February 22nd, 2021

Reconstructing the morphologies and hydrodynamics of ancient rivers from source to sink: Cretaceous Western Interior Basin, Utah, USA

Sinéad J. Lyster[1]*, Alexander C. Whittaker[1], Gary J. Hampson[1], Elizabeth, A. Hajek[2], Peter A. Allison[1] and Bailey A. Lathrop[1]

[1] Department of Earth Science and Engineering, Imperial College London, London, UK.

[2] Department of Geosciences, The Pennsylvania State University, Pennsylvania, USA.

*s.lyster17@imperial.ac.uk

(A) Abstract

Quantitative reconstruction of palaeohydrology from fluvial stratigraphy provides sophisticated insights into the response, and relative impact, of tectonic and climatic drivers on ancient fluvial landscapes. Here, field measurements and a suite of quantitative approaches are used to develop a four-dimensional (space and time) reconstruction of palaeohydrology in Late Cretaceous palaeorivers of central Utah, USA — these rivers drained the Sevier mountains to the Western Interior Seaway. Field data include grain-size and cross-set measurements and span five parallel fluvial systems, two of which include up-dip to down-dip transects, across seven stratigraphic intervals through the Blackhawk Formation, Castlegate Sandstone and Price River Formation. Reconstructed palaeohydrological parameters include fluvial morphologies (flow depths, palaeoslopes, palaeorelief, and planform morphologies) and various hydrodynamic properties (flow velocities, water discharges, and sediment transport modes). Results suggest that fluvial morphologies were similar in space and time; median flow depths spanned 2–4 m with marginally greater flow depths in southerly systems. Meanwhile palaeoslopes spanned 10^{-3} to 10^{-4}, decreasing downstream by an order of magnitude. The most prominent spatio-temporal change is an up to four-fold increase in palaeoslope at the Blackhawk–Castlegate transition; associated alluvial palaeorelief is tens of metres during Blackhawk deposition and >100 m during Castlegate Sandstone deposition. We observed no change in unit water discharges at the Blackhawk–Castlegate transition, which argues against a climatically driven increase in palaeoslope and channel steepness. These findings instead point to a tectonically driven palaeoslope increase, although one limitation in this study is uncertainty in palaeochannel widths, which directly influences total water discharges. These reconstructions complement and expand on extensive previous work in this region, which enables us to test the efficacy of quantitative reconstruction tools. Comparison of results with facies-based interpretations indicates that quantitative tools work well, but inconsistencies in more complex reconstructions (e.g. planform morphologies) highlight the need for further work.

(A) Introduction

The stratigraphic record is a fundamental archive of Earth surface processes in space and time (Wobus et al., 2006; Allen, 2008a, 2008b; Armitage et al., 2011; Whittaker, 2012). A key research challenge is to decode this archive to reconstruct the movement of water and sediment across Earth's surface in the geological past (Castelltort & Van Den Driessche, 2003; Jerolmack & Paola, 2010; Ganti et al., 2014; Romans et al., 2016; Straub et al., 2020) — effective quantification of palaeohydrology from fluvial

stratigraphy is crucial to achieve this goal. Constraints on the morphologies and hydrodynamics of palaeorivers can be used to: resolve the size and scale of ancient catchments (Bhattacharya & Tye, 2004; Bhattacharya et al., 2016; Eide et al., 2018; Lyster et al., 2020); quantify sediment transport capacities and the magnitudes of sediment exported to oceans (Allen et al., 2013; Holbrook & Wanas, 2014; Lin & Bhattacharya, 2017; Sharma et al., 2017); decipher fluvial response to perturbation (Foreman et al., 2012; Foreman, 2014; Colombera et al., 2017; Chen et al., 2018); and reconstruct local palaeogeographies (Li et al., 2018). Importantly, these constraints can be used to investigate hydrological response to long-period forcing (>10^6 yrs) as river behaviour is intrinsically linked to tectono-climatic boundary conditions over geological timescales (Duller et al., 2010; Whitchurch et al., 2011; Whittaker et al., 2011; Castelltort et al., 2012; Hampson et al., 2013).

However, palaeohydrology is limited by incomplete (or absent) records of palaeorivers (Sadler, 1981; Jerolmack & Sadler, 2007), uncertainty as to what information fluvial stratigraphy actually preserves (Castelltort & Van Den Driessche, 2003; Jerolmack & Paola, 2010; Romans et al., 2016; Straub et al., 2020), and uncertainties associated with data type, data measurement, and reconstruction tools (e.g. Bridge & Tye, 2000). Where it is possible to overcome these challenges, the ability to decipher palaeohydrological information with high fidelity can enable sophisticated insights to be drawn about the sensitivity and response of ancient fluvial systems to tectonic and climatic drivers.

Here, a quantitative framework is used to reconstruct the palaeohydrological evolution of well-known source-to-sink systems of Late Cretaceous central Utah, USA. The focus of this study is the Blackhawk Formation–Castlegate Sandstone–Price River Formation fluvial succession as outcrops are extensive and well-documented (Kauffman, 1977; Kauffman & Caldwell, 1993; Cobban et al., 2006). These strata represent eastward flowing palaeorivers that drained the Sevier orogenic fold-and-thrust belt to the Western Interior Seaway (WIS). Previous work has primarily focused on *qualitative* inferences of palaeohydrology in these systems (Miall, 1994; Miall & Arush, 2001; Adams & Bhattacharya, 2005; McLaurin & Steel, 2007; Hampson et al., 2012; Flood & Hampson, 2014), which are sometimes complimented by simple quantitative reconstructions (e.g. Hampson et al., 2013). Meanwhile, *quantitative* work has mostly focused on architectural-scale elements in these systems, including preservation of channelized bodies and bars and associated autogenic processes, such as avulsion and backwater dynamics (Hajek et al., 2010; Hajek & Wolinsky, 2012; Flood & Hampson, 2015; Trower et al., 2018; Chamberlin & Hajek, 2019; Ganti et al., 2019a). The palaeohydrological evolution of these rivers at the system scale has not been comprehensively addressed using quantitative tools — this study addresses this outstanding research challenge to shed new light on these ancient systems.

Palaeohydrological field data were collected for 5 parallel transverse fluvial systems (spaced ~20–25 km apart) across 7 stratigraphic intervals within the Campanian stage (83.6±0.2 to 72.1±0.2 Ma) of the Late Cretaceous, which spanned 11.5 Myr (Figs 1, 2). These data allow for high resolution spatio-temporal reconstructions of these systems, both up-dip to down-dip and along depositional strike (Fig. 1). Reconstructed palaeohydrologic parameters include: flow depths; palaeoslopes and palaeorelief (specific to the alluvial domain); hydrodynamic properties, including flow velocities, water discharges and sediment transport modes; and planform morphologies. First and foremost, results show how the morphologies and hydrodynamic properties of these palaeorivers varied in space and time. Moreover, reconstruction of palaeoslopes and palaeorelief in the alluvial domain enable evaluation of the competing roles of tectonic and climatic drivers on the evolution of these ancient rivers. Finally, the

results provide new insights regarding the extent to which quantitative palaeohydrologic methods (which are increasingly borrowed from the field of engineering) can be reconciled with sedimentological observables.

(A) Research background

(B) Palaeohydrology

Palaeohydrological interpretations traditionally derive from analysis of facies associations in fluvial strata, particularly of architectural-scale elements (Miall, 1994; Miall & Arush, 2001; Adams & Bhattacharya, 2005; McLaurin & Steel, 2007; Hampson et al., 2012; Hampson et al., 2013; Flood & Hampson, 2014), and increasingly take advantage of high-resolution remote imagery and three-dimensional outcrop models (Hajek & Heller, 2012; Rittersbacher et al., 2014; Chamberlin & Hajek, 2019). However, a combination of empirical, theoretical and experimental work has led to the development of fluid and sediment transport models that are applicable to geologic questions (e.g. van Rijn, 1984b; Ferguson & Church, 2004; Parker, 2004; Wright & Parker, 2004; Mahon & McElroy, 2018), enabling more sophisticated inferences of palaeohydrology from the rock record.

Recent quantitative research has focused on maximising the ability to accurately reconstruct the evolution of fluvial landscapes in the geologic past. Some efforts have centred on connecting landscape surface kinematics to stratal preservation (Paola & Borgman, 1991; Castelltort & Van Den Driessche, 2003; Jerolmack & Mohrig, 2005; Jerolmack & Paola, 2010; Hajek & Wolinsky, 2012; Ganti et al., 2013; Ganti et al., 2014; Reesink et al., 2015; Romans et al., 2016; Ganti et al., 2020; Leary & Ganti, 2020; Straub et al., 2020) and a number of these studies have focused on Late Cretaceous fluvial strata in central Utah (Flood & Hampson, 2015; Trower et al., 2018; Chamberlin & Hajek, 2019; Ganti et al., 2019a). Meanwhile, other quantitative work has applied fluid and sediment transport models to stratigraphic field data, with an overarching goal of constraining the characteristics of catchments, regional systems or entire fluvial landscapes in the geological past (Ganti et al., 2019b; Lapôtre et al., 2019), or even on other planetary bodies (Lamb et al., 2012; Buhler et al., 2014; Hayden et al., 2019; Lapôtre et al., 2019). This includes using quantitative palaeohydrological tools to reconstruct water and sediment discharges within mass balance frameworks (Holbrook & Wanas, 2014; Lin & Bhattacharya, 2017; Sharma et al., 2017), decipher local palaeogeographies (Bhattacharyya et al., 2015; Li et al., 2018), characterise pre-vegetation rivers (Ganti et al., 2019b), and reconstruct fluvial response to climatic perturbations for well-preserved fluvial strata straddling events such as the Paleocene–Eocene Thermal Maximum (PETM) (Foreman et al., 2012; Foreman, 2014; Colombera et al., 2017; Chen et al., 2018; Duller et al., 2019).

Despite the breadth of quantitative palaeohydrological tools available, previous applications to fluvial stratigraphic field data have typically centred on individual catchments and instantaneous or short-period intervals (i.e. individual discharge events and mean annual discharges) (Holbrook & Wanas, 2014; Lin & Bhattacharya, 2017; Sharma et al., 2017), or reconstructions across stratigraphic boundaries and short-period tectono-climatic events, such as the PETM (Foreman et al., 2012; Foreman, 2014; Colombera et al., 2017; Chen et al., 2018; Duller et al., 2019). Far fewer studies have focused on long-period intervals, such as the evolution of source-to-sink systems across geologic timescales (>10^6 yrs). This outstanding opportunity can be exploited in Late Cretaceous fluvial systems

of central Utah, where outcrop availability supports a four-dimensional (space and time) study in a region subject to active tectonics, spanning both Sevier and Laramide deformation.

(B) Tectono-geographic setting and palaeodrainage

Input of sediment to the Late Cretaceous WIS was dominated by the western margin, where rivers draining the active Sevier fold-and-thrust belt eroded and transported huge volumes of clastic sediments eastwards into the foreland basin (Spieker, 1946; Armstrong, 1968; Kauffman, 1977; Hay et al., 1993; Kauffman & Caldwell, 1993) (Fig. 1b,c). This led to the deposition and progradation of a large, asymmetric clastic wedge on the western WIS margin. This study focuses on Campanian non-marine clastic sediments of this wedge in central Utah, USA (Figs 1–3), where palaeodrainage is relatively well-constrained (Bartschi et al., 2018; Pettit et al., 2019). Multiple transverse fluvial systems drained the Sevier thrust belt in this area (Fig. 1b). Several studies have additionally interpreted an axial, or longitudinal, fluvial system that drained north–northeast from the Mogollon Highlands (present day central Arizona) and Cordilleran magmatic arc, which interacted with transverse systems of the Sevier thrust belt (Lawton et al., 2003; Jinnah et al., 2009; Szwarc et al., 2015) (Fig. 1b) and led to downsystem sediment mixing (Bartschi et al., 2018; Pettit et al., 2019). Detrital zircon data (Bartschi et al., 2018) indicate that these fluvial systems were dominated by a thrust-belt source in close proximity to the Sevier thrust front, but that more southerly transverse systems may have additionally featured a longitudinal component of drainage (Bartschi et al., 2018; Pettit et al., 2019). Herein, focus is on transverse fluvial systems that predominantly drained the Sevier mountains (Fig. 1).

Tectonic forcing in this region is well studied (DeCelles, 1994, 2004; DeCelles & Coogan, 2006) and palaeoclimate has been reconstructed from a variety of palaeontological, geochemical-proxy and modelling studies (e.g. Wolfe & Upchurch Jr., 1987; Fricke et al., 2010; Miller et al., 2013; Sewall & Fricke, 2013; Foreman et al., 2015). In central Utah, eastward propagation of the Sevier thrust belt (due to eastward subduction of the Farallon plate) resulted in thin-skinned deformation and movement on the north–south trending Canyon (~145−110 Ma), Pahvant (~110−86 Ma), Paxton (86−75 Ma) and Gunnison (75−65 Ma) thrust systems (DeCelles, 1994, 2004; DeCelles & Coogan, 2006). Associated exhumation created substantial topographic relief in the Sevier mountains, which has been described as “Andean” in scale with mean elevations approaching near 4000 m (Sewall & Fricke, 2013; Foreman et al., 2015). Modelling results and stable isotope evidence suggest a strong monsoonal precipitation along the eastern flank of the Sevier mountains and seasonal flooding across low-relief regions (Roberts, 2007; Roberts et al., 2008; Fricke et al., 2010; Sewall & Fricke, 2013). The tectono-geographic set-up of the Western Interior was particularly conducive to a monsoonal climate — the proximity of a warm sea to high elevation mountains commonly results in strong seasonal precipitation and convective circulation (e.g. Zhisheng et al., 2001). A seasonal temperate-to-subtropical climate therefore prevailed throughout Campanian deposition (L. R. Parker, 1976; Kauffman & Caldwell, 1993; Roberts & Kirschbaum, 1995). The Campanian onset of thick-skinned deformation as the subducting Farallon plate transitioned to lower-angle, or flat-slab, subduction (DeCelles, 2004) began to manifest as basement-cored Laramide uplifts (e.g. San Rafael Swell, central Utah, and Uinta Mountains, northern Utah), which partitioned the Sevier foreland basin and disrupted patterns of both regional subsidence and drainage (Bartschi et al., 2018; Pettit et al., 2019).

(B) Stratigraphic framework

Establishing a consistent stratigraphic framework in space and time is crucial for system scale palaeohydrological reconstructions. Here, focus is on the Upper Cretaceous Mesaverde Group and up-dip equivalents (Figs 1, 2) in central Utah, USA, specifically fluvial sediments situated less than ~100 km from the Sevier orogenic front (DeCelles & Coogan, 2006) in the flexurally subsiding foredeep (Fig. 3). These sediments include the Blackhawk Formation, Castlegate Sandstone and Price River Formation along the eastern front of the Wasatch Plateau (Figs 1–3). Up-dip, on the western Wasatch Plateau, the Blackhawk–Castlegate–Price River succession is correlated with the Sixmile Canyon Formation (Indianola Group) and the Price River Conglomerate (following Robinson and Slingerland (1998); Horton et al. (2004); Aschoff and Steel (2011b, 2011a)) (Figs 1–3). Up-dip to down-dip, these sediments encompass the entire alluvial domain of these palaeorivers draining the Sevier highlands. A broad summary of field sites and the stratigraphic framework (Figs 1, 2) is given below — extended information regarding regional stratigraphy and correlations is provided in the Supplementary Material.

Down-dip field sites were grouped spatially into 5 field areas that represent 5 parallel transverse fluvial systems draining the Sevier thrust front: Price Canyon, Wattis Road, Straight Canyon (including Joe's Valley Reservoir), Link Canyon and Salina Canyon (Figs 1, 3). These 5 field areas are approximately ~50 km from up-dip alluvial fan lobes (Figs 1, 3). Assuming typical outlet spacings of rivers draining orogenic fronts (~25 km) (Hovius, 1996), it is likely that these field areas represent 5 distinct palaeorivers and form a ~125 km transect along depositional strike. For the 2 up-dip to down-dip transects (Fig. 1), the northern transect included 4 field areas: Dry Hollow, Lake Fork, Bear Canyon, and terminating at Price Canyon (Fig. 3c–e), and the southern transect included 3 field areas: Mellor Canyon, Sixmile Canyon, and terminating at Straight Canyon (Fig. 3d–f). These transects follow those widely implemented in previous work, both along-strike (Hampson et al., 2012; Hampson et al., 2013; Flood & Hampson, 2014, 2015; Chamberlin & Hajek, 2019) and up-dip to down-dip (Robinson & Slingerland, 1998; Horton et al., 2004; Aschoff & Steel, 2011b, 2011a).

In addition to grouping field sites in space, they were also grouped in time. In this study 7 stratigraphic intervals were defined: 1 = lower Blackhawk Formation; 2 = middle Blackhawk Formation; 3 = upper Blackhawk Formation; 4 = lower Castlegate Sandstone; 5 = middle Castlegate Sandstone; 6 = upper Castlegate Sandstone (Bluecastle Tongue); 7 = (lowermost) Price River Formation (Fig. 2).

Down-dip, on the eastern front of the Wasatch Plateau, it is straightforward to assign sediments of the Blackhawk–Castlegate–Price River succession to the appropriate "space–time" interval by facies associations, following extensive work that has been undertaken in this region (Lawton, 1983, 1986b; Miall, 1994; van Wagoner, 1995; Yoshida et al., 1996; Miall & Arush, 2001; Lawton et al., 2003; Adams & Bhattacharya, 2005; Hampson et al., 2012; Hampson et al., 2013; Flood & Hampson, 2014; Hampson et al., 2014; Flood & Hampson, 2015). The lower–middle Campanian Blackhawk Formation represents deposition on coastal plains behind wave-dominated deltaic shorelines which, up-section, pass landward into alluvial and fluvial plains (Hampson, 2010; Hampson et al., 2012; Hampson et al., 2013). The size and abundance of channelized fluvial sand bodies (deposited by both single- and multi-thread rivers) increase from base to top of the Blackhawk Formation (Adams & Bhattacharya, 2005; Hampson et al., 2012; Hampson et al., 2013; Flood & Hampson, 2015). The middle–upper Campanian Castlegate Sandstone is situated atop the Blackhawk Formation and is an extensive, cliff-forming river-dominated deposit. The lower Castlegate Sandstone and upper Castlegate Sandstone (Bluecastle Tongue) comprise amalgamated braided fluvial channel-belt deposits, whereas the middle Castlegate

Sandstone comprises less amalgamated, more meandering, fluvial channel-belt deposits with interbedded mudstones (Fouch et al., 1983; Lawton, 1986b; Miall, 1994; van Wagoner, 1995; Yoshida et al., 1996; Miall & Arush, 2001). The ledge-forming upper Campanian Price River Formation sits conformably atop the Castlegate Sandstone and comprises large channelized sand bodies with interbedded siltstones and mudstones — channelized sand bodies form ~75% of the formation (Lawton, 1983, 1986b). Fluvial sediments of the Price River Formation represent the end of Sevier thrusting; the late Maastrichtian–Eocene North Horn Formation unconformably overlies the Price River Formation.

Up-dip, on the western Wasatch Plateau, correlative strata include more proximal sediments of the Indianola Group and Price River Formation, which is now known to not be time-equivalent with the down-dip Price River Formation exposed near Price, Utah (Robinson & Slingerland, 1998; Horton et al., 2004; Aschoff & Steel, 2011b, 2011a). To avoid confusion, these up-dip strata are here referred to as the Price River Conglomerate, following Aschoff and Steel (2011b, 2011a). Up-dip to down-dip correlations are limited by incomplete exposure on the western Wasatch Plateau and difficulty in dating conglomerates (see Supplement). Nevertheless, Robinson and Slingerland (1998) used palynology to correlate these strata across a variety of localities on the Wasatch Plateau (Fig. 2), which can be traced in seismic reflection data (Horton et al., 2004). The up-dip Price River Conglomerate is time-correlative with the down-dip lower, middle, and upper Castlegate Sandstone, and Price River Formation (Robinson & Slingerland, 1998; Horton et al., 2004; Aschoff & Steel, 2011b, 2011a), and is characterised by quartzite-dominated synorogenic fanglomerates and few gravel–sand fluvial bodies (Robinson & Slingerland, 1998; Aschoff & Steel, 2011b, 2011a). Of the Indianola Group, the upper Sixmile Canyon Formation is time-correlative with the Blackhawk Formation (Lawton, 1982; Fouch et al., 1983; Lawton, 1986b) and is predominantly characterised by synorogenic gravel–sand fluvial facies, spanning polymictic fluvial conglomerates to medium–coarse-grained sandstones (Lawton, 1982, 1986a, 1986b). Here a conservative approach is taken to up-dip to down-dip correlations; the upper Sixmile Canyon Formation of the Indianola Group (intervals 1–3) is time-averaged, and the Price River Conglomerate (intervals 4–7) is also time-averaged, but exceptions were made where field sites were known to be situated at either the top of the upper Sixmile Canyon Formation or at the top/base of the Price River Conglomerate. A full description of these correlations, including new logging in Mellor Canyon, is presented in the Supplement.

Each depositional-dip transect is pinned at the most downstream location, i.e. it is assumed that the most down-dip sites in each transect (Price Canyon and Straight Canyon) are approximately parallel and at the same downstream distance. Transects then work upstream, such that the most up-dip field site (Dry Hollow; northern transect) is at a downstream distance of 0 km. Downstream distances follow Robinson and Slingerland (1998) —post-depositional extension is not corrected for. Alternatively, when reconstructing along-depositional-strike transects, transects are pinned at the most northern location (Price Canyon) with an along-strike distance of 0 km, meanwhile southern locations have along-depositional-strike distances up to 125 km.

(A) Methods

Data were collected from channel-fill stratigraphy (cross-stratified sandstone and gravel deposits are interpreted as channel floor deposits) and were time-averaged across each stratigraphic space–time interval (field sites are listed in Supplementary Table S2). These field data, including uncertainties,

were propagated through a quantitative framework to reconstruct the morphologies and hydrodynamics (flow depths, palaeoslopes, river long profiles, flow velocities and discharges, sediment transport modes and likely planform morphologies) of palaeorivers in both space and time.

(B) Field observations

(C) Grain size

At each field site the coarse-fraction (>2 mm in diameter) and sand-fraction (<2 mm in diameter) grain-sizes of channel-fill deposits were established (Fig. 4a,b). For coarse-fractions, grain-size distributions were measured via Wolman point counts (Wolman, 1954) (Fig. 4a); this technique has been successfully used to decode spatio-temporal trends in grain-size (e.g. Whittaker et al., 2011; D'Arcy et al., 2017; Brooke et al., 2018). For sand-fractions, scaled photographs were processed in *ImageJ* software and, similarly, the long axis of a minimum of 50 randomly selected grains was measured to recover grain-size distributions (Fig. 4b). From each measured grain-size distribution, the median grain-size, D_{50}, and 84th percentile, D_{84}, were extracted. Where grain-size facies were disparate, e.g. gravel topped with sand, data were collected for each grain-size facies and the proportions of each were estimated (Fig. 4c).

In order to achieve representative sampling for spatio-temporal grain-size trends, multiple grain-size observations were collected at each field site. Not only were data collected for each grain-size facies (Fig. 4a–c), but depending on overall outcrop extent Wolman point counts were repeated and/or additional scaled photographs were taken for *ImageJ* processing at intermittent stratigraphic intervals (e.g. one count per 5–10 m of strata or per channelized body). The extent of each field site can be approximated as the extent of outcrop apparent in Fig. 3c–h. From these data an average grain-size was produced for both the sand-fraction and gravel-fraction at each field site. As each space–time interval includes multiple field sites, this results in multiple average sand- and gravel-fraction grain-sizes, capturing channel-fill deposits from several channelized bodies. Finally, a bulk-grain-size was produced for each space–time interval using the gravel-to-sand proportions at each field site — each site within a space–time interval was assigned equal weighting. Further information regarding grain-size data collection, including axis selection, sample size sufficiency and weighting, is presented in the Supplement.

(C) Cross-sets

Cross-set heights were measured as these data can be used to reconstruct original bedform heights and formative flow depths. Trough- and planar-cross bedding, which are inherently indicative of bedload transport, were present at nearly all field sites. They occurred predominantly in sand-grade deposits, but also in granule- to pebble-grade deposits (Fig. 4d–f). To establish mean cross-set heights, the sampling strategy of Ganti et al. (2019b) was followed. Cross-set boundaries (i.e. the lower, asymptotic bounding surface and the upper, erosional bounding surface) were delineated and then heights were measured at regular intervals along the entire width of the cross-set dip-section (Fig. 4g–i). Measurements were made to a precision of ±5 mm. This protocol was repeated for individual cross-sets within co-sets to establish a mean cross-set height for each individual cross-set. Subsequently, maximum cross-set heights (i.e. the maximum distance between lower and upper bounding surfaces) were measured for a representative sample across the exposed outcrop (usually n=25–50).

From cross-sets for which height distributions were measured (n=470), the mean, 84th percentile (P_{84}), and maximum heights of each individual cross-set were extracted. From these data, the relationship between maximum and mean cross-set heights was established. This new relationship was then used to estimate mean cross-set heights from all measured maximum cross-set heights (n=4053). This maximised the amount of field data that could be collected, and therefore analysed, at each field site — it is more efficient to measure maximum cross-set heights than height distributions of individual cross-sets. These estimates of mean cross-set heights were propagated through subsequent calculations, as measurements of mean cross-set heights are more appropriate than maximum cross-set heights in reconstruction of palaeohydrologic parameters (e.g. Equation 1).

(C) Channel geometry and architectural element data

Above grain- and bedform-scales, channel geometries and major architectural elements were also measured, where possible, using a Haglof Laser Geo laser range finder to a precision of ±5 cm. This included maximum channel body/story thicknesses and bar-scale clinoform heights. Previous work in this region has documented the dimensions and distributions of fluvial architectural elements using high-resolution imagery and 3D outcrop models (Hajek & Heller, 2012; Rittersbacher et al., 2014; Flood & Hampson, 2015; Chamberlin & Hajek, 2019). Field data collection therefore focused on grain-size and cross-set measurements, with compilation of published secondary data (alongside new data from this study) to augment field data and evaluate our palaeohydrological reconstructions (see Supplementary Tables S4, S5).

(B) Quantitative palaeohydrology

(C) Channel geometries

To calculate original bedform heights from cross-set measurements, the relation of Leclair and Bridge (2001) was used, which is based on theoretical work by Paola and Borgman (1991). Leclair and Bridge (2001) showed that mean bedform (i.e. dune) height, h_d, can be approximated as a function of mean cross-set height, h_{xs}, as

$$h_d = 2.9(\pm 0.7)h_{xs}, \quad \text{Eq. 1}$$

where 2.9 is the mean and 0.7 is the standard deviation. Given that exact error margins of palaeohydrologic inversion methods cannot be known, a Monte Carlo uncertainty propagation method is used in this study to estimate uncertainty and offer plausible spreads of values for each reconstructed palaeohydrological parameter. In Equation 1, uncertainty is represented as the mean (μ) and one standard deviation (σ). As such, 10^6 random samples were generated between bounds defined by μ−σ and μ+σ. Samples were generated from a uniform distribution as the shape and the scale of the full distribution of the data is not known — this approach avoids introduction of additional assumptions. These values are then propagated through subsequent calculations.

While bedform height generally scales with flow depth, the mechanistic explanation for this is not fully resolved. As such, many scaling relations simply relate bedform height and flow depth (e.g. Yalin, 1964), whereas some incorporate additional parameters such as Froude number, D_{50}, and transport

stage (e.g. Gill, 1971; van Rijn, 1984a), however their incorporation does not improve predictive power. Bradley and Venditti (2017) revisited previous bedform height−flow-depth scaling relations and derived a new relation between h_d and median formative flow depth, H, based on >380 field observations, where

$$H = 6.7h_d. \quad \text{Eq. 2}$$

In detail, Bradley and Venditti (2017) derived two relations to reconstruct H from h_d. Their first relation was derived from regression analysis and recovered μ and σ, however the authors argued that this relation is not useful as the data are not normally- or log-normally distributed, and that the tails of the distribution are not fully represented (Bradley & Venditti, 2017). The authors additionally presented a non-parametric relation to derive median H (Equation 2) with a probabilistic uncertainty estimator in which the 1st and 3rd quartiles of H are given by H=4.4h_d and H=10.1h_d, respectively (Bradley & Venditti, 2017). Bradley and Venditti (2017) noted that this probabilistic uncertainty estimator better represented their data, as it does not assume an underlying distribution. This relation is more appropriate in palaeohydrologic reconstructions as, with a larger uncertainty estimate, it offers a broader spread of possible H values. As such, 10^6 uniformly distributed random samples were generated between 4.4 and 10.1, and these model parameter values were used to generate likely palaeoflow depths in these ancient systems. Where cross-bedding was absent (i.e. the most up-dip field sites), channel-body thicknesses were used as a proxy for flow depth.

Similar to H, channel width, W, can be estimated using scaling relations as direct measurement is not normally possible from outcrop. Bridge and Mackey (1993) proposed the relation W=8.8$H^{1.82}$ for single-thread channels. Alternatively, widths of fully-braided channel systems can be approximated as, for example, W=42$H^{1.11}$ (Leopold & Maddock Jr, 1953). However, estimates of W from outcrop data and scaling relations are particularly tentative and, where systems are braided, subject to further uncertainty pertaining to the number of threads. As such, results in this study are reported per unit width.

(C) Palaeoslopes and palaeorelief

Palaeoslopes were estimated using 2 independent methodologies, adapted from Ganti et al. (2019a). First, Shields stress, τ^*, was estimated using the bedform stability diagram of Carling (1999), which expresses bedform stability in terms of τ^* and D_{50} (for D_{50} < 33 mm). Minimum and maximum bounds of τ^* for the stable existence of dunes were then identified for a range of D_{50} values. Then, 10^6 uniformly distributed random samples of τ^* were generated between these grain-size-dependent bounds. Where D_{50} exceeded 33 mm, and in the absence of bedforms, possible τ^* values of 0.03–0.06 were assigned. To reconstruct palaeoslope, S, the bed shear stress, τ_b, was approximated as the depth–slope product (τ_b=ρgHS) and then S can be given as

$$S = \frac{RD_{50}\tau^*}{H}, \quad \text{Eq. 3}$$

where R is the dimensionless submerged specific gravity of sediment in water (1.65 for quartz) and H is the flow depth (ρ is density and g is acceleration due to gravity). For the second approach, the method of Trampush et al. (2014) was used, which is based on Bayesian regression analysis of bankfull measurements in modern alluvial rivers (n=541); here slope is expressed as

$$\log S = \alpha_0 + \alpha_1 \log D_{50} + a_2 \log H \,, \quad \text{Eq. 4}$$

where the constants are given by $\alpha_0 = -2.08 \pm 0.036$, $\alpha_1 = 0.254 \pm 0.016$, and $\alpha_3 = -1.09 \pm 0.044$. Again, 10^6 values of α_0, α_1, and α_3 were generated (uniformly distributed random samples between $\mu-\sigma$ and $\mu+\sigma$). Having propagated 10^6 values of τ^*, H, α_0, α_1, and α_3 into these calculations, 10^6 values of S were recovered for both Equations 3 and 4, which can then be contrasted.

Along up-dip to down-dip transects, palaeoslope estimates can be used to infer the shape of the river long profile, and therefore palaeorelief, in the alluvial domain. Palaeorelief was reconstructed using estimates of S from Equations 3 and 4. For simplicity, median S was extracted from these values and used to derive palaeorelief. The local slope at downstream position x, S_x, can be related to its upstream contributing catchment area, A_x, (Hack, 1973; Flint, 1974; Whipple, 2004) as

$$S_x = k_s {A_x}^{-\theta} \,, \quad \text{Eq. 5}$$

where k_s is the steepness index and θ is the concavity, typically between 0.4 and 0.7 (Tucker & Whipple, 2002). Given that the palaeo-concavity is unknown, a range of plausible concavities (0.4, 0.5, and 0.6) were tested to gauge the spread of possible results. Following Hack's law, local catchment length, L_x, is related to A_x by $L_x = c_H {A_x}^h$, where c_H is the Hack coefficient, commonly taken as near 2 when L_x and A_x are in units of km^2 (Castelltort et al., 2009), and h is the Hack exponent, commonly taken as 0.5 (Hack, 1957). Using Hack's law, local slope can instead be estimated as a function of downstream distance, where

$$S_x = k_s {L_x}^{-\theta/h} \,. \quad \text{Eq. 6}$$

k_s is calculated from field data using downsystem palaeoslope estimates and knowledge of catchment lengths at each downstream location. As this study solely focuses on the alluvial domain, this means that up-dip fan apexes would have a catchment length of 0 km. Here, the most up-dip field sites are set as having a catchment length of 5 km to allow for additional up-dip fan length. Knowledge of distance to the coeval palaeoshoreline from our most down-dip sites (Price Canyon and Straight Canyon) is also required. Based on previous studies, approximate distances to the palaeoshoreline are set as ~10 km for the lower Blackhawk Formation, ~35 km for the middle Blackhawk Formation, ~50 km for the upper Blackhawk Formation, ~110 km for the Castlegate Sandstone (Hampson et al., 2012; Hampson et al., 2013), and ~200 km for the Price River Formation (Hettinger & Kirschbaum, 2002; Aschoff & Steel, 2011a). A nonlinear least squares regression was used to find best fit palaeoslope profiles (Equation 6) for both the northern and southern transects at each time interval. Palaeoslope profiles were then transformed into river long profiles by summing elevation increments along the

downstream length to the palaeoshoreline. This elevation decrease is indicative of the likely relief in the alluvial domain of these palaeorivers.

(C) Hydrodynamics

In subsequent calculations, values derived from Monte Carlo uncertainty propagation were used, i.e. 10^6 estimates of *H*, *S,* etc. Specifically, estimates of *S* derived from the Shields stress inversion (Equation 3) were carried forward. Flow velocities, *U*, were calculated following Manning's Equation, where

$$U = \frac{1}{n} H^{\frac{2}{3}} S^{\frac{1}{2}} \quad , \qquad \text{Eq. 7}$$

and *n* is Manning's constant, set as 0.03. Water discharges were then estimated by multiplying flow velocity by flow depth, to obtain discharge per unit width (*Q*=*UH*).

To determine dominant mode of sediment transport, the Rouse number, *Z*, was calculated as

$$Z = \frac{w_s}{\beta \kappa u_*} \qquad \text{Eq.8}$$

where β is a constant that correlates eddy viscosity to eddy diffusivity, typically taken as 1, κ is the von Karman constant, taken as 0.4, and u^* is the bed shear velocity ($gHS^{0.5}$). Sediment settling velocity, w_s, was calculated as a function of grain size following Ferguson and Church (2004),

$$w_s = \frac{RgD_{50}{}^2}{C_1 v + (0.75 C_2 RgD_{50}{}^3)^{0.5}}, \qquad \text{Eq. 9}$$

where *v* is the kinematic viscosity of water (1×10^{-6} m^2/s for water at 20°C) and C_1=18 and C_2=1 are constants associated with grain sphericity and roundness. With *Z*, dominant mode of sediment transport is typically wash load for $Z < 0.8$, 100% suspended load for $0.8 < Z < 1.2$, 50% suspended load (i.e. mixed load) for $1.2 < Z < 2.5$, and bedload for $Z > 2.5$. To corroborate inferred sediment transport modes, the particle Reynolds number, Re_p, was additionally calculated in line with previous work (cf. Parker, 2004) as

$$Re_p = \frac{\sqrt{RgD_{50}} D_{50}}{v} \qquad \text{Eq. 10}$$

and plotted as a function of τ^*, following Dade and Friend (1998). This enables field results to be contrasted with data that are typical of either suspended, mixed, or bedload sediments (Leopold & Wolman, 1957; Schumm, 1968; Chitale, 1970; Church & Rood, 1983; Andrews, 1984), and to identify where these data are positioned among characteristic flow regimes (no sediment transport; ripples and dunes; upper plane beds) following Allen (1982a, 1982b).

(C) Fluvial style

Fluvial style (i.e. planform morphology) of Blackhawk–Castlegate rivers has been described qualitatively from outcrop architecture (Miall, 1994; Miall & Arush, 2001; Adams & Bhattacharya, 2005; Hampson et al., 2013). Here, a quantitative approach is implemented to decipher fluvial style to complement these works, check for consistency, and interpret the interplay between different planform morphologies and the tectono-geographic setting. This is carried out for field areas along the eastern Wasatch Plateau. First, Froude number, *Fr*, is calculated as

$$Fr = \frac{U}{\sqrt{gH}} \quad \text{Eq. 11}$$

and, then, depth/width ratios were plotted against palaeoslope/Froude ratios (G. Parker, 1976). Various flow widths were assigned to determine what depth/width ratios are required such that the data fall within the theoretical stability fields for single-thread and multi-thread fluvial planform morphologies. These flow widths are then contrasted with estimates of apparent maximum flow width from architectural analysis of channelized sandstone bodies (e.g. Flood & Hampson, 2015) and field interpretations of fluvial style (Miall, 1994; Miall & Arush, 2001; Adams & Bhattacharya, 2005; Hampson et al., 2013).

For all palaeohydrological parameters the median (2nd quartile) result is presented. Where minima and maxima are presented, these bounds reflect the full spread of recovered values. These are offered as plausible minimum and maximum values for the median, derived from propagation of uncertainty margins. In instances where a 1st–3rd interquartile range is additionally presented, specifically in box-and-whisker plots, this is the 1st–3rd interquartile range that has been extracted for each parameter from the 10^6 values recovered by Monte Carlo error propagation. The whiskers in these plots effectively describe the minimum and maximum values of the data, and can also be considered as plausible minimum and maximum values for the median.

(A) Results

(B) Channel geometries

Linear relationships between maximum cross-set height and both the mean and the P_{84} cross-set height were established from measured cross-set distributions (n=470) for our field area (Fig. 5a,b). Maximum and mean cross-set heights are well-correlated (R^2=0.88) and 95% of observed mean cross-set heights fall within ~3 cm of the predicted mean cross-set height. Using these new relationships, mean cross-set heights were estimated for all (n=4053) measured maximum cross-set heights (Fig. 5c–e; Supplementary Table S3).

Maximum cross-set heights typically span 0.1–0.35 m — these field data are comparable to the results of previous work (e.g. Adams & Bhattacharya, 2005). From maximum cross-set heights, mean cross-set heights spanning 0.07–0.25 m are estimated, which correspond with original bedform heights of 0.2–0.75 m. Flow depths for the along-depositional-strike transect suggest that, in both space and time, these 5 transverse fluvial systems maintained median flow depths of 2–4 m, with a range of 1–7 m (Fig. 6). Overall, flow depths do not change across the Blackhawk–Castlegate transition but exhibit

a marginal decrease during middle Castlegate Sandstone deposition of <0.5 m. Flow depths are also projected to be overall <1 m greater in southern fluvial systems (Fig. 6). However, these observed differences all lie within the uncertainty margins of calculations, suggesting these systems were similar to each other.

Reconstructed palaeoflow depths are consistent with independent palaeoflow depth proxies (Supplementary Table S4), which demonstrates applicability of cross-set scaling relations in the absence of well-preserved macroforms. Bar heights, where available, are consistent with projected flow depths of 2–4 m across field sites. For instance, Chamberlin and Hajek (2019) reported mean bar heights of 2.6 m, 3.6 m and 3.9 m for the entire Castlegate Sandstone at Price Canyon, Straight Canyon and Salina Canyon, respectively. At Price Canyon, both Lynds and Hajek (2006) and Hajek and Heller (2012) reported greater mean bar heights of 4.1 m specifically for the lower Castlegate Sandstone, with a typical span of 1–8 m (Lynds & Hajek, 2006; McLaurin & Steel, 2007) — we note that the full range of our reconstructed palaeoflow depths is typically 1–7 m and therefore agrees with this range. Meanwhile, channelized fluvial sandstone bodies are more extensively documented for the Blackhawk Formation and their heights offer a maximum limit on palaeoflow depths. Flood and Hampson (2015) recovered mean apparent heights for channelized sandstone bodies of 6–8 m across the entire Blackhawk Formation between Straight Canyon and Salina Canyon. As maximum bounds on palaeoflow depth, these values are also in good agreement with the upper bounds of estimated palaeoflow depths.

(B) Palaeoslopes and river long profiles

Palaeoslope estimates for our northern (Fig. 7a–f) and southern (Fig. 7g–m) transects and results from each method (Equations 3 and 4) were compared (Fig. 7). Palaeoslopes are presented as y/x — a palaeoslope of 0.001 results in an elevation decrease of 1 m per 1000 m and is equivalent to 0.057°. Maximum (up-dip) palaeoslopes of 5 $\times 10^{-3}$ are equivalent to slopes of ~0.3°; these magnitudes of palaeoslope are comparable with the slopes of modern rivers, including middle–upper reaches of the Colorado (USA) and upper reaches of the Niger (west Africa) (Roberts et al., 2012; Paul et al., 2014; Fernandes et al., 2019). Minimum (down-dip) palaeoslopes of ~5 $\times 10^{-5}$ are equivalent to slopes of ~0.003°; palaeoslopes in the range 10^{-5} to 10^{-4} are characteristic of lowland/low-slope rivers, such as lower reaches of the Mississippi (USA), Ebro (Spain), Nile (northeast Africa) and Murray–Darling (Australia) (Carlston, 1969; Rudge et al., 2015; Fernandes et al., 2019; Roberts et al., 2019; Soria-Jáuregui et al., 2019).

Up-dip, palaeoslopes are consistently of order 10^{-3} (Fig. 7), with the exception of the Blackhawk Formation in the southern transect where 1st–3rd interquartile range of recovered palaeoslope values extends down to 7 $\times 10^{-4}$ (Fig. 7k–m). Importantly, an order of magnitude decrease in palaeoslope is reconstructed between a down-system distance of 10 and 25 km; this occurs in all stratigraphic intervals, at the same downstream distance, for both the northern and southern transects (Fig. 7). Down-dip, from ~25 km onwards, palaeoslopes are flatter and typically span 5 $\times 10^{-5}$ to 5 $\times 10^{-4}$. In these lower gradient regions, there is an apparent down-dip increase in palaeoslope in Fig. 7b,c,i–m. However, this apparent increase is within the 1st–3rd interquartile range of values and may not be significant. Up-dip to down-dip palaeoslope estimates derived from Equations 3 and 4 are broadly consistent with one another — they are the same order of magnitude and the 1st–3rd interquartile ranges either overlap with, or are within a factor of 2–3 of, one another. However, Equation 3

overpredicts and underpredicts palaeoslope relative to Equation 4, such that palaeoslope estimates derived from Equation 3 imply higher topographic relief and estimates derived from Equation 4 imply lower topographic relief (Fig. 7).

To constrain temporal changes in palaeoslope, the palaeoslope evolution at the most up-dip locations of both the northern and southern transects can be compared (Fig. 8). Palaeoslopes increase at the onset of Castlegate Sandstone deposition (intervals 4–6) and the magnitude of this increase differs between the north and the south (Fig. 8). In the north, the initial palaeoslope is higher (~2 $\times 10^{-3}$) and increases by a factor of 1.5 to ~3 $\times 10^{-3}$ (Fig. 8a), whereas, in the south, the initial palaeoslope is lower (~1 $\times 10^{-3}$) and increases by a factor of up to 4, to ~4 $\times 10^{-3}$ (Fig. 8b). This implies a coeval increase in palaeoslope at the onset of Castlegate Sandstone deposition which was more pronounced in the south. Again, estimates derived from Equation 4 dampen this increase relative to estimates derived from Equation 3.

With up-dip to down-dip palaeoslope estimates for both the northern and southern transects, best-fit palaeoslope profiles were derived as a function of downstream distance (Equation 7; Supplementary Table S6). Palaeoslope profiles generally fit reconstructed palaeoslopes well, with typical R^2 values >0.85, and it is noted that of 3 reference concavities, θ, used, the higher value of θ=0.6 typically recovered the best fits (Supplementary Table S6). A notable exception to this is palaeoslope profiles reconstructed from Shields stress palaeoslope estimates for the Castlegate Sandstone in the northern depositional-dip transect — the lower θ=0.4 value generates the best fit and this fit is relatively poor (R^2 of 0.35–0.6). However, palaeoslope profiles for these same space–time intervals derived from alternative palaeoslope estimates (Equation 4) fit well (R^2 >0.9; Supplementary Table S6).

In reconstructing palaeoslope profiles steepness index, k_s, values were recovered for each stratigraphic interval (for θ=0.5), which were mostly between ~5 and 35 m (Supplementary Table S6). There is an increase in reconstructed k_s values across the Blackhawk–Castlegate transition for both methods of palaeoslope estimation. For estimates derived from Equation 3, k_s values increase across the Blackhawk–Castlegate transition by a factor of ~2–3 in the northern transect, and by a factor of ~4–5 in the southern transect. In contrast, for estimates derived Equation 4, k_s values increase across the Blackhawk–Castlegate transition by a factor of <1.5 in the northern transect, and by a factor of ~2 in the southern transect (Supplementary Table S6).

Palaeoslope profiles were transformed into river long profiles, which are indicative of the palaeorelief in the alluvial domain, or depositional reaches, of Blackhawk–Castlegate–Price River fluvial systems only (Fig. 9). Given that the concavities of these ancient rivers are not known, implementing plausible concavities of 0.4, 0.5 and 0.6 enabled a likely spread of values for palaeorelief to be constrained (Fig. 9). Results indicate that different concavities recover similar values for palaeorelief; total estimates vary within a factor of ~2, between a concavity of 0.4 and 0.6 (Fig. 9).

Using palaeoslope estimates derived from Equation 3, palaeorelief during Blackhawk deposition was estimated as ~40–60 m in the northern transect (Fig. 9e,f) and 15–25 m in the southern transect (Fig. 9k–m). During Castlegate Sandstone deposition, palaeorelief increased by a factor of 1.5–2.5 in the northern transect, to an estimated 65–145 m of palaeorelief, whereas it increased by a factor of 5–6 in the southern transect, to an estimated 90–130 m of palaeorelief. Alternatively, using palaeoslope

553 estimates derived from Equation 4, palaeorelief during Blackhawk Formation deposition was
554 estimated as ~30–50 m in the northern transect (Fig. 9e,f) and 15–25 m in the southern transect (Fig.
555 9k–m). During Castlegate Sandstone deposition, palaeorelief increased by a factor of ~1.8 in the
556 northern transect, to an estimated 55–90 m of palaeorelief, whereas it increases by a factor of 2 in
557 the southern transect, to an estimated 30–50 m of palaeorelief. In detail, palaeorelief implied by
558 Equation 3 (Shields) is up to a factor of 2 greater than the palaeorelief implied by Equation 4
559 (Trampush). This higher palaeorelief during Castlegate Sandstone deposition is sustained into Price
560 River Formation times. It is stressed that these estimates refer to the alluvial domain only.

561 ***(B) Hydrodynamics and sediment transport***

562 Median flow velocities of 0.8 m/s, with a median plausible range of 0.4–1.6 m/s, are deduced across
563 all field data (Fig. 10a), as well as median unit discharges of 2.5 m^2/s with a median plausible range of
564 1–10 m^2/s (Fig. 10b). Using plausible single-thread channel widths of 100–500 m at down-dip locations
565 (see Planform morphologies), this would imply median total discharges between 250–1250 m^3/s,
566 which is comparable with total discharges of well-known North American rivers such as the Platte,
567 Hudson, Colorado, Arkansas and Susquehanna. However, if multi-thread rivers are assumed to possess
568 >1 branch/braid, total discharges would have been several times greater. With a reconstructed
569 increase in palaeoslope at the Blackhawk–Castlegate transition, a coeval increase in flow velocities
570 and unit water discharges is expected analytically. Here, across all up-dip field areas, flow velocities
571 are overall greater during Castlegate Sandstone deposition, up to a factor of 2 to 3 (Fig. 10c), relative
572 to Blackhawk Formation deposition, whereas down-dip flow velocities are broadly the same through
573 time (Fig. 10d). Both up-dip and down-dip, unit water discharges overall do not change at the
574 Blackhawk–Castlegate transition (Fig. 10e,f). To offer a specific example for the Blackhawk–Castlegate
575 transition (intervals 3 and 4), at Mellor Canyon, median flow velocity, U, increased from 1.9 to 3.0 m/s,
576 and median unit water discharge, Q, only increased marginally from 4.4 to 4.6 m^2/s.

577 Reconstructed Rouse numbers, Z, indicate that dominant transport modes of bed-material varied in
578 space and time (Fig. 11). Up-dip field sites consistently exhibit high Z values for both the median and
579 1st–3rd interquartile range, indicating predominant bedload transport (Fig. 11). Median Z values then
580 decrease by a downstream distance of 30 km, indicating local transition to predominantly mixed load
581 systems, however the likely spread of values indicated by the interquartile ranges implies that
582 dominant transport modes at this downstream distance may have spanned both mixed load and a
583 near entirely suspended load (Fig. 11). A crucial exception to this observation is for Castlegate
584 Sandstone deposition in the southern transect (intervals 4–6) where, at a downstream distance of 30
585 km, median Z values suggest bedload remains the most important transport mode (Fig. 11g–i). At
586 downstream distances associated with the most down-dip field sites, median Z values have further
587 decreased, however 1st–3rd interquartile ranges mostly still span both the mixed load and entirely
588 suspended load domains.

589 The inferred dominant sediment transport modes are corroborated with results in Fig. 12, in which
590 Shields stress, τ^*, is plotted as a function of particle Reynolds number, Re_p, for each field site. These
591 data are plotted alongside observed data that are characteristic of suspended load, mixed load and
592 bedload regimes (Leopold & Wolman, 1957; Schumm, 1968; Chitale, 1970; Church & Rood, 1983;
593 Andrews, 1984). Up-dip field sites (Dry Canyon, Lake Fork, Mellor Canyon) plot among secondary data
594 that are typical for bedload rivers, meanwhile all other field sites plot in the mixed-load realm (Fig.

12). Of field sites dominated by a mixed load, data from Sixmile Canyon and Straight Canyon plot closest to the bedload realm, which is consistent with observations in Fig. 11, where results suggest that bedload transport remained important in the southern transect during Castlegate Sandstone deposition (intervals 4–6). Overall, results in Fig. 12 suggest that, down-dip, field sites are firmly in the mixed load range — it is unlikely that bed-material loads were predominantly suspended. In contrast, the 1st–3rd interquartile ranges in Fig. 11 suggest that dominant sediment transport modes may have spanned the mixed load/predominantly suspended domain. Down-dip, all field sites straddle the bounds between the stability fields for ripples and dunes and upper-stage plane beds (Fig. 12), which implies unidirectional flow and high sediment transport rates (both suspended transport and bedload transport).

(B) Planform morphologies

Finally, these data provide insights into the implied planform morphology of these ancient fluvial systems. However, to do this effectively estimates of palaeochannel widths are needed. Widths are difficult to constrain with confidence from field observations, and estimates from empirical scaling relations are tentative. Assuming single-thread channels, reconstructed median flow depths of 2–4 m might suggest channel widths of order 30–110 m and, using the upper bound of the 1–7 m range, widths up to ~300 m (following Bridge and Mackey (1993)). In contrast, if multi-thread channel belts are assumed, then channel belt widths of order 90–200 m, and up to ~400 m, might be expected (following Leopold and Maddock Jr (1953)).

For a range of possible widths, palaeoslope/Froude ratios were plotted against channel depth/width ratios (cf. G. Parker, 1976; Ganti et al., 2019b) (Fig. 13). Results imply that, for Blackhawk–Castlegate–Price River fluvial systems, single-thread planforms would be stable at channel widths <1 km; channel and channel-belt widths >1 km would have been required to instigate formation of bars and support transition to multi-thread systems, forming vast channel-belt complexes (Fig. 13a–d). However, planform reconstructions are very dependent on grain-size, a factor which is often not evaluated systematically. Bulk grain-sizes were used in initial calculations (Fig. 13a–d; see Methods). However, when using gravel-fraction grain-sizes, which can be associated with tectonic or climatic perturbations (e.g. increased palaeoslope or high-magnitude low-frequency discharge events), the results show that multi-thread planforms were more likely (Fig. 13e–h). For gravel-fraction grain-sizes, results imply that single-thread planforms were likely stable at channel widths <500 m, and that channel and channel-belt widths >500 m would have supported transition to multi-thread systems (Fig. 13b).

Of the Blackhawk–Castlegate–Price River fluvial systems, field results for the Castlegate Sandstone plot closest to the single-thread–multi-thread transition, whereas field results for the Price River Formation plot furthest from this transition (Fig. 13). This indicates the relatively high propensity of Castlegate fluvial systems to braiding, relative to Blackhawk and Price River systems.

(A) Discussion

(B) What did Campanian palaeorivers look like?

These analyses provide new insights that build on previous work characterising ancient rivers in the Campanian of central Utah as a series of distinct parallel transverse systems draining the Sevier front (Robinson & Slingerland, 1998; Bartschi et al., 2018; Chamberlin & Hajek, 2019; Pettit et al., 2019).

These rivers traversed a low-gradient landscape; alluvial relief was 10s of metres to c. 100 m, and the length scale of the alluvial domain (i.e. the distance from fan apexes to the palaeoshoreline) varied from as little as ~70 km during lower Blackhawk Formation deposition, up to and in excess of 250 km during Price River Formation deposition (Hettinger & Kirschbaum, 2002; Aschoff & Steel, 2011a; Hampson et al., 2012; Hampson et al., 2013). Relief was 10s of metres during Blackhawk deposition, when the length scale of the alluvial domain was at its narrowest. At the onset of Castlegate Sandstone deposition an increase in palaeoslope is documented, with palaeorelief increasing to c. 100 metres, which persisted into Price River deposition (Figs 7–9). For comparative purposes, such values of palaeoslope and palaeorelief are characteristic of the Mississippi river and downstream reaches of its principal tributaries e.g. the Missouri, Tennessee, Arkansas and Red rivers (Carlston, 1969; Fernandes et al., 2019).

Results imply that palaeoriver morphologies were similar in space and time, with palaeoflow depths of order 2–4 m (Fig. 6). Previous detrital zircon results suggest that northerly field sites (Price Canyon and Wattis Road) represent smaller transverse systems and that southerly field sites (Straight Canyon, Link Canyon and Salina Canyon) represent larger systems that include a longitudinal drainage component (Bartschi et al., 2018; Pettit et al., 2019). These results indicate that size disparities between these 5 systems were not statistically significant — reconstructed variations in palaeoflow depths are within the full range of plausible values. However, palaeoflow depths appear to have been marginally greater in southerly systems (Fig. 6). If true, this may be attributed to the possible longitudinal drainage component (Bartschi et al., 2018; Pettit et al., 2019).

Comparisons with modern rivers suggest that these 5 parallel palaeorivers (being ~25 km apart) were substantial systems. Reconstructed hydrodynamic properties, such as flow velocities and unit water discharges, are consistent with the ranges of values of modern systems with similar outlet spacings and similar distances to range fronts (Perry et al., 1996; Schulze et al., 2005; Milliman & Farnsworth, 2013; Global Runoff Data Centre). Notably, unit discharges are overall constant in time — there is no apparent increase in unit discharge at the Blackhawk–Castlegate transition (coeval with palaeoslope increase). This raises questions as to the nature of down-system width evolution and has implications for total discharge — plausible single-thread river widths of 100–500 m at down-dip locations would imply median total discharges of 250–1250 m^3/s.

Bedload transport was dominant at gravel-dominated up-dip localities, as expected, and suspended- and mixed-load systems prevailed further down-dip, with some localised variations (Figs 11, 12). For example, results highlight the importance of bedload transport during Castlegate Sandstone deposition in the southern transect (Figs 11, 12). With this information it is possible to map out how river behaviour varied spatially within catchments, and this informs best practices when it comes to reconstructing sediment discharges. This is especially important where interested in reconstructing the entire sediment load of an ancient system. For instance, channel palaeohydrologic approaches are often used to reconstruct sediment discharges in ancient source-to-sink systems (Holbrook & Wanas, 2014; Lin & Bhattacharya, 2017; Sharma et al., 2017), however these reconstruction tools solely reconstruct the bedload fraction and the suspended fraction of the bed material load (van Rijn, 1984b; Wright & Parker, 2004), i.e. the portion of the suspended load that interacts with the bed. As such, these reconstruction tools are not appropriate, by themselves, for reconstructing the total sediment load of a wash load-dominated system, for example. Knowledge of prevailing sediment transport

modes is important for evaluating whether different sediment discharge reconstruction methods are consistent with one another, as studies that reconstruct sediment discharges often corroborate results with an independent approach (Lin & Bhattacharya, 2017; Watkins et al., 2018; Zhang et al., 2018; Brewer et al., 2020; Lyster et al., 2020).

Here, reconstructions of planform morphology, following G. Parker (1976), and assuming channel widths <1 km, imply that single-thread rivers would have prevailed throughout Blackhawk–Castlegate–Price River deposition. Localized or intermittent transitions to braided planforms may have been associated with tectonic or climatic perturbations, such as increased palaeoslope or high-magnitude, low-frequency discharge events (Fig. 13). In detail, these perturbations (which can be associated with the gravel-fraction grain-size) can support braiding at narrower channel/channel-belt widths of order 500 m. Of these fluvial systems, Castlegate systems had a higher propensity to braiding. At this point, it is important to flag that traditional bipartite classification of fluvial systems aims to define fluvial systems as either straight/meandering or braided/anabranching end members (Leopold & Wolman, 1957). However, these are not mutually exclusive; both straight/meandering and braided/anabranching planforms can co-exist at reach scales. These reconstructions can be contextualised by field evidence; however, field observations point to a discrepancy and this topic is returned to in the final discussion section.

To create a holistic view as to the nature of these ancient fluvial landscapes, various modern analogues can be considered. In the Amazon basin, several of the most up-system tributaries axially drain the central and eastern Andean cordillera. For example, the Huallaga river, Peru, is an axial river fed by transverse systems draining the eastern Andean range front. These transverse rivers have regular outlet spacings, channel-belt widths of order 100s of metres (up to 1 km), and combine both single- and multi-thread planforms which vary at reach-scales. In the eastern Himalayas, transverse systems draining the range front into the axial Brahmaputra (Assam Valley) provide another modern analogue for the pattern and style of these ancient fluvial systems, despite the larger scale of this system.

(B) What drove spatio-temporal changes in morphologic properties?

A key result in this study is quantification of an increase in palaeoslope at the Blackhawk–Castlegate transition by a factor of 1.5–4, as well as the associated increase in palaeorelief (Figs 7–9). Increased palaeoslopes have implications for the morphologic and hydrodynamic properties of these palaeorivers, including their flow velocities and unit discharges. In this study, the increase in palaeoslope and palaeorelief implies that rivers were actively responding to changes in uplift rate in the hinterland region.

At the Blackhawk–Castlegate transition, palaeorelief increased from 10s of metres to c. 100 m (Fig. 9). An important point to remember is that these estimates are specific to the alluvial domain only. Behind the Sevier front, existence of a high-elevation plateau known as “Nevadaplano” is inferred (Allmendinger, 1992; DeCelles, 1994, 2004; DeCelles & Coogan, 2006), which has been likened to the modern high-elevation plateau, Altiplano, of the central Andes. Palaeo-elevations in the Sevier highlands and Nevadaplano are argued to be 3 to >4 km — these values have been deduced from a combination of climate modelling studies (Sewall & Fricke, 2013; Foreman et al., 2015), kinematic reconstructions (DeCelles, 1994, 2004; DeCelles & Coogan, 2006) and other data, including palaeoflora (Chase et al., 1998). Here, alluvial palaeorelief of order 100 m is reconstructed. Given that the low-

lying alluvial domain of these palaeorivers has a length scale of order 70–250 km, and given proximity to high-elevation Sevier highlands, the entire river long profile is inferred to have likely been highly concave. This is supported in part by the fact that, in reconstructing palaeoslope profiles, the best fits were recovered when using a higher reference concavity of 0.6 (Supplementary Table S6). If best-fit palaeoslope profiles were projected up-dip into the Sevier hinterland, palaeoslopes of 10^{-1} might be reached within as little as 10 km of the most up-dip field area, and therefore elevations in excess of 1 km might be reached within a further 10 km. To again use the modern Andes as an analogue, a longitudinal river profile from the Peruvian shoreline to the western Andean cordillera and Altiplano would have a length scale of 50–150 km, with 0.5–1 km of relief in the alluvial domain and elevations >3 km in the western cordillera and Altiplano. With a similar tectono-geographic setting in Late Cretaceous Utah, this comparison can also be used to highlight the potential high concavity of these ancient river profiles.

In reconstructing palaeorelief, steepness indexes, k_s, were also recovered for northern and southern transects (Equations 5 and 6) (Supplementary Table S6). While k_s was solved for using field data and a nonlinear least squares regression, k_s values are often estimated (albeit tenuously) as a function of known uplift rate and erodibility in bedrock channels, but additionally (although less frequently) in downstream alluvial reaches (Kirby & Whipple, 2012; Pederson & Tressler, 2012; Stucky de Quay et al., 2019). Inversely, where k_s can be measured, and where erodibility is known, first-order estimates of uplift rate can be made. Steepness indexes recovered in this study were typically ~5–35 m (for a reference concavity, θ, of 0.5) and, despite unknown erodibility, global data compilations indicate that low uplift rates of order 0.01–0.1 mm/yr are generally associated with these kinds of values (Kirby & Whipple, 2012). Despite overall low k_s values, it is important to note the relative increase in k_s by a factor of <1.5 to 5 at the Blackhawk−Castlegate transition. While these are first-order estimates, and are derived solely for the alluvial domain, an increase in k_s (and palaeorelief) can be attributed to a relative increase in uplift rate in the hinterland region. Here, this increase might be attributed to frontal thrust migration, or thrust initiation in the Sevier highlands (DeCelles, 2004; DeCelles & Coogan, 2006). This includes Sevier shortening in the Charleston–Nebo Salient (CNS), an eastward convex portion of the Sevier thrust front in north-central Utah (Fig. 1b) (Bruhn et al., 1986; Bryant & Nichols, 1988; Constenius et al., 2003; Bartschi et al., 2018), which is commonly attributed to the influx of quartzite-dominated coarse-grained detritus associated with Castlegate Sandstone progradation (Robinson & Slingerland, 1998; Horton et al., 2004). For Castlegate Sandstone deposition in the northern transect, results show that palaeoslope profiles did not fit reconstructed palaeoslopes well and favoured lower concavities (which also did not fit well). Our interpretation is that shortening in the CNS, which has been structurally linked with coeval basement Laramide uplifts in northern Utah (Bruhn et al., 1986; Bryant & Nichols, 1988; Constenius et al., 2003; Bartschi et al., 2018), may have significantly influenced river long profiles associated with northerly Castlegate fluvial systems near Price, and locally lowered their concavities. Whereas ~60 km south in the southern transect, higher concavity values of 0.6 deliver best fitting palaeoslope profiles through all 7 stratigraphic intervals (Supplementary Table S6).

While tectonic drivers are commonly attributed to variations in channel steepness (Kirby & Whipple, 2001; Kirby et al., 2003; Wobus et al., 2006; Boulton & Whittaker, 2009; DiBiase et al., 2010), climatic drivers, especially precipitation rates, also play a crucial role but are notoriously difficult to disentangle from their tectonic counterpart (Wobus et al., 2010; DiBiase & Whipple, 2011; Champagnac et al.,

2012; Whittaker, 2012; D'Arcy & Whittaker, 2014). The role of climate is important to consider here, given the assumed monsoonal climate and, therefore, highly seasonal discharge variability (Roberts, 2007; Roberts et al., 2008; Fricke et al., 2010; Sewall & Fricke, 2013). Previous work shows that precipitation rates have a discernible role on steepness indexes (Champagnac et al., 2012; D'Arcy & Whittaker, 2014); analytically, an increase in channel steepness and palaeoslope can be attributed to a decrease in precipitation rate (to maintain similar total water discharge) (D'Arcy & Whittaker, 2014). To reduce palaeoslopes by a factor of 2 precipitation rate must typically be quadrupled (D'Arcy & Whittaker, 2014). Despite the supposed warm and wet climate (L. R. Parker, 1976; Kauffman & Caldwell, 1993; Roberts & Kirschbaum, 1995), few workers have argued for, or investigated, the possibility of increased aridity at the Blackhawk–Castlegate transition (van Wagoner, 1995; Adams & Bhattacharya, 2005). In theory, increased palaeoslopes can be explained by decreased precipitation (D'Arcy & Whittaker, 2014), however, here, no decrease in either flow velocities or unit discharges is reconstructed at the Blackhawk–Castlegate transition (Fig. 10). Generally, in down-dip locations, flow velocities and unit discharges are constant across this interval (Fig. 10d,f). At up-dip field sites, however, flow velocities are overall slightly greater during Castlegate Sandstone deposition relative to Blackhawk Formation deposition, but unit discharges remain similar for both.

With unit discharges constant in space and time, the crucial unknown is palaeochannel width. At minimum, channel widths can be considered as broadly the same across the Blackhawk–Castlegate transition. During Blackhawk Formation deposition, channelized sandbody widths of order 350–420 m offer a maximum limit on palaeochannel widths (Hampson et al., 2013; Flood & Hampson, 2015). Meanwhile, during Castlegate Sandstone deposition, bar package widths are between ~60–180 m (Chamberlin & Hajek, 2019); assuming 2–3 threads, these bar widths might imply channel belt widths of order half a kilometre. However, planform stability estimates based on G. Parker (1976) indicate that these rivers could have possessed anywhere between 1–10 threads (Fig. 13), which could result in channel-belt widths up to and in excess of 1 km. At maximum, this implies increased channel widths at the Blackhawk–Castlegate transition. Unless a significant decline in river widths is projected, then field results do not directly support a climatic driver. Consequently, our interpretation is that increased channel steepness and palaeoslope at the Blackhawk–Castlegate transition is due to tectonically driven uplift in hinterland regions.

(B) Effectiveness of palaeohydrological and palaeomorphological reconstructions

While quantitative reconstructions have led to significant advances in both the quantity and level of detailed information that can be extracted from fluvial strata (e.g. Ganti et al., 2019a), it is unclear how accurately these tools characterise ancient systems. Addressing this question is particularly important as sedimentology becomes increasingly numerical and it becomes easier to apply quantitative tools to stratigraphy (Duller et al., 2010; Whittaker et al., 2011; Holbrook & Wanas, 2014; Ganti et al., 2019b). With extensive existing work on Late Cretaceous fluvial systems of central Utah, results in this study offer a unique opportunity to highlight consistencies and discrepancies between quantitative interpretations of fluvial palaeohydrology and more qualitative field-based facies and architectural interpretations.

To first order, whether point reconstructions of various morphologic and hydrodynamic parameters agree with qualitative interpretations can be evaluated using independent proxies (derived from field measurements or facies interpretations). As previously mentioned, reconstructed flow depths agree

with several secondary observations of bar heights (Adams & Bhattacharya, 2005; Lynds & Hajek, 2006; McLaurin & Steel, 2007; Hajek & Heller, 2012; Chamberlin & Hajek, 2019) (Supplementary Table S4), which can be used as a direct proxy for flow depth (Bridge & Tye, 2000; Hajek & Heller, 2012). This agreement indicates that the uncertainty estimator in Equation 2 is reasonable, and that cross-set heights can therefore be used to reconstruct reasonable flow-depth constraints and are useful as a bedform-scale approach. Such an approach is particularly useful in core data, locations with limited outcrop exposure, or deposits where the degree of bar preservation is poor. It is noted that scaling relations that relate cross-set heights with original bedform heights (and subsequently formative flow depths) are derived from theory and experiments that assume statistical steady state, in which flow is constant (Paola & Borgman, 1991; Leclair, 2002; Jerolmack & Mohrig, 2005). As such, agreement of flow depth reconstructions with bar heights might therefore imply that these dunes were formed in steady flow conditions (Ganti et al., 2020). This contrasts with literature that alludes to the preferential preservation of dunes in unsteady flow conditions (Reesink & Bridge, 2007; Reesink & Bridge, 2009; Reesink et al., 2015; Leary & Ganti, 2020), and merits further work regarding the kinematic controls on dune preservation in this region.

For more complex palaeohydrologic reconstructions, such as palaeoslopes and palaeorelief (Figs 7–9), it is not possible to directly corroborate estimates with independent proxies derived from field data. Nevertheless, it is still possible to evaluate reconstruction tools by contrasting commonly used methods. In this study the first approach used a theoretically-based Shields stress inversion (Equation 3), whereas the second approach used the empirically-derived model (Equation 4) of Trampush et al. (2014). Palaeoslope estimates derived from each approach are in broad agreement with one another. Each method typically recovers estimates of the same order of magnitude — in many cases the interquartile ranges of values overlap, and, in all cases, the full ranges of plausible values overlap (i.e. the whiskers in Fig. 7 and 8). These point comparisons between the 2 methods are promising, and in line with comparisons made elsewhere (e.g. Ganti et al., 2019a). However, there are implications when larger spatial scales are concerned, imparting uncertainty that must be carried forward in interpretation of palaeorelief in the depositional reaches of these systems. Along the northern and southern transects, Shields stress inversion estimates consistently show higher differences in palaeoslope (i.e. higher slopes up-dip and lower slopes down-dip) relative to palaeoslopes derived from the Trampush et al. (2014). This difference is likely an outcome of the Trampush et al. (2014) method using a continuous function to estimate slope, whereas the Shields stress inversion relies on a step-change empirical estimate for gravel or sand-bed rivers. Regardless of the method used, palaeoslope reconstructions are dependent on grain-size and flow-depth estimates. Because flow depths did not appreciably change in Blackhawk and Castlegate palaeorivers, variations in reconstructed slopes and derivative estimates (e.g. water and sediment discharge) are largely driven by observed differences in grain-size.

Despite the differences of the 2 methodologies on palaeorelief, estimates of palaeorelief can be compared with relief in modern systems possessing similar tectono-geographic set-ups. Palaeorelief estimates between 50 and 100 m in depositional reaches of these ancient fluvial systems are reasonable when compared with relief in modern systems with a similar tectono-geographic setting. For example, one can return to the Andean analogue, but cross over to the eastern Andean cordillera and into the foreland basin and low-lying plains of the Amazon river. For most of its course, the

Amazon long profile has a relief of less than 100 m (Milliman & Farnsworth, 2013) — relief only exceeds 100 m in proximity to the range front (Milliman & Farnsworth, 2013).

Finally, these results complement field evaluation of the nature of Blackhawk Formation and Castlegate Sandstone planforms, but also raise new questions. Channelized sandstone bodies of the Blackhawk Formation are typically 350–420 m wide (Adams & Bhattacharya, 2005; Hampson et al., 2013; Flood & Hampson, 2015), although a small proportion are much larger and some exceed 1 km (Flood & Hampson, 2015). These sandstone bodies offer a maximum cap on palaeoflow width. The Blackhawk Formation is considered to mostly represent single-thread systems, which results in this study agree with. However there is significant field evidence that many channelized sandstone bodies of the Blackhawk Formation represent multi-thread systems with mid-channel bars, based on bar facies observations (Adams & Bhattacharya, 2005; Hampson et al., 2013; Flood & Hampson, 2015). Field observations of multi-thread Blackhawk fluvial systems of order 100s of metres are inconsistent with our results, which suggest multi-thread systems would not have been stable (Fig. 13). Meanwhile, the Castlegate Sandstone is interpreted to be fully-braided from facies observations (Miall, 1993, 1994; Miall & Arush, 2001; McLaurin & Steel, 2007). Reported mean bar package widths of order 60–180 m for the Castlegate Sandstone (Chamberlin & Hajek, 2019) would imply total channel widths <1 km (assuming a few braids); our reconstructed planform stability estimates, which indicate that Castlegate systems should have been single-threaded, are again inconsistent with sedimentological facies and architectural interpretations. Other quantitative reconstructions of planform have contradicted traditional field-based facies observations (Ganti et al., 2019a), and these inconsistencies must be treated carefully. The main limitation to reconstructing ancient channel planforms is a lack of reliable methods for estimating palaeochannel widths. Interpreting palaeochannel planforms from facies associations and stratigraphic-architectural data is not trivial, particularly where outcrop is limited or where observations are equivocal. But, in this case, a number of workers have concluded that braided conditions prevailed at the time of Castlegate Sandstone deposition (Lawton, 1986b; Miall, 1994; van Wagoner, 1995; Miall & Arush, 2001) and occurred at times during Blackhawk Formation deposition (Adams & Bhattacharya, 2005; Hampson et al., 2013; Flood & Hampson, 2014, 2015). As such, it can be argued that further detailed work to test and reconcile facies-based and hydraulically derived interpretations of channel planforms is a pressing research goal.

(A) Conclusions

Here a four-dimensional reconstruction of palaeohydrology in Late Cretaceous palaeorivers of central Utah, USA, is presented, using field data and a well-established quantitative framework. Overall, fluvial morphologies were similar in space and time, although marginally greater reconstructions of flow depths in southerly systems likely reflect the contribution of a longitudinal drainage component. The most prominent spatio-temporal change is an increase in palaeoslope at the Blackhawk–Castlegate transition by a factor of 1.5–4; this reflects an increase in palaeorelief (for the alluvial domain) from 10s of metres during Blackhawk Formation deposition up to, and in excess of, 100 m during Castlegate Sandstone deposition, which persisted into Price River Formation times. The observation that unit water discharges do not change at the Blackhawk–Castlegate transition does not support a climatically driven increase in palaeoslope and channel steepness. Results therefore point to a tectonically driven palaeoslope increase. In deciphering the relative role of tectonic and climatic drivers, the main limitation in this study is uncertainty in palaeochannel widths, which directly affect total water discharges. Palaeochannel width reconstructions therefore remain a prominent research challenge.

Results complement and expand on extensive facies-based interpretations of these systems, which offers unique opportunity to evaluate the efficacy of quantitative palaeohydrological reconstruction tools. Bedform-scale palaeoflow depth reconstructions are in good agreement with observations of preserved barforms. Moreover, while different palaeoslope reconstruction methods produce results that broadly agree, the results show that at larger spatial scales they over- and under-predict relief relative to one another, which has implications for quantifying alluvial palaeorelief and, therefore, the magnitude of change in relief at the Blackhawk–Castlegate transition. Finally, quantitative hydraulic reconstructions of planform somewhat disagree with facies-based interpretations. While this discrepancy ties back to uncertainty in palaeochannel widths, these results highlight that further work is required to reconcile hydraulically- and facies-based approaches in order to facilitate their application in the geological past.

Acknowledgements

This research was primarily funded by the Natural Environment Research Council (NERC) Science and Solutions for a Changing Planet Doctoral Training Partnership (DTP), with additional funding by The Geological Society of London and The British Sedimentological Research Group. We thank Christopher Dean for support with planning fieldwork, George Hedley for support with field data collection, and Stephen Watkins for useful discussions. We would also like to thank Robert Mahon and Sandra Mann for their constructive reviews, which greatly enhanced this manuscript.

Author Contributions

SJL and ACW designed the study. SJL, ACW and BAL conducted field data collection. SJL processed field data and results. SJL, ACW, GJH and EAH analysed and interpreted results. SJL wrote the manuscript. ACW, GJH, EAH and PAA all contributed significantly to the manuscript.

Data Availability

Field data available in article supplementary material.

Figures

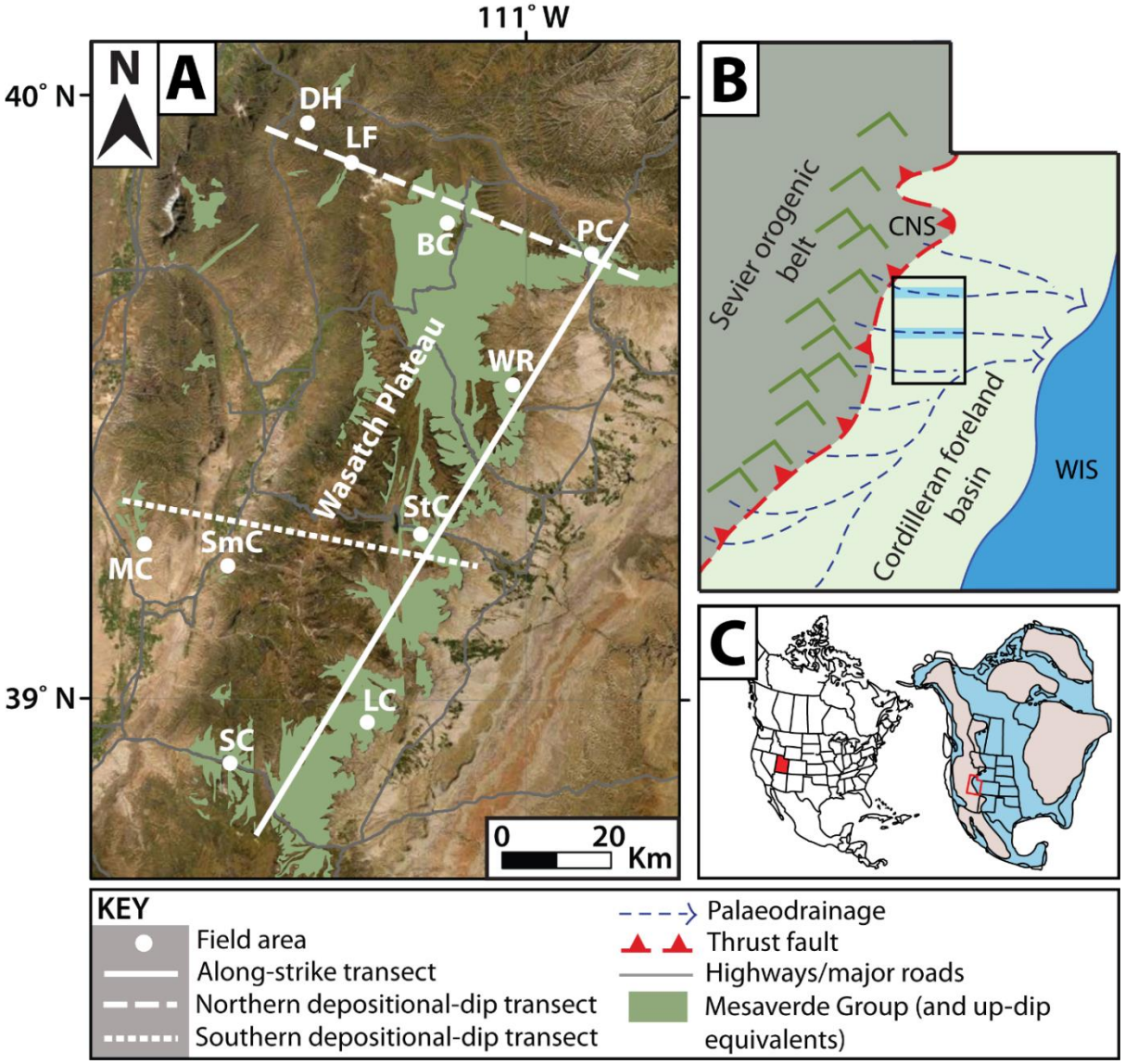

913

914 **Figure 1:** Study area. Part A) Field areas in central Utah, USA, which include Bear Canyon (BC), Dry
915 Hollow (DH), Lake Fork (LF), Link Canyon (LC), Mellor Canyon (MC), Price Canyon (PC), Salina Canyon
916 (SC), Sixmile Canyon (SmC), Straight Canyon (StC) and Wattis Road (WR). The solid white line indicates
917 the along-depositional-strike transect defined in this study, the dashed white line indicates the
918 northern depositional-dip transect defined in this study, and the dotted white line indicates the
919 southern depositional-dip transect defined in this study. Part B) A conceptual diagram of Utah
920 palaeogeography and palaeodrainage in the Campanian (Late Cretaceous). Likely configurations of
921 drainage toward the Western Interior Seaway (WIS) are indicated by dashed blue lines. CNS =
922 Charleston–Nebo Salient. The black outlined box indicates the study area (i.e. part A), and the two
923 highlighted drainage routes (shaded blue) represent the northern and southern depositional-dip
924 transects defined in this study (see part A). Part C) The location of Utah relative to the modern North
925 American continent (left) and the Late Cretaceous North American continent (right), which features
926 the Western Interior Seaway (blue). Utah is highlighted as a red box.

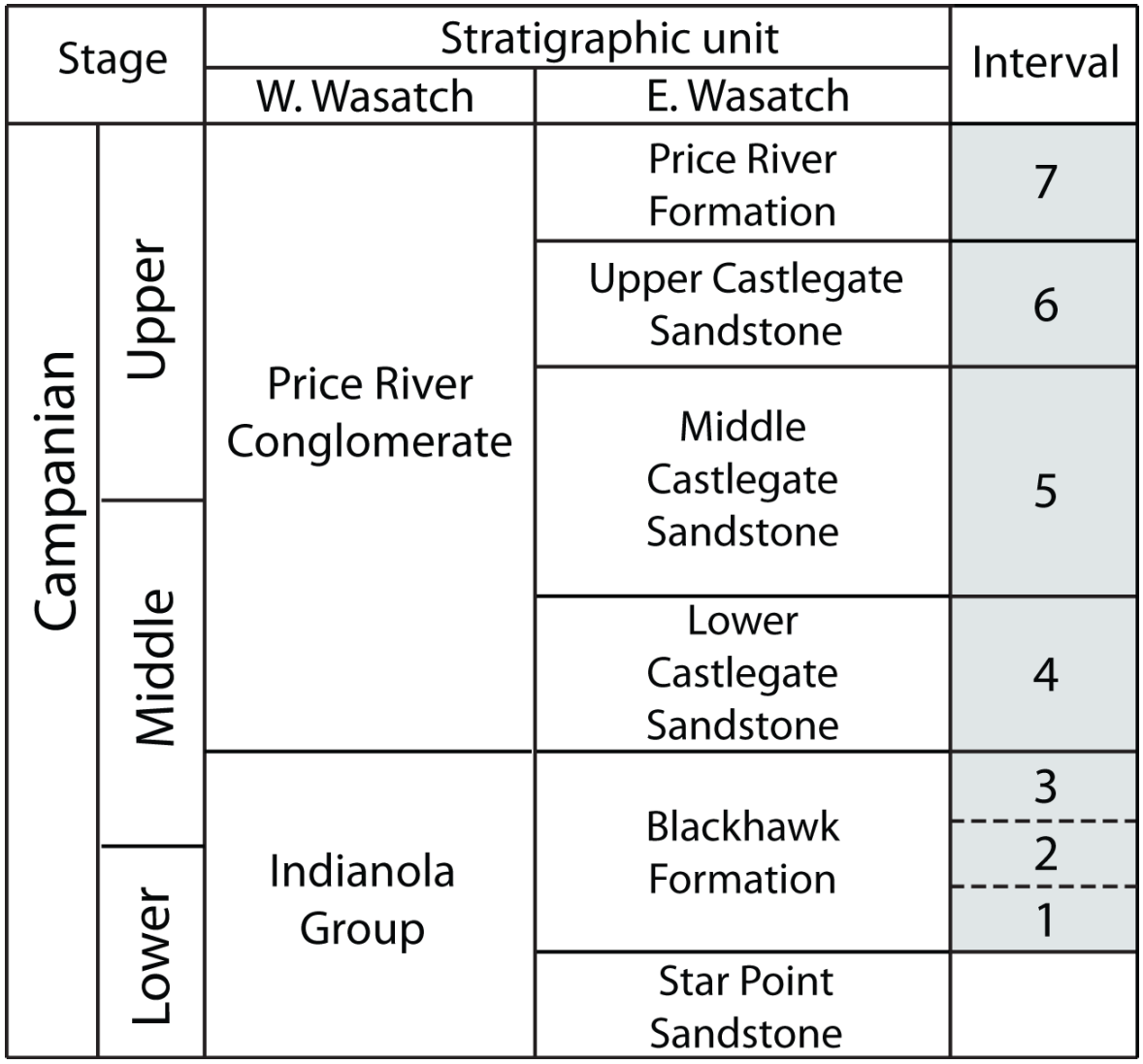

Figure 2: Regional stratigraphy and up-dip (western Wasatch Plateau) to down-dip (eastern Wasatch Plateau) stratigraphic correlation followed in this study. Shaded intervals indicate the stratigraphic intervals used in this study (note that they are not of equal duration). 1 = lower Blackhawk Formation; 2 = middle Blackhawk Formation; 3 = upper Blackhawk Formation; 4 = lower Castlegate Sandstone; 5 = middle Castlegate Sandstone; 6 = upper Castlegate Sandstone (Bluecastle Tongue); 7 = (lowermost) Price River Formation. Dashed lines indicate an approximate interval boundary. Modified and compiled using data from Fouch et al. (1983); Robinson and Slingerland (1998); Miall and Arush (2001); Horton et al. (2004); Cobban et al. (2006); Aschoff and Steel (2011a, 2011b); Bartschi et al. (2018). Price River Conglomerate nomenclature follows Aschoff and Steel (2011a, 2011b).

Figure 3: An overview of fluvial strata from which palaeohydrological field data were collected. Data were collected for 5 parallel palaeorivers in Late Cretaceous central Utah, USA. These 5 palaeorivers cropped out in canyons on the eastern front of the Wasatch Plateau — parts A and B show typical exposure of the Blackhawk Formation, Castlegate Sandstone, and Price River Formation in these canyons. Specifically, part A shows strata in Salina Canyon and part B shows strata in Straight Canyon (see Fig. 1), and dashed white lines indicate lithostratigraphic boundaries. For two of these 5 palaeorivers, data were additionally collected upstream to downstream along defined depositional-dip transects (see Fig. 1). Parts C–E show deposits on the northern depositional-dip transect. From up-dip to down-dip, part C shows debris flow facies of the Price River Conglomerate, part D shows amalgamated fluvial gravels and sands of the Castlegate Sandstone near Bear Canyon, and part E shows amalgamated fluvial sands of the Castlegate Sandstone in Price Canyon. Parts F–H show deposits on the southern depositional-dip transect, for older sediments. From up-dip to down-dip, part F shows channelized fluvial gravel–sand bodies of the upper Sixmile Canyon Formation in Mellor Canyon, part G shows a small channelized sandstone body of the upper Sixmile Canyon Formation in Sixmile Canyon, and part H shows a large channelized sand body of the Blackhawk Formation in Straight Canyon (in the background the Castlegate Sandstone is visible).

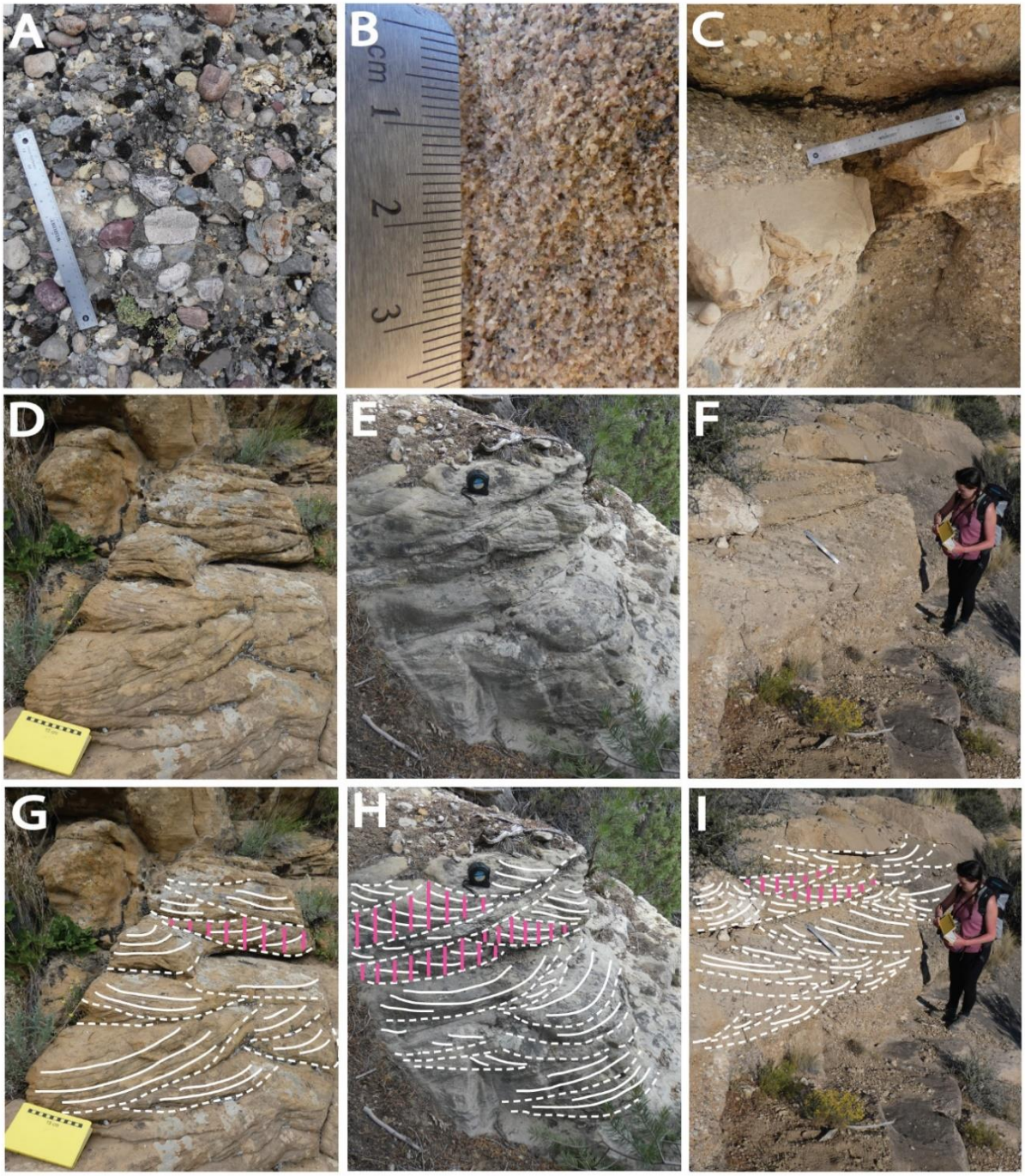

Figure 4: Field data collection included grain-size measurements for (part A) gravel and (part B) sand fractions, as well as (part C) estimates of the proportions of different grain-size facies. Parts D–F depict cross-bedding, and parts G–I depict interpreted versions of the same images. Dashed white lines indicate bounding surfaces of individual cross-sets and solid white lines indicate selected foresets within individual cross-sets. To exemplify sampling procedure when determining mean cross-set height, solid pink lines demonstrate how heights are measured for selected cross-set dip sections. Field notebook with 15 cm scale, tape measure, and 30 cm rule for scale.

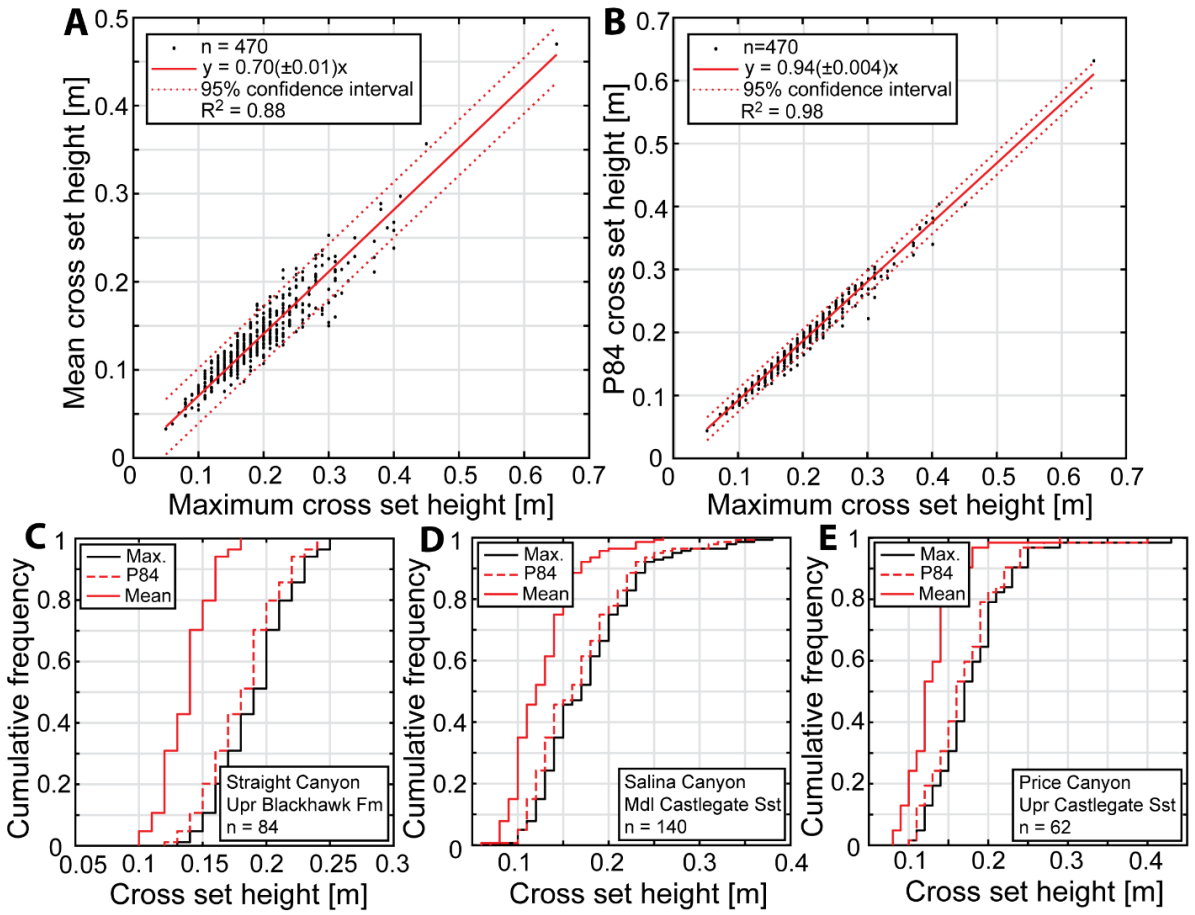

962

963 **Figure 5:** Part A) Relationship between maximum cross-set height and mean cross-set height. Part B)
964 Relationship between maximum cross-set height and the 84th percentile (P_{84}) of cross-set height. Data
965 are based on 470 measured cross-set distributions. Errors reported in the fits are 95% confidence
966 intervals. Parts C–E) Examples of the use of these new relations (parts A and B) to predict the mean
967 and P_{84} cross-set height from maximum cross-set heights. Examples are for the upper Blackhawk
968 Formation in Straight Canyon (part C), the middle Castlegate Sandstone in Salina Canyon (part D), and
969 the upper Castlegate Sandstone in Price Canyon (part E). In parts C–E, n indicates the number of
970 maximum cross-set heights used to predict mean and P_{84} cross-set heights. Full cross set data for each
971 field site, through each stratigraphic interval, are located in Supplementary Table S3.

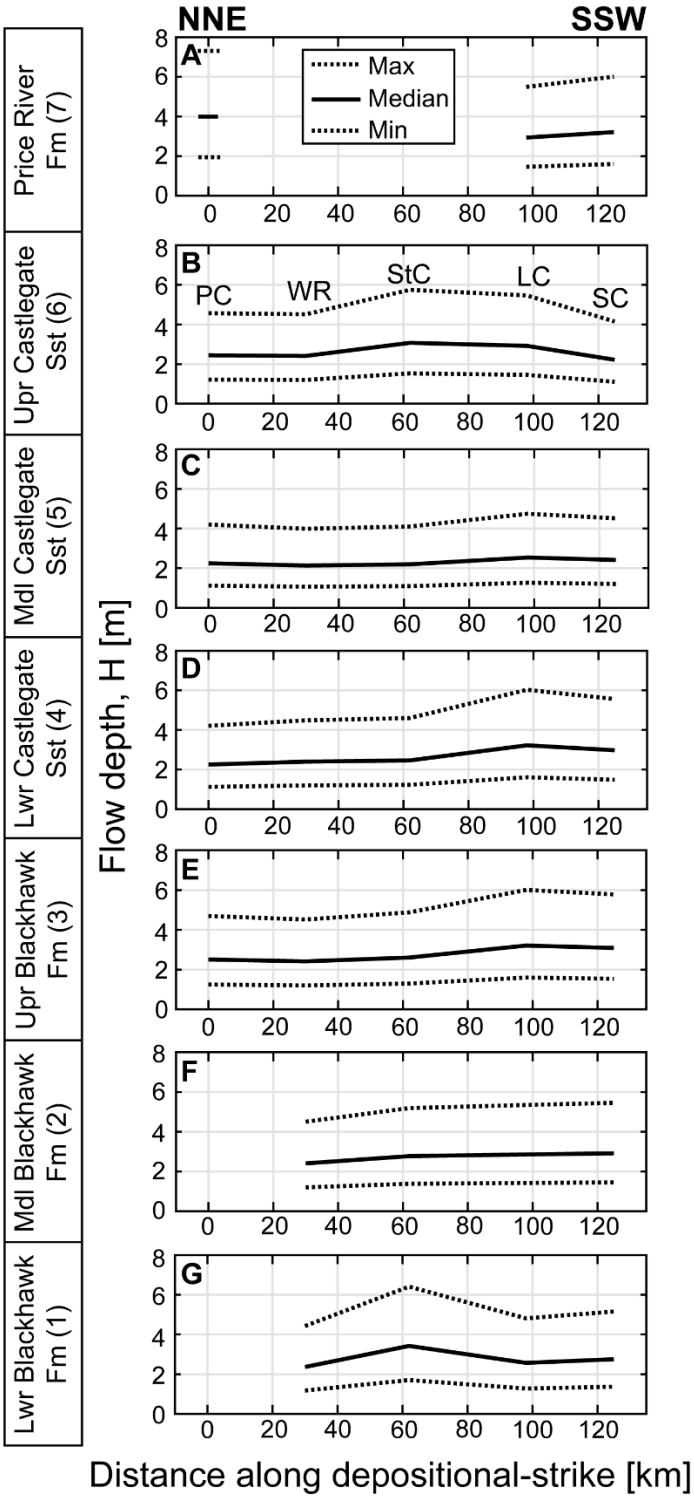

Figure 6: Reconstructed palaeoflow depths for the 5 parallel fluvial systems, for each stratigraphic interval (parts A–G), where possible, using mean cross-set heights. Results are presented as along-depositional strike transects from NNE (left; 0 km) to SSW (right; 125 km). Field sites span Price Canyon (PC), Wattis Road (WR), Straight Canyon (StC), Link Canyon (LC) and Salina Canyon (SC). Solid lines indicate median palaeoflow depths and dashed lines indicated plausible minimum and maximum values for median palaeoflow depths using uncertainty margins of Equation 2. This figure is replicated in the Supplement alongside palaeoflow depths reconstructed from maximum cross-set heights (Supplementary Fig. S5).

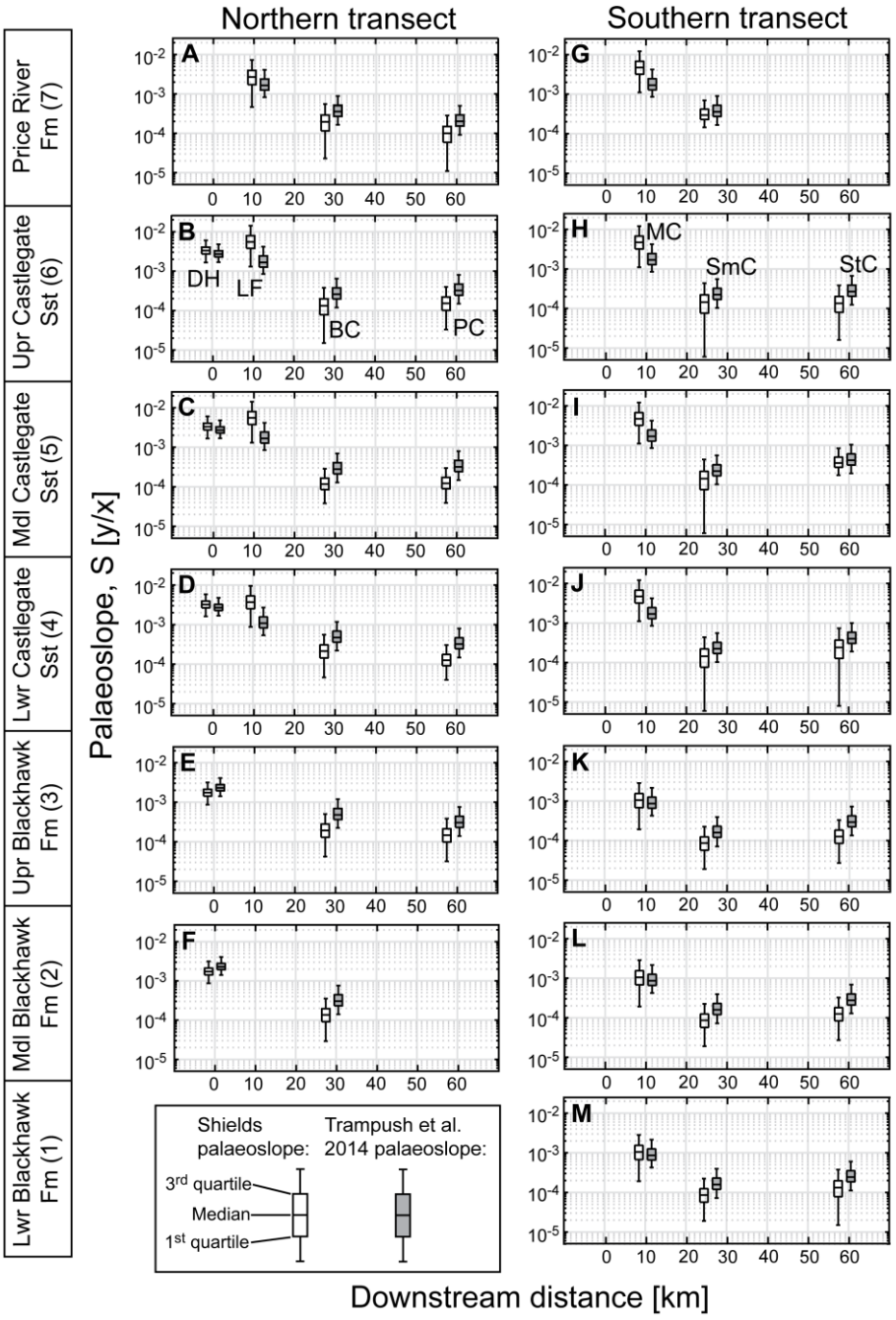

Figure 7: Up-dip to down-dip palaeoslope estimates for the defined northern and southern transects, using bulk grain-size data, for each stratigraphic interval (1–7), where possible. Parts A–F represent up-dip to down-dip palaeoslopes for the northern transect, from the middle Blackhawk Formation to the Price River Formation. Parts G–M represent up-dip to down-dip palaeoslopes for the southern transect, from the lower Blackhawk Formation to the Price River Formation. The central mark of each box indicates the median estimate, and the bottom and top edges of each box indicate the 1st and 3rd quartiles (or 25th and 75th percentiles), respectively. The whiskers extend to the most extreme estimates that are not considered to be outliers. Palaeoslope estimates are derived from 2 independent approaches; boxes with no fill indicate estimates of palaeoslope derived using a Shields stress inversion (Equation 3) and boxes with grey fill indicate estimates derived from the method of Trampush et al. (2014) (Equation 4). BC = Bear Canyon; DH = Dry Hollow; LF = Lake Fork; MC = Mellor Canyon; PC = Price Canyon; SmC = Sixmile Canyon; StC = Straight Canyon.

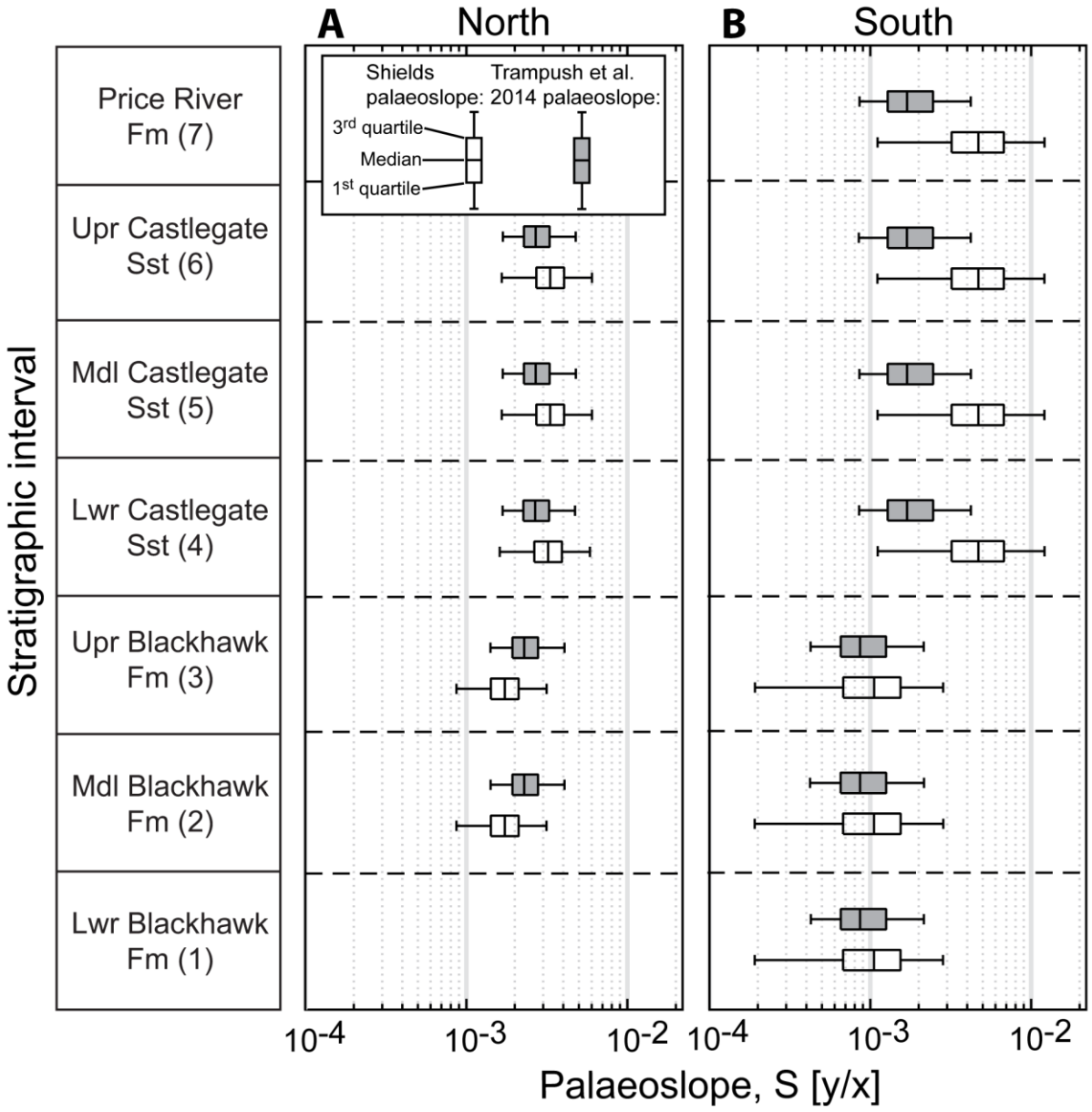

994

995 **Figure 8:** Palaeoslope estimates for the most up-dip location of the defined northern (part A) and
996 southern (part B) depositional-dip transects, for each stratigraphic interval (1–7), where possible,
997 using bulk grain-size data. The central mark of each box indicates the median estimate, and the edges
998 of each box indicate the 1st and 3rd quartiles (or 25th and 75th percentiles) of estimates. The whiskers
999 extend to the most extreme estimates that are not considered to be outliers. Palaeoslope estimates
1000 are derived from 2 independent approaches; boxes with no fill indicate estimates of palaeoslope
1001 derived using a Shields stress inversion (Equation 3) and boxes with grey fill indicate estimates derived
1002 from the method of Trampush et al. (2014) (Equation 4).

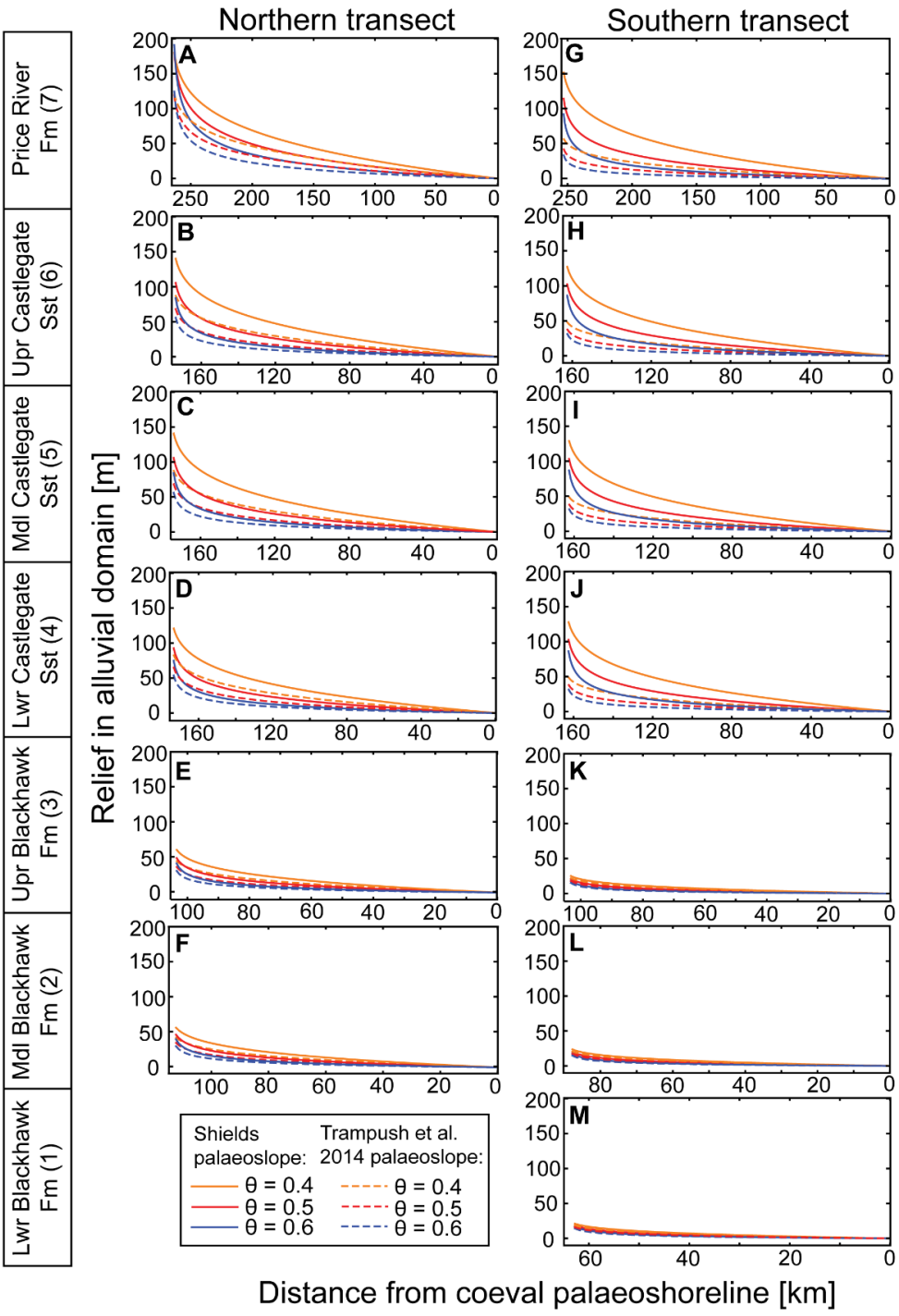

Figure 9: Estimated palaeorelief in the alluvial domain for the defined northern and southern transects, using bulk grain-size data, for each stratigraphic interval (1–7), where possible. Parts A–F depict estimated palaeorelief for the northern transect, from the middle Blackhawk Formation to the Price River Formation. Parts G–M depict estimated palaeorelief for the lower Blackhawk Formation to the Price River Formation. Palaeorelief estimates are derived using palaeoslope estimates from 2 independent approaches; palaeoslopes from a Shields stress inversion (Equation 3) and palaeoslopes from the method of Trampush et al. (2014) (Equation 4). In addition, palaeorelief is estimated using a plausible range of values for the concavity index, θ. Unlike other depositional-dip transects in this study, the x axis instead depicts distance from the coeval palaeoshoreline (following Hettinger and Kirschbaum (2002); Hampson et al. (2012); Hampson et al. (2013)).

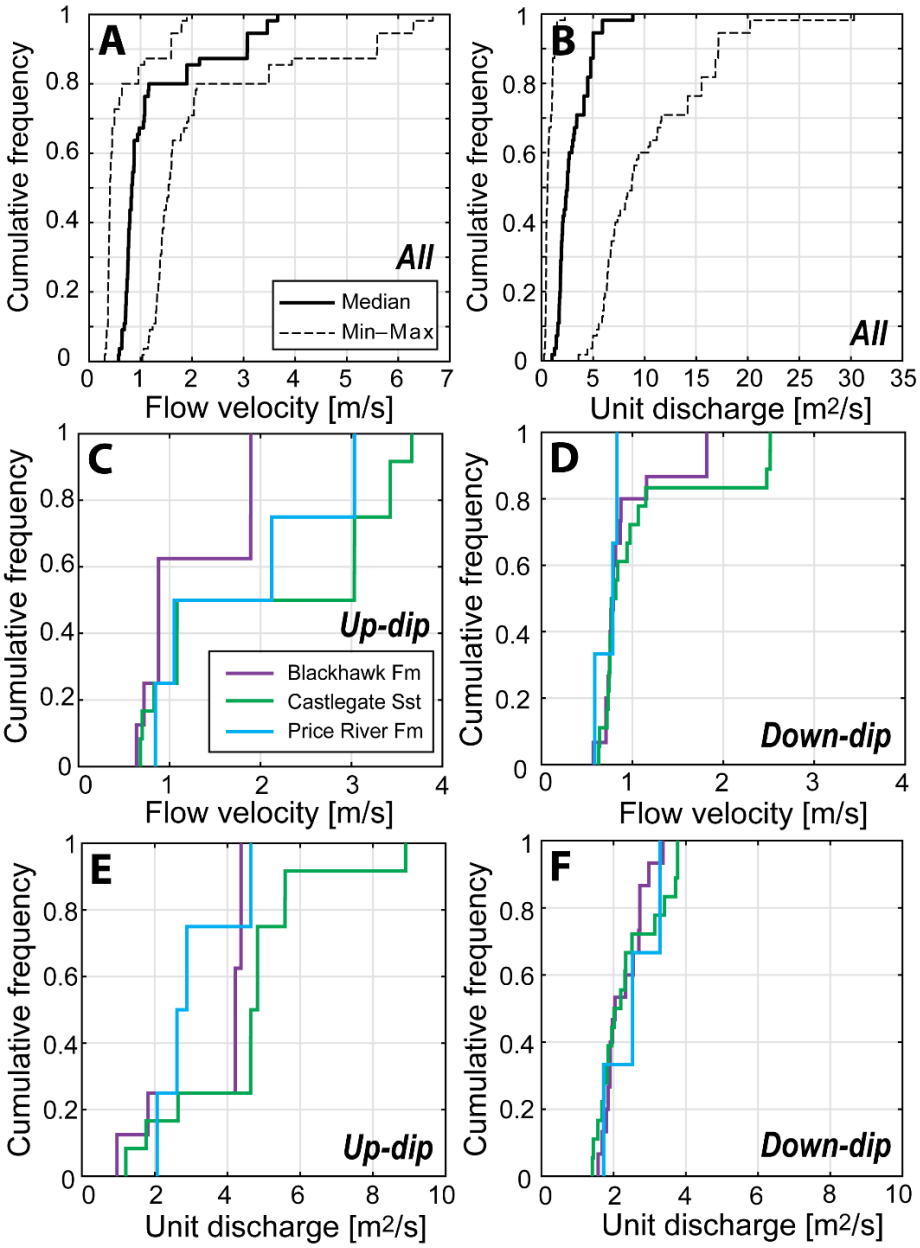

Figure 10: Cumulative frequency distributions of (part A) reconstructed flow velocities across all field areas and (part B) reconstructed water discharges, per unit width, across all field areas. Solid lines indicate median values and dashed lines indicate plausible minimum and maximum values for the median, derived from propagated uncertainty margins. Flow velocities are derived using Manning's formula (Equation 7), as described in the Methods section. Parts C–F depict flow velocities and unit water discharges split into up-dip and down-dip field sites. Down-dip field areas include field areas on the along-strike depositional transect (Price Canyon, Wattis Road, Straight Canyon, Link Canyon and Salina Canyon), meanwhile up-dip field areas include all those that are relatively up-dip (Dry Hollow, Lake Fork, Bear Canyon, Mellor Canyon, Sixmile Canyon). Field areas were also split into the Blackhawk Formation (and up-dip equivalents, i.e. intervals 1–3), Castlegate Sandstone (and up-dip equivalents, i.e. intervals 4–6) and Price River Formation (and up-dip equivalents, i.e. interval 7). Parts C and D depict cumulative frequency distributions of reconstructed flow velocities for up-dip (part C) and down-dip (part D) field areas, respectively. Parts E and F depict cumulative frequency distributions of reconstructed unit water discharges for up-dip (part E) and down-dip (part F) field areas, respectively.

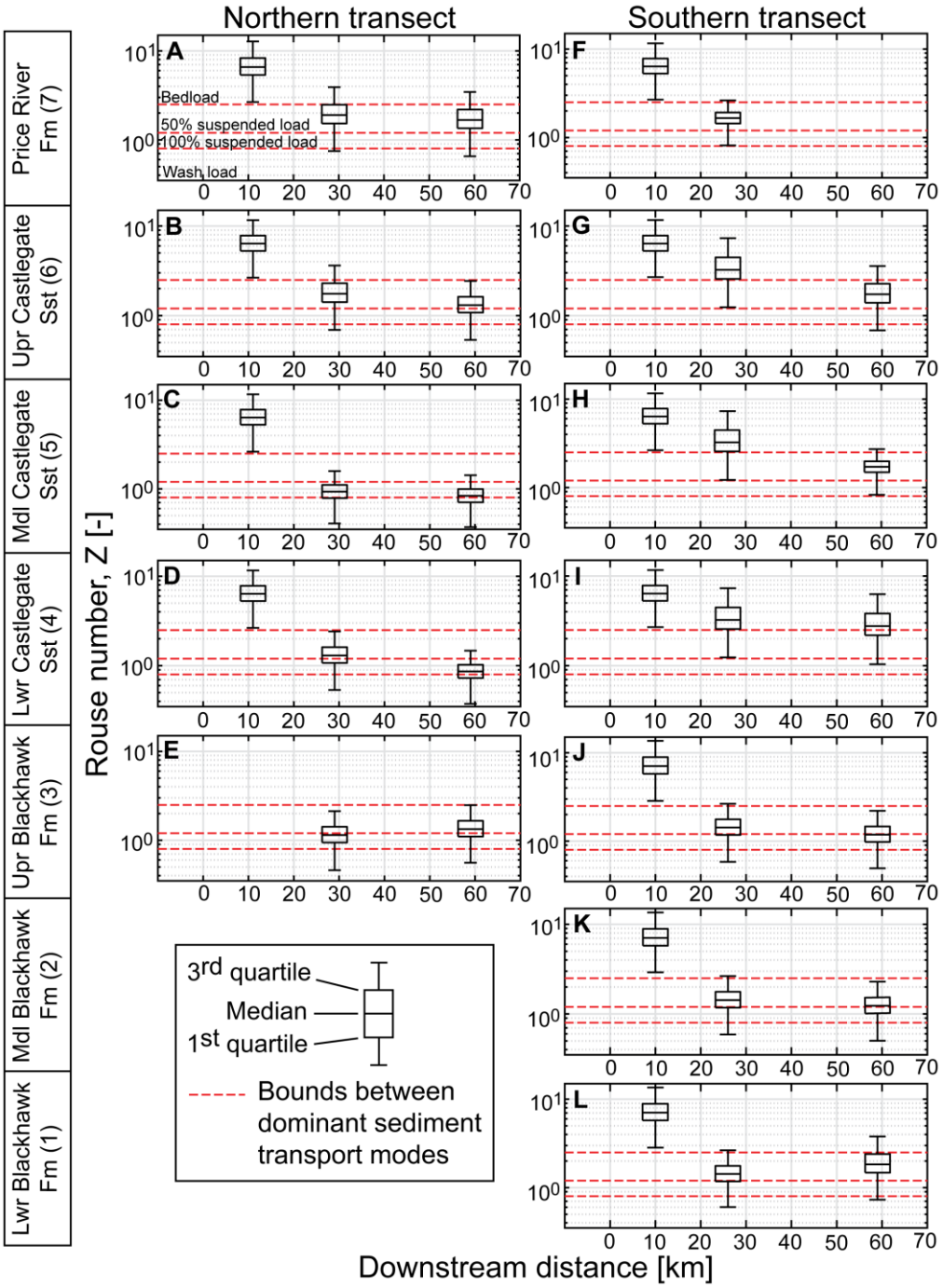

Figure 11: Estimated Rouse numbers, *Z*, for the defined northern and southern transects, using bulk grain-size data, for each stratigraphic interval (1–7), where possible. Dominant mode of sediment transport is typically wash load for $Z < 0.8$, 100% suspended load for $0.8 < Z < 1.2$, 50% suspended load (i.e. mixed load) for $1.2 < Z < 2.5$, and bedload for $Z > 2.5$. Parts A–E represent up-dip to down-dip Rouse numbers for the northern transect, from the upper Blackhawk Formation to the Price River Formation. Parts F–L represent up-dip to down-dip Rouse numbers for the southern transect, from the lower Blackhawk Formation to the Price River Formation. The central mark of each box indicates the median estimate, and the bottom and top edges of each box indicate the 1st and 3rd quartiles (or 25th and 75th percentiles), respectively. The whiskers extend to the most extreme estimates that are not considered to be outliers. Dashed red lines indicate the bounds between differing dominant sediment transport modes, as labelled in part A.

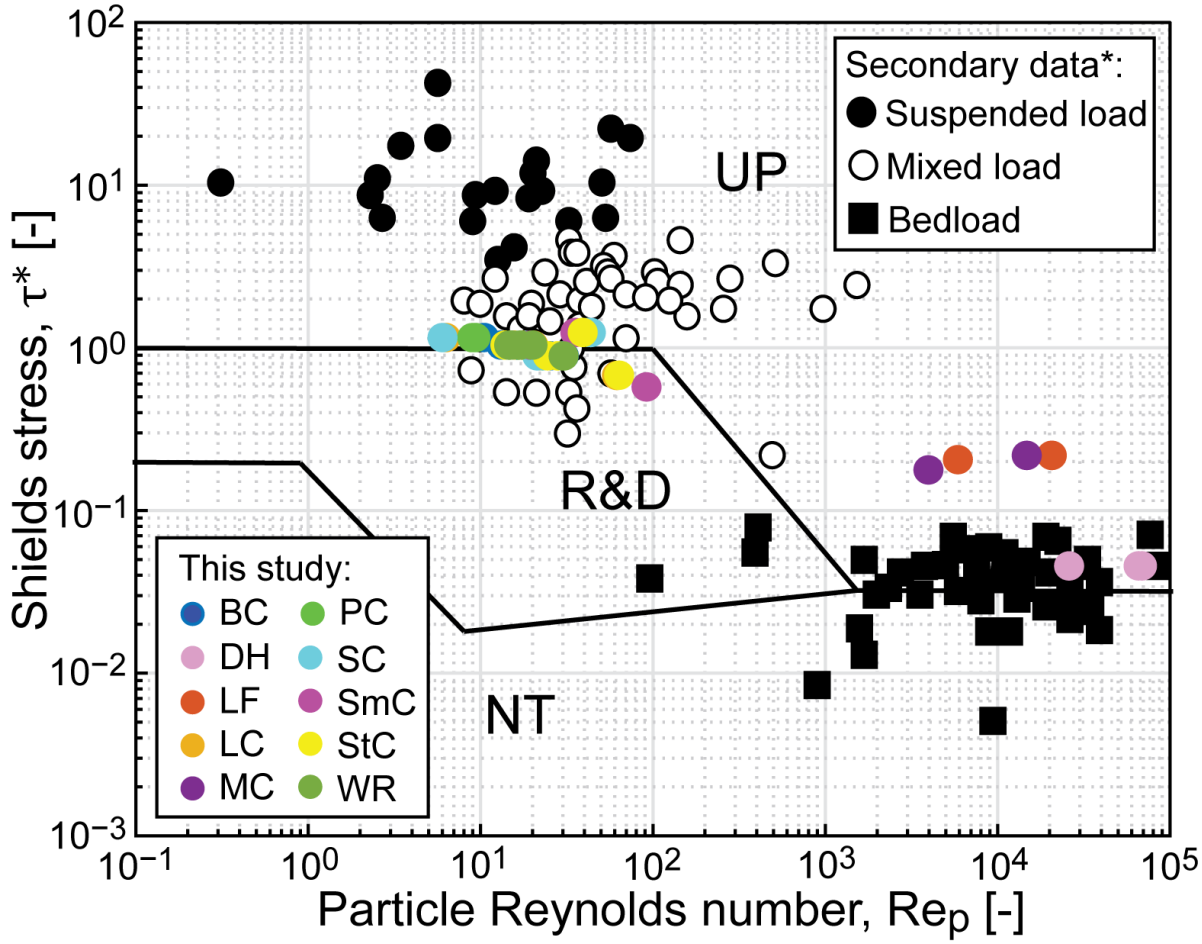

Figure 12: Shields stress, τ^*, plotted as a function of particle Reynold's number, Re_p, for all field sites and for each stratigraphic interval (1–7), where possible, using bulk grain size data. Colour-filled circles indicate field results from this study for Bear Canyon (BC), Dry Hollow (DH), Lake Fork (LF), Link Canyon (LC), Mellor Canyon (MC), Price Canyon (PC), Salina Canyon (SC), Sixmile Canyon (SmC), Straight Canyon (StC) and Wattis Road (WR). *For comparison, this plot includes secondary data, originally compiled by Dade and Friend (1998), from Leopold and Wolman (1957); Schumm (1968); Chitale (1970); Church and Rood (1983); Andrews (1984), for characteristic dominant transport modes. Black squares indicate bedload, white circles indicate mixed load, and black circles indicate suspended load. Solid black lines indicate stability fields of different flow regimes: no sediment transport (NT), ripples and dunes (R&D) and upper-stage plane beds (UP), in line with Allen (1982a, 1982b).

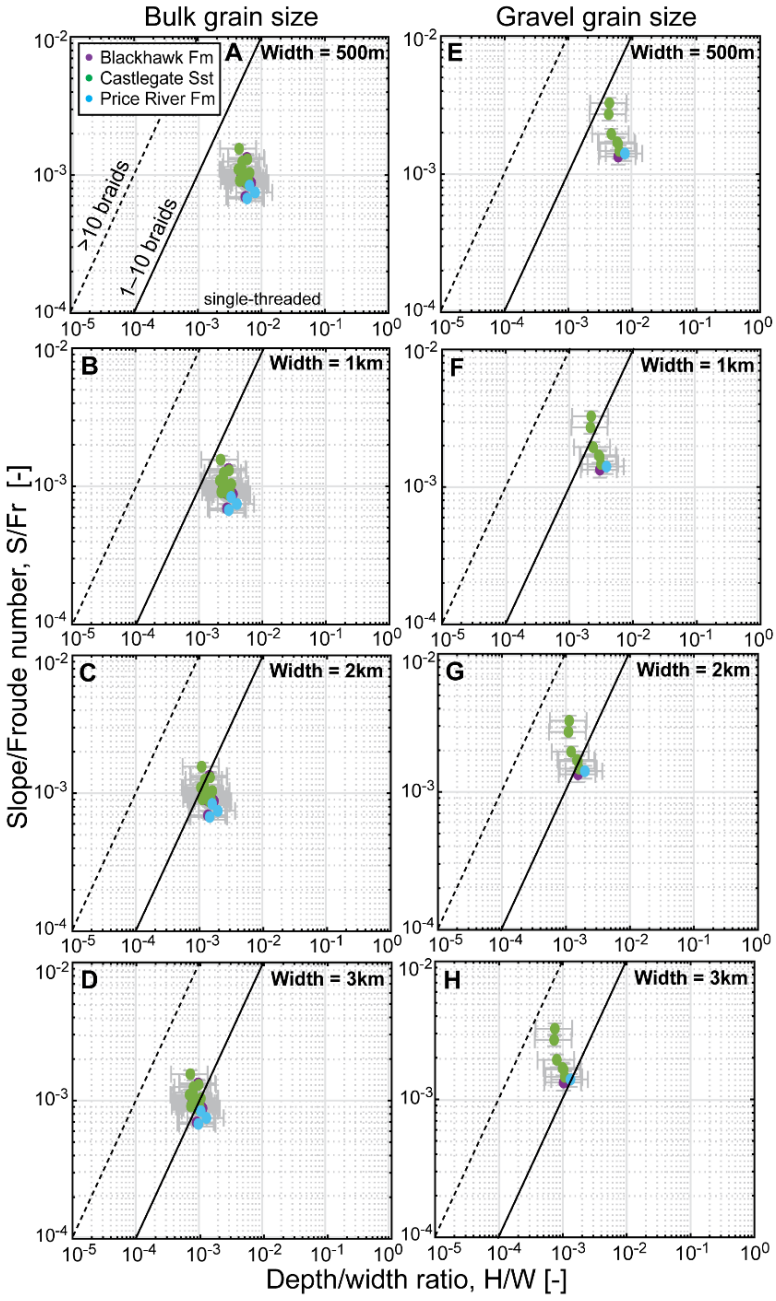

Figure 13: Theoretical stability fields of fluvial planform morphologies, i.e. single-thread and multi-thread planforms, for both bulk grain-sizes (parts A–D) and gravel fraction grain-sizes (parts E–H), where present (not all field localities possessed a gravel fraction). For both bulk and gravel grain-size fractions, a range of river widths are assumed (500 m, 1 km, 2 km and 3 km) and used to calculate the depth/width ratio. Data points are for all localities, in space and time, along the defined along-depositional strike transect, i.e. these data points represent the five parallel fluvial systems and do not consider up-dip localities. Data are further subdivided into the Blackhawk Formation (intervals 1–3), Castlegate Sandstone (intervals 4–6) and Price River Formation (interval 7). Coloured markers indicate the median value and error bars represent plausible minimum and maximum values for the median, derived from propagated uncertainty margins. Solid black lines indicate the bounds of each stability field, and therefore the predicted transition from single-thread (straight/meandering) to multi-thread (anabranching/braided) planform morphology. Dashed black lines indicate a potential transition from 1–10 threads to >10 threads, based on modern data (G. Parker, 1976).

Supplementary Information for: ***Reconstructing the morphologies and hydrodynamics of ancient rivers from source to sink: Cretaceous Western Interior Basin, Utah, USA***

Sinéad J. Lyster[1]*, Alexander C. Whittaker[1], Gary J. Hampson[1], Elizabeth, A. Hajek[2], Peter A. Allison[1] and Bailey A. Lathrop[1]

[1] Department of Earth Science and Engineering, Imperial College London, London, UK.

[2] Department of Geosciences, The Pennsylvania State University, Pennsylvania, USA.

*s.lyster17@imperial.ac.uk

Contents:

S1. Variables list

Here we present a list of all variables assigned and used in this study (see Methods section):

A_x	Upstream catchment area [m^2]
C_1	Constant in Equation 9 associated with grain sphericity and roundness [-]
C_2	Constant in Equation 9 associated with grain sphericity and roundness [-]
c_H	Hack coefficient [-]
D_x	*x*th percentile of the grain size distribution [m]
Fr	Froude number [-]
g	Acceleration due to gravity [m/s^2]
H	Median formative flow depth [m]
h	Hack exponent [m]
h_d	Mean original bedform (i.e. dune) height [m]
h_{xs}	Mean cross-set height [m]
k	Erodibility constant [-]
k_s	Steepness index [$m^{0.8}$ or m^1 or $m^{1.2}$]
L_x	Upstream catchment length [m]
n	Manning's constant [$s/m^{1/3}$]
Q	Water discharge [m^2/s or m^3/s]
R	Dimensionless submerged specific gravity of sediment in water [-]
Re_p	Particle Reynold's number [-]
S	Slope [-]
U	Flow velocity [m/s]

1105	u_*	Bed shear velocity [m/s]
1106	v	Kinematic viscosity of water [m^2/s]
1107	W	Channel width [m]
1108	w_s	Sediment settling velocity [m/s]
1109	Z	Rouse number [-]
1110	α0	Constant in Equation 4 [-]
1111	α1	Constant in Equation 4 [-]
1112	α2	Constant in Equation 4 [-]
1113	β	Eddy viscosity and diffusivity constant [-]
1114	θ	Concavity index [-]
1115	κ	von Karman constant [-]
1116	λ	Bedform wavelength [m]
1117	ρ	Fluid density [kg/m^3]
1118	τ*	Dimensionless bed shear stress, Shields stress [-]
1119	τ_b	Bed shear stress [$kg/m/s^2$]
1120		

1121 **S2. Field localities**

1122 Palaeohydrological data were collected at each field site, as described in the Methods. These data
1123 centred on grain-size and cross-set measurements, but additionally included measurement of channel
1124 geometries and palaeocurrent indicators.

1125 Field localities were grouped spatially, typically by the canyon in which they were located. From north-
1126 northeast to south-southwest, localities were grouped into 5 field areas along a depositional strike
1127 transect: Price Canyon, Wattis Road, Straight Canyon (including Joe's Valley Reservoir), Link Canyon
1128 and Salina Canyon (Fig. S1; reproduced from Fig. 1 in the main text). These 5 field areas represent 5
1129 parallel transverse fluvial systems draining the Sevier orogenic front. Further data were collected
1130 along two up-dip to down-dip depositional-dip transects, to encompass an upstream to downstream
1131 element for 2 of these palaeorivers (Fig. S1). The northern depositional-dip transect included field
1132 localities that were grouped as Dry Hollow, Lake Fork, Bear Canyon, and terminating at Price Canyon.
1133 Meanwhile, the southern depositional-dip transect included field localities that were grouped as
1134 Mellor Canyon, Sixmile Canyon, and terminating at Straight Canyon. These transects are in line with
1135 those implemented in previous work, both along-strike (Hampson et al., 2012; Hampson et al., 2013;
1136 Flood & Hampson, 2014, 2015; Chamberlin & Hajek, 2019) and up-dip to down-dip (Robinson &
1137 Slingerland, 1998; Horton et al., 2004; Aschoff & Steel, 2011b, 2011a).

1138 For each field area, localities were typically within 5 km of one another. There exist a few exceptions
1139 to this, in which localities were slightly more spread out (<10 km). These field areas were characterised
1140 by post-depositional extensional faulting and so we encompassed localities that were either along-
1141 depositional strike, or further down-dip on downthrown fault blocks — when restored, it is
1142 anticipated that these field localities would have been in close proximity. All field localities are detailed
1143 in Table S1 and have been subdivided by both field area and stratigraphic interval. It is important to
1144 note that some field localities are duplicated across stratigraphic intervals — this is where data have
1145 time-averaged across stratigraphic intervals.

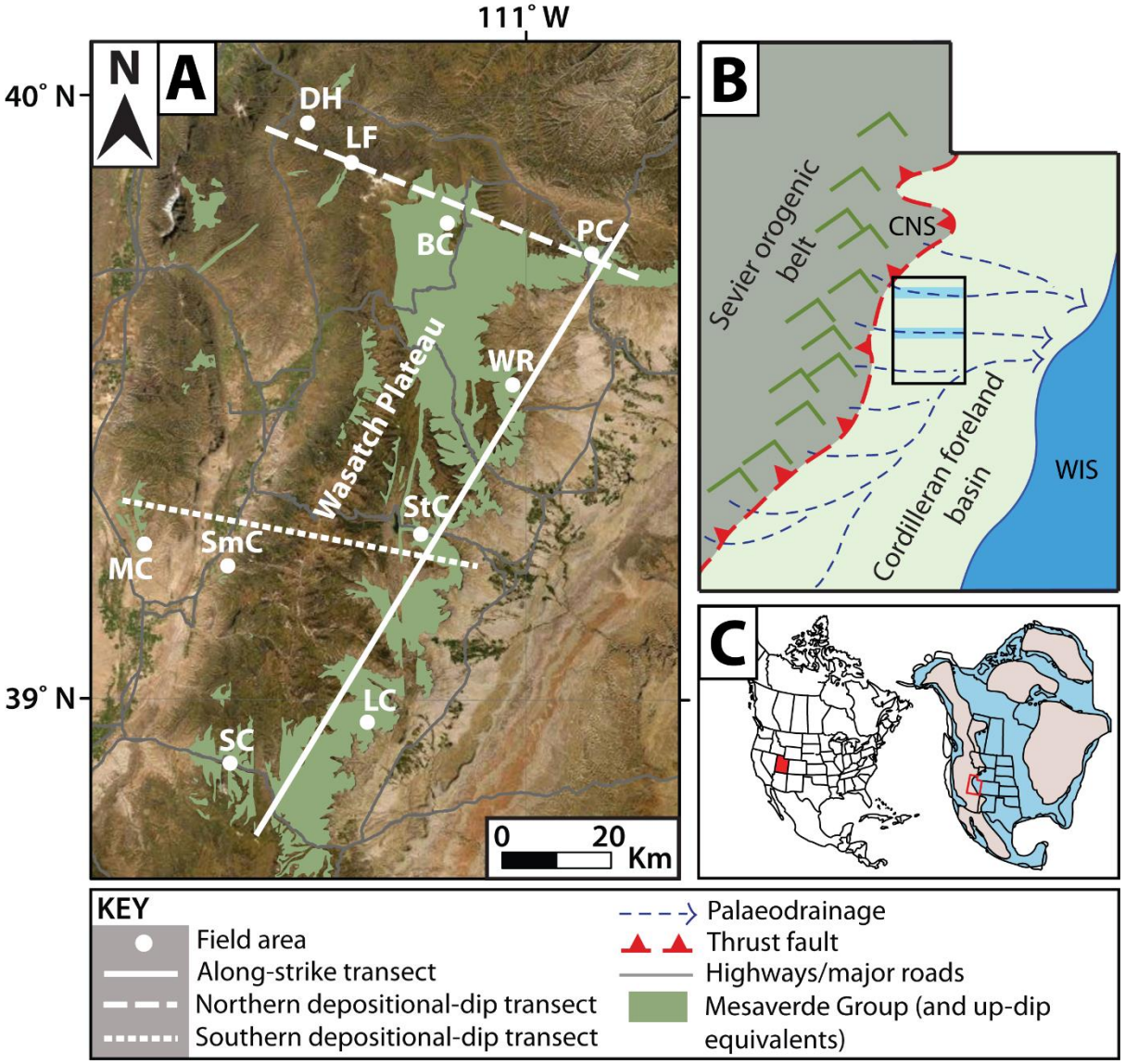

Figure S1: *Study area showing key localities mentioned in the supplement, reproduced from Figure 1 in the main manuscript. Part A) Field areas in central Utah, USA, which include Bear Canyon (BC), Dry Hollow (DH), Lake Fork (LF), Link Canyon (LC), Mellor Canyon (MC), Price Canyon (PC), Salina Canyon (SC), Sixmile Canyon (SmC), Straight Canyon (StC) and Wattis Road (WR). The solid white line indicates the along-depositional-strike transect defined in this study, the dashed white line indicates the northern depositional-dip transect defined in this study, and the dotted white line indicates the southern depositional-dip transect defined in this study. Part B) A conceptual diagram of Utah palaeogeography and palaeodrainage in the Campanian (Late Cretaceous). Likely configurations of drainage toward the Western Interior Seaway (WIS) are indicated by dashed blue lines. CNS = Charleston–Nebo Salient. The black outlined box indicates the study area (i.e. part A), and the two highlighted drainage routes (shaded blue) represent the northern and southern depositional-dip transects defined in this study (see Part A). Part C) The location of Utah relative to the modern North American continent (left) and the Late Cretaceous North American continent (right), which features the Western Interior Seaway (blue). Utah is highlighted as a red box.*

Table S1: *Field localities visited in this study, for each field area (e.g. Price Canyon, Wattis Road, etc). Field localities are further subdivided into their respective stratigraphic intervals (1–7). 1 = lower Blackhawk Formation; 2 = middle Blackhawk Formation; 3 = upper Blackhawk Formation; 4 = lower Castlegate Sandstone; 5 = middle Castlegate Sandstone; 6 = upper Castlegate Sandstone (Bluecastle Tongue); 7 = (lowermost) Price River Formation. It is important to note that some field localities are duplicated across stratigraphic intervals — this is where data have been time-averaged across stratigraphic intervals. Where 'N/A' is reported, this is the absence of data (typically due to lack of access or lack of outcrop).*

Location and stratigraphic interval		Field sites	Elevation, m (±3–4)
Bear Canyon	Lower Blackhawk Formation (1)	N/A	N/A
	Middle Blackhawk Formation (2)	N39 49 53.4, W111 08 32.8	2383
		N39 46 59.3, W111 10 37.8	2325
	Upper Blackhawk Formation (3)	N39 47 31.9, W111 11 33.6	2347
		N39 47 57.4, W111 12 23.0	2373
		N39 48 04.1, W111 12 37.0	2416
		N39 48 00.5, W111 12 31.9	2371
	Lower Castlegate Sandstone (4)	N39 48 05.4, W111 12 27.5	2439
		N39 48 07.6, W111 12 35.6	2426
	Middle Castlegate Sandstone (5)	N39 50 18.2, W111 11 31.8	2263
		N39 50 10.4, W111 11 16.6	2261
	Upper Castlegate Sandstone (6)	N39 50 17.6, W111 11 42.6	2282
		N39 49 52.7, W111 08 30.5	2341
		N39 48 12.7, W111 12 33.3	2495
		N39 48 09.8, W111 12 30.1	2485
	Price River Formation (7)	N39 51 06.7, W111 11 01.7	2200
		N39 50 33.8, W111 11 17.0	2236
		N39 49 53.4, W111 08 32.8	2383
Dry Hollow	Lower Blackhawk Formation (1)	N/A	N/A
	Middle Blackhawk Formation (2)	N39 57 35.2, W111 28 42.6	1769
		N3957 35.2, W111 28 43.5	1773
	Upper Blackhawk Formation (3)	N39 57 35.2, W111 28 42.6	1769
		N3957 35.2, W111 28 43.5	1773
	Lower Castlegate Sandstone (4)	N39 57 34.8, W111 28 40.6	1764
	Middle Castlegate Sandstone (5)	N39 57 33.0, W111 23 38.0	1730
		N39 57 33.8, W111 28 37.8	1756
	Upper Castlegate Sandstone (6)	N39 57 33.0, W111 23 38.0	1730
		N39 57 33.8, W111 28 37.8	1756
	Price River Formation (7)	N/A	N/A
Lake Fork	Lower Blackhawk Formation (1)	N/A	N/A
	Middle Blackhawk Formation (2)	N/A	N/A
	Upper Blackhawk Formation (3)	N/A	N/A
	Lower Castlegate Sandstone (4)	N39 53 16.1, W111 23 49.5	2058

	Middle Castlegate Sandstone (5)	N39 53 36.6, W111 23 27.7	2063
		N39 53 29.7, W111 23 06.8	2115
	Upper Castlegate Sandstone (6)	N39 53 36.6, W111 23 27.7	2063
		N39 53 29.7, W111 23 06.8	2115
	Price River Formation (7)	N39 53 23.0, W111 22 59.1	2131
		N39 53 21.3, W111 22 57.6	2170
Link Canyon	Lower Blackhawk Formation (1)	N38 57 42.1, W111 19 57.4	2363
		N38 57 39.7, W111 19 53.9	2383
		N38 57 41.4, W111 19 53.0	2398
	Middle Blackhawk Formation (2)	N38 57 44.3, W111 19 53.8	2421
		N38 57 48.4, W111 19 53.9	2473
	Upper Blackhawk Formation (3)	N38 57 58.3, W111 19 57.3	2538
		N38 57 52.8, W111 19 55.8	2509
		N38 57 51.4, W111 19 55.0	2500
	Lower Castlegate Sandstone (4)	N38 58 05.9, W111 19 56.6	2572
	Middle Castlegate Sandstone (5)	N38 58 08.0, W111 19 55.8	2584
	Upper Castlegate Sandstone (6)	N38 58 10.6, W111 19 54.2	2600
	Price River Formation (7)	N38 58 15.8, W111 20 15.0	2643
Mellor Canyon	Lower Blackhawk Formation (1)	N39 15 07.5, W111 49 04.0	1751
		N39 15 05.2, W111 49 04.8	1732
		N39 15 03.3, W111 49 06.6	1721
		N39 15 02.3, W111 49 07.3	1715
		N39 15 00.7, W111 49 05.8	1711
		N39 15 00.0, W111 49 09.8	1701
		N39 14 59.6, W111 49 15.3	1717
		N39 14 59.8, W111 49 23.6	1691
		N39 14 58.0, W111 49 25.0	1683
	Middle Blackhawk Formation (2)	N39 15 07.5, W111 49 04.0	1751
		N39 15 05.2, W111 49 04.8	1732
		N39 15 03.3, W111 49 06.6	1721
		N39 15 02.3, W111 49 07.3	1715
		N39 15 00.7, W111 49 05.8	1711
		N39 15 00.0, W111 49 09.8	1701
		N39 14 59.6, W111 49 15.3	1717
		N39 14 59.8, W111 49 23.6	1691
		N39 14 58.0, W111 49 25.0	1683
	Upper Blackhawk Formation (3)	N39 15 07.5, W111 49 04.0	1751
		N39 15 05.2, W111 49 04.8	1732
		N39 15 03.3, W111 49 06.6	1721
		N39 15 02.3, W111 49 07.3	1715
		N39 15 00.7, W111 49 05.8	1711
		N39 15 00.0, W111 49 09.8	1701
		N39 14 59.6, W111 49 15.3	1717
		N39 14 59.8, W111 49 23.6	1691

		N39 14 58.0, W111 49 25.0	1683
	Lower Castlegate Sandstone (4)	N39 15 11.4, W111 49 00.9	1809
		N39 15 09.8, W111 49 01.6	1784
		N39 15 08.8, W111 49 01.9	1770
	Middle Castlegate Sandstone (5)	N39 15 11.4, W111 49 00.9	1809
		N39 15 09.8, W111 49 01.6	1784
		N39 15 08.8, W111 49 01.9	1770
	Upper Castlegate Sandstone (6)	N39 15 11.4, W111 49 00.9	1809
		N39 15 09.8, W111 49 01.6	1784
		N39 15 08.8, W111 49 01.9	1770
	Price River Formation (7)	N39 15 11.4, W111 49 00.9	1809
		N39 15 09.8, W111 49 01.6	1784
		N39 15 08.8, W111 49 01.9	1770
Price Canyon	Lower Blackhawk Formation (1)	N/A	N/A
	Middle Blackhawk Formation (2)	N/A	N/A
	Upper Blackhawk Formation (3)	N39 44 11.0, W110 50 47.7	1932
		N39 44 08.4, W110 50 46.9	1947
	Lower Castlegate Sandstone (4)	N39 45 05.1, W110 53 10.3	1920
		N39 44 48.5, W110 49 58.1	1969
		N39 44 52.6, W110 49 55.4	1983
	Middle Castlegate Sandstone (5)	N39 45 01.3, W110 49 43.5	2000
		N39 45 03.0, W110 49 40.6	1999
	Upper Castlegate Sandstone (6)	N39 45 10.5, W110 49 35.8	2008
		N39 45 12.0, W110 49 34.8	2003
	Price River Formation (7)	N39 46 18.3, W110 48 12.1	2115
		N39 45 58.8, W110 48 30.1	2095
		N39 45 47.1, W110 48 41.6	2044
		N39 45 32.1, W110 49 02.0	2035
Salina Canyon	Lower Blackhawk Formation (1)	N38 54 00.8, W111 39 53.8	1861
	Middle Blackhawk Formation (2)	N38 53 51.5, W111 39 02.3	1885
	Upper Blackhawk Formation (3)	N38 54 29.6, W111 41 46.8	1802
		N38 54 13.8, W111 39 05.9	1926
	Lower Castlegate Sandstone (4)	N38 54 52.9, W111 38 06.5	2036
		N38 54 52.3, W111 38 08.7	2017
	Middle Castlegate Sandstone (5)	N38 54 50.6, W111 38 18.1	2009
		N38 54 52.6, W111 38 20.2	2030
		N38 54 53.7, W111 38 ~20.2	2035
		N38 54 33.0, W111 42 32.7	1779
	Upper Castlegate Sandstone (6)	N38 54 57.1, W111 38 20.3	2076
		N38 54 59.4, W111 38 13.1	2111
	Price River Formation (7)	N38 55 04.1, W111 38 15.7	2152
Sixmile Canyon	Lower Blackhawk Formation (1)	N39 12 43.1, W111 38 55.0	1876
		N39 12 25.4, W111 39 12.5	1860
	Middle Blackhawk Formation (2)	N39 12 43.1, W111 38 55.0	1876

		N39 12 25.4, W111 39 12.5	1860
	Upper Blackhawk Formation (3)	N39 12 43.1, W111 38 55.0	1876
		N39 12 25.4, W111 39 12.5	1860
	Lower Castlegate Sandstone (4)	N39 12 51.6, W111 37 32.9	1967
		N39 12 51.6, W111 37 54.7	1931
		N39 12 44.5, W111 38 10.4	1892
		N39 12 44.9, W111 38 13.8	1923
		N39 12 49.6, W111 37 40.1	1952
	Middle Castlegate Sandstone (5)	N39 12 51.6, W111 37 32.9	1967
		N39 12 51.6, W111 37 54.7	1931
		N39 12 44.5, W111 38 10.4	1892
		N39 12 44.9, W111 38 13.8	1923
		N39 12 49.6, W111 37 40.1	1952
	Upper Castlegate Sandstone (6)	N39 12 51.6, W111 37 32.9	1967
		N39 12 51.6, W111 37 54.7	1931
		N39 12 44.5, W111 38 10.4	1892
		N39 12 44.9, W111 38 13.8	1923
		N39 12 49.6, W111 37 40.1	1952
	Price River Formation (7)	N39 12 46.4, W111 36 57.8	1995
Straight Canyon	Lower Blackhawk Formation (1)	N39 16 56.6, W111 13 58.0	2027
		N39 16 46.2, W111 13 41.9	2010
		N39 16 29.1, W111 13 11.9	1996
	Middle Blackhawk Formation (2)	N39 17 16.2, W111 14 37.5	2047
		N39 17 15.7, W111 14 30.4	2043
		N39 17 05.7, W111 14 10.5	2037
	Upper Blackhawk Formation (3)	N39 17 36.5, W111 16 16.7	2146
		N39 17 19.3, W111 16 00.0	2129
		N39 17 20.9, W111 15 19.8	2102
	Lower Castlegate Sandstone (4)	N39 17 51.9, W111 16 18.0	2161
	Middle Castlegate Sandstone (5)	N39 18 28.6, W111 16 13.2	2181
	Upper Castlegate Sandstone (6)	N39 18 55.2, W111 16 06.2	2238
	Price River Formation (7)	N/A	
Wattis Road	Lower Blackhawk Formation (1)	N39 31 45.5, W111 02 16.0	2577
	Middle Blackhawk Formation (2)	N39 31 11.9, W111 01 56.9	2692
		N39 31 19.8, W111 01 58.4	2655
	Upper Blackhawk Formation (3)	N39 31 20.7, W111 02 37.2	2798
		N39 31 14.3, W111 02 13.8	2765
	Lower Castlegate Sandstone (4)	N39 31 28.6, W111 02 44.9	2844
	Middle Castlegate Sandstone (5)	N39 31 31.7, W 111 02 50.6	2877
		N39 31 30.2, W111 02 46.4	2861
	Upper Castlegate Sandstone (6)	N39 31 33.5, W111 02 53.2	2889
	Price River Formation (7)	N/A	

1170

1171 **S3. Regional correlation**

In addition to grouping field localities in space, localities were also grouped in time. In this study 7 stratigraphic intervals were defined, which were used to reconstruct the palaeohydrological evolution of ancient rivers draining the Sevier orogenic front. These intervals are all Campanian in age, which spanned a duration of 11.5 Myr (83.6±0.2 to 72.1±0.2 Ma) in the Late Cretaceous. These 7 intervals are defined as: 1 = lower Blackhawk Formation; 2 = middle Blackhawk Formation; 3 = upper Blackhawk Formation; 4 = lower Castlegate Sandstone; 5 = middle Castlegate Sandstone; 6 = upper Castlegate Sandstone (Bluecastle Tongue); 7 = (lowermost) Price River Formation. These intervals are referred to in the Results and in Fig. 2 of the main text. It is important to note that these stratigraphic intervals are not of equal duration — age constraints across these intervals are derived from correlation with ammonite biozones in the down-dip Mancos Shale, which have been age-constrained by radiometric dating of volcanic ash beds (Gill & Hail Jr, 1975; Fouch et al., 1983; Cobban et al., 2006) — see recent review by Seymour and Fielding (2013). The lowermost Blackhawk Formation is correlated with the *Scaphites hippocrepis II* zone (83.5±0.7–81.86±0.36 Ma), the middle Blackhawk Formation with the *Baculites obtusus* zone (80.58±0.55 Ma), and the top of the Blackhawk Formation with the *Baculites asperiformis* zone (79 Ma). The lower and middle Castlegate Sandstone are correlated with the *Baculites perplexus*, *Baculites scotti* (75.84±0.26/75.56±0.11 Ma), *Didymoceras nebrascense* and *Didymoceras stevensoni* (75.19±0.28 Ma) zones. The upper Castlegate Sandstone is correlated with the *Exiteloceras jenneyi* zone (75.08±0.11 Ma) and, finally, the Price River Formation is correlated with the *Didymoceras cheyennense* and *Baculites jenseni* zones (74.67±0.15–71.98±0.31 Ma) (Fouch et al., 1983; Cobban et al., 2006).

Down-dip: Eastern Wasatch Plateau

Along the eastern front of the Wasatch Plateau (Fig. S1), it is straightforward to assign field localities to their appropriate stratigraphic intervals by facies associations, following extensive work that has been undertaken in this region (Lawton, 1983, 1986b; Miall, 1994; van Wagoner, 1995; Yoshida et al., 1996; Miall & Arush, 2001; Lawton et al., 2003; Adams & Bhattacharya, 2005; Hampson et al., 2012; Hampson et al., 2013; Flood & Hampson, 2014; Hampson et al., 2014; Flood & Hampson, 2015).

The lower–middle Campanian Blackhawk Formation, (Hampson, 2010; Hampson et al., 2012) represents deposition on coastal plains behind wave-dominated deltaic shorelines which, up-section, pass landward into alluvial and fluvial plains (Hampson et al., 2012; Hampson et al., 2013). The size and abundance of channelized fluvial sandstone bodies (deposited by both single- and multi-thread rivers) increase from base to top of the Blackhawk Formation (Adams & Bhattacharya, 2005; Hampson et al., 2012; Hampson et al., 2013; Flood & Hampson, 2015). The Blackhawk Formation comprises intervals 1, 2 and 3 in this study, i.e. the lower, middle and upper Blackhawk Formation. The Blackhawk Formation is slightly challenging to subdivide into stratigraphic intervals as it is typically undifferentiated along the eastern Wasatch Plateau front (with the exception of Price Canyon) (Hampson et al., 2012; Hampson et al., 2013) — this is, in part, because the upper half of the Blackhawk Formation lacks mappable coal zones or other stratigraphic markers along the Wasatch Plateau front (Hampson et al., 2012; Hampson et al., 2013). This study follows Flood and Hampson (2014, 2015) in subdividing the Blackhawk Formation into the lower, middle, and upper Blackhawk Formation. While these divisions may not be exact, given variation in outcrop exposure at Price Canyon, Wattis Road, Straight Canyon, Link Canyon and Salina Canyon, as well as north–south variation in stratigraphic thickness, they are appropriate for the temporal and spatial scales considered here. At Price Canyon, only the Desert Member of the Blackhawk Formation is fluvial, and

so data were only collected from this member, which were then assigned to the upper Blackhawk Formation stratigraphic interval. For Wattis Road, Straight Canyon, Link Canyon, and Salina Canyon, field localities were assigned to the lower, middle and upper Blackhawk Formation, following Hampson et al. (2012); Hampson et al. (2013); Flood and Hampson (2014, 2015), based on (1) adjacency to the contact with the overlying Castlegate Sandstone or underlying Star Point Sandstone; (2) where the outcrop was positioned, stratigraphically, within the entire stratigraphic thickness of the Blackhawk Formation at the field area in question; (3) architectural and facies observations — up-section the Blackhawk Formation is more palaeo-landward and preserves an increase in the size and abundance of channelized fluvial sandstone bodies; (4) presence and abundance of coal zones, which are associated with the lower and middle Blackhawk Formation, but are most abundant in the lower Blackhawk Formation (Flood & Hampson, 2014, 2015).

The middle–upper Campanian Castlegate Sandstone is situated atop the Blackhawk Formation and is an extensive and easily recognisable cliff-forming deposit — the basal contact separates braided fluvial deposits from underlying coastal plain deposits of the Blackhawk Formation (van Wagoner, 1995; Yoshida et al., 1996). In this study the Castlegate Sandstone comprises intervals 4, 5 and 6, i.e. the lower, middle and upper Castlegate Sandstone respectively. The lower and upper Castlegate Sandstone both comprise amalgamated braided fluvial channel-belt deposits, whereas the middle Castlegate Sandstone comprises less amalgamated, more meandering, fluvial channel-belt deposits with interbedded mudstones (Fouch et al., 1983; Lawton, 1986b; Miall, 1994; Yoshida et al., 1996; Miall & Arush, 2001).

The ledge-forming upper Campanian Price River Formation conformably overlies the Castlegate Sandstone and is interval 7 in this study. It is recognised by transition from amalgamated fluvial channel-belt deposits of the upper Castlegate Sandstone to large channelized sandstone bodies (~10–30m thick) with interbedded siltstones and mudstones — channelized sandstone bodies form ~75% of the formation (Lawton, 1983, 1986b). This transition is also recognised by a break in slope. Data were collected for channelized sandstone bodies of the lowermost Price River Formation (where accessible) atop the contact with the underlying upper Castlegate Sandstone.

Up-dip: Western Wasatch Plateau

Importantly, in this study data were additionally collected along two up-dip to down-dip transects, to capture upstream to downstream trends for 2 of the 5 transverse fluvial systems. This requires correlation of the 7 aforementioned stratigraphic intervals (along the eastern Wasatch Plateau front) with up-dip strata on the western and central Wasatch Plateau. Up-dip field sites along the northern depositional dip transect include Dry Hollow, Lake Fork, and Bear Canyon, meanwhile up-dip field sites along the southern depositional-dip transect include Mellor Canyon and Sixmile Canyon. These depositional-dip transects follow those of Robinson and Slingerland (1998); Horton et al. (2004). Bear Canyon can be excluded from subsequent considerations as it has been mapped using Blackhawk–Castlegate–Price River nomenclature.

Up-dip, on the western Wasatch Plateau, correlative strata include more proximal sediments of the Indianola Group and Price River Formation, which is now known to not be time-equivalent with the down-dip Price River Formation exposed near Price, Utah (Robinson & Slingerland, 1998; Horton et al., 2004; Aschoff & Steel, 2011b, 2011a). Here, to avoid confusion, up-dip strata are referred to as the Price River Conglomerate, following Aschoff and Steel (2011b, 2011a). It should be noted that the

Price River Conglomerate has elsewhere been referred to as the Conglomerate of Thistle (Valora, 2010). The detail of up-dip correlations is limited by poor exposure on the Wasatch Plateau and difficulty in dating conglomerates. Nevertheless, work by Robinson and Slingerland (1998) successfully used palynology to establish correlation of the lower Castlegate Sandstone with up-dip conglomerates exposed across a variety of localities on the Wasatch Plateau (Fig. 2). Correlations were corroborated by field observations, e.g. correlation of a white, quartzite-dominated, cobble–boulder conglomerate in the Charleston–Nebo Salient of the Sevier thrust belt with the Castlegate–Price River succession in the Book Cliffs to the east, which can be traced in seismic reflection data (Robinson & Slingerland, 1998; Horton et al., 2004). These works were used in the field to establish correlations.

The up-dip upper Sixmile Canyon Formation of the Indianola Group is predominantly characterised by synorogenic gravel–sand fluvial facies, spanning polymictic fluvial conglomerates to medium–coarse-grained sandstones (Lawton, 1982, 1986a, 1986b). The upper Sixmile Canyon Formation is time-correlative with the Blackhawk Formation (Lawton, 1982; Fouch et al., 1983; Lawton, 1986b), and therefore encompasses intervals 1, 2, and 3 in this study. Meanwhile, the up-dip Price River Conglomerate is characterised by quartzite-dominated synorogenic fanglomerates wherein debris flow facies interact with gravel–sand fluvial facies (Robinson & Slingerland, 1998; Aschoff & Steel, 2011b, 2011a). The Price River Conglomerate is time-correlative with the down-dip lower, middle, and upper Castlegate Sandstone, and Price River Formation (Robinson & Slingerland, 1998; Horton et al., 2004), and therefore encompasses intervals 4, 5, 6 and 7 in this study.

Given uncertainties in age constraints, a conservative approach to correlation is taken in this study. Up-dip, at Dry Hollow, Lake Fork, Mellor Canyon, and Sixmile Canyon, the upper Sixmile Canyon Formation of the Indianola Group (intervals 1–3) is time-averaged, and the entire Price River Conglomerate (intervals 4–7) is also time-averaged. It can be said that, up-dip, time-averaging across intervals 1–3 and 4–7, respectively, may lead to loss of temporal signal. However, exceptions were made to time-averaging where field localities were known to be situated at the top of the upper Sixmile Canyon Formation or at the top/base of the Price River Conglomerate. Currently, it is not possible to generate time-correlations at higher resolution. Nevertheless, the observation was made that within the upper Sixmile Canyon Formation and Price River Conglomerate, respectively, median grain-sizes and mean cross-set heights for each grain-size facies were generally similar throughout sections. The main impact of time-averaging across sections was therefore that our results do not account for how the proportions of different grain-size facies change up-section.

In the northern transect, for up-dip field areas of Dry Hollow and Lake Fork, assignment of field localities to their appropriate stratigraphic intervals (as per the previous paragraph) is simple as regional mapping has differentiated the Indianola Group into its respective members, including the Sixmile Canyon Formation, and has also mapped the Price River Conglomerate (though it is mapped with its alternative name, i.e. Conglomerate of Thistle). However, in the southern transect, for up-dip field areas of Mellor Canyon and Sixmile Canyon, assignment is less simple as regional mapping is older and predates recent advances in regional correlation (c.f. Robinson & Slingerland, 1998; Horton et al., 2004; Aschoff & Steel, 2011b, 2011a). In Sixmile Canyon, the Indianola Group is differentiated into its respective members. However, what would be Price River Conglomerate has here been mapped as the Price River Formation — but it is now known that the up-dip Price River Formation on the western Wasatch Plateau is time-correlative with *both* the Castlegate Sandstone and Price River Formation on the eastern Wasatch Plateau (Robinson & Slingerland, 1998; Horton et al., 2004; Aschoff & Steel,

2011b, 2011a). This is taken into account accordingly and considered to be Price River Conglomerate. Secondly, in Mellor Canyon, the entire stratigraphy is undifferentiated — it is all mapped as undifferentiated Indianola Group sediments, and is capped unconformably by the North Horn Formation. As such, in this study the stratigraphy in Mellor Canyon was newly logged so that stratigraphy could be appropriately assigned, (expanding on work by Robinson and Slingerland (1998)) (Fig. S2). Observations of up-dip, more proximal sediments in the northern depositional-dip transect (i.e. at Dry Hollow) were extrapolated to Mellor Canyon. These included observations that the Price River Conglomerate is characterised by quartzite-dominated synorogenic fanglomerates wherein debris flow facies interact with gravel–sand fluvial facies (Robinson & Slingerland, 1998; Aschoff & Steel, 2011b, 2011a), and the upper Sixmile Canyon Formation of the Indianola Group is predominantly characterised by synorogenic gravel–sand fluvial facies spanning polymictic conglomerates to medium–coarse-grained sands (Lawton, 1982, 1986a, 1986b). In logging the Mellor Canyon section, quartzite-dominated debris fanglomerates with interspersed gravel–sand channelized bodies were successfully identified, and then classified as Price River Conglomerate (Fig. S2). In addition, the more polymictic fluvial conglomerates and channelized sandstone bodies, which can be likened to the upper Sixmile Canyon Formation, were also successfully identified (Fig. S2). It is unclear whether logged strata encompass the entire Sixmile Canyon Formation, or just the uppermost Sixmile Canyon Formation. However the entire Sixmile Canyon Formation at Sixmile Canyon has a stratigraphic thickness of over 1.2 km, whereas at Mellor Canyon our logging is for the uppermost 240 m of Sixmile Canyon Formation —it is therefore reasonable to assign these sediments to the upper Sixmile Canyon Formation (Fig. S2).

[SUPPLEMENTARY FIGURE 2 ATTACHED AS PDF "LYSTER_ETAL_SUPPINFO_FIG2.PDF"]

Figure S2: *Measured section through the Sixmile Canyon Formation (Indianola Group) and (extrapolated) Price River Conglomerate at Mellor Canyon.*

S4 Field data

Palaeohydrologic field data collection was primarily focused on grain-size and cross-set measurements but, as mentioned, additionally included measurement of channel geometries and palaeocurrent indicators. In this section raw field data are presented for grain-size measurements (Table S2) and cross-set measurements (Table S3), as these are the data that we propagate through our quantitative palaeohydrologic framework to reconstruct various palaeohydrologic parameters (see Methods). Data are tabulated and subdivided by field area and stratigraphic interval. First, extended information pertaining to grain-size data collection is presented.

Grain-Size

At each field site, the coarse-fraction (>2 mm in diameter) and sand-fraction (<2 mm in diameter) grain-size of channel-fill deposits was established (Fig. 3a,b in main text). For coarse-fractions (>2 mm), grain-size distributions were measured via Wolman point counts (Wolman, 1954). For each count, 100 clasts were randomly selected across a 1 m^2 area of exposed outcrop (or 2 m^2, where grain-size was boulder-grade) and the long axis was measured (Fig. 3a). The long axis was measured as opposed to the intermediate axis because: (1) it is objectively easier, and more efficient, to identify and

consistently measure the long axis (Brooke et al., 2018; Watkins et al., 2020); (2) the ratio between the long and intermediate axis is broadly constant in fluvial gravels, near 0.7 (e.g. Litty & Schlunegger, 2017; Litty et al., 2017); (3) any measured axis is an apparent axis given the arbitrary orientation of the outcrop exposure, so it is therefore consistent and easiest to measure the longest observed. For sand-fractions (<2 mm), scaled photographs were instead processed in *ImageJ* software and the long axis of 50 randomly selected grains were similarly measured (Fig. 3b) (where sand-fractions were poorly sorted 100 clasts were counted for certainty). Grain-size distributions were then used to establish the median grain size, D_{50}, and 84th percentile, D_{84}. Finally, where grain-size facies in channel-fill deposits were disparate, e.g. gravel topped with sand, data were collected for each grain-size facies and the proportions of each facies were estimated (Fig. 3c).

To recover spatio-temporal grain-size distribution trends along several time-averaged stratigraphic intervals, it was crucial that representative time-averaged data were collected. Not only were grain-size data collected for each grain-size facies (Fig. 3a–c), depending on overall outcrop extent Wolman point counts were also repeated and/or additional scaled photographs were taken for *ImageJ* processing at intermittent stratigraphic intervals (e.g. one count per 5–10 m of strata or per channelized body). The extent of each field site can be approximated as the extent of outcrop apparent in Fig. 3c–h. From these data an average sand-fraction grain size and an average gravel-fraction grain size was produced for each field site. As each space–time interval includes multiple field sites, this results in multiple average sand- and gravel-fraction grain-sizes per interval, encompassing channel-fill deposits from several channelized bodies. Finally, weighted, bulk-grain size distribution was produced for each space–time interval using the gravel- vs sand-fraction weightings at each field site — each field site within a space–time interval was assigned equal weighting. For example, say data were collected from two field sites for one space–time interval. If one of these sites was 100% sand-grade, and the second site was 80% sand-grade and 20% gravel-grade, then the bulk grain-size for that space–time interval would be calculated as follows: 50% would be the average sand-fraction grain size at Site 1, 40% would be the average sand-fraction grain-size at Site 2, and 10% would be the average gravel-fraction grain-size at Site 2.

Table S2: *Grain-size data collected and used in this study. Bulk grain-sizes include both the sand fraction grain-size and the gravel fraction grain-size, which are weighted according to their respective facies proportions. Gravel fraction grain-sizes solely represent the gravel fraction. Where 'N/A' is reported, this is the absence of data (due to lack of access) or, in the case of gravel fraction grain-sizes, absence of a gravel fraction in the exposed outcrop. D_{50} and D_{84} represent the median and 84th percentile of grain-size, respectively. Grain-size data are reported for each field location, through stratigraphic intervals 1–7: 1 = lower Blackhawk Formation; 2 = middle Blackhawk Formation; 3 = upper Blackhawk Formation; 4 = lower Castlegate Sandstone; 5 = middle Castlegate Sandstone; 6 = upper Castlegate Sandstone (Bluecastle Tongue); 7 = (lowermost) Price River Formation.*

Location and stratigraphic interval		**Bulk grain-size**		**Gravel fraction grain-size**	
		D_{50} (mm)	D_{84} (mm)	D_{50} (mm)	D_{84} (mm)
Bear Canyon	Lower Blackhawk Formation (1)	N/A	N/A	N/A	N/A
	Middle Blackhawk Formation (2)	0.24	0.38	N/A	N/A

	Upper Blackhawk Formation (3)	0.22	0.30	N/A	N/A
	Lower Castlegate Sandstone (4)	0.26	0.36	N/A	N/A
	Middle Castlegate Sandstone (5)	0.19	0.26	74.92	166.21
	Upper Castlegate Sandstone (6)	0.34	5.00	10.00	15.00
	Price River Formation (7)	0.39	3.00	10.00	20.00
Dry Hollow	Lower Blackhawk Formation (1)	N/A	N/A	N/A	N/A
	Middle Blackhawk Formation (2)	35.00	65.00	35.00	65.00
	Upper Blackhawk Formation (3)	35.00	65.00	35.00	65.00
	Lower Castlegate Sandstone (4)	65.00	126.5	65.00	126.5
	Middle Castlegate Sandstone (5)	67.00	147.5	80.00	179.00
	Upper Castlegate Sandstone (6)	67.00	147.5	80.00	179.00
	Price River Formation (7)	N/A	N/A	N/A	N/A
Lake Fork	Lower Blackhawk Formation (1)	N/A	N/A	N/A	N/A
	Middle Blackhawk Formation (2)	N/A	N/A	N/A	N/A
	Upper Blackhawk Formation (3)	N/A	N/A	N/A	N/A
	Lower Castlegate Sandstone (4)	30.00	50.00	30.00	50.00
	Middle Castlegate Sandstone (5)	30.00	60.00	30.00	63.00
	Upper Castlegate Sandstone (6)	30.00	60.00	30.00	63.00
	Price River Formation (7)	13.00	46.50	32.00	60.00
Link Canyon	Lower Blackhawk Formation (1)	0.31	0.43	N/A	N/A
	Middle Blackhawk Formation (2)	0.30	0.56	N/A	N/A
	Upper Blackhawk Formation (3)	0.27	0.40	N/A	N/A
	Lower Castlegate Sandstone (4)	0.62	1.55	5.00	9.00
	Middle Castlegate Sandstone (5)	0.27	0.42	N/A	N/A
	Upper Castlegate Sandstone (6)	0.25	0.31	N/A	N/A
	Price River Formation (7)	0.14	0.18	N/A	N/A
Mellor Canyon	Lower Blackhawk Formation (1)	10.00	30.00	20.00	36.00
	Middle Blackhawk Formation (2)	10.00	30.00	20.00	36.00
	Upper Blackhawk Formation (3)	10.00	30.00	20.00	36.00
	Lower Castlegate Sandstone (4)	24.00	52.00	34.00	65.00
	Middle Castlegate Sandstone (5)	24.00	52.00	34.00	65.00
	Upper Castlegate Sandstone (6)	24.00	52.00	34.00	65.00
	Price River Formation (7)	24.00	52.00	34.00	65.00
Price Canyon	Lower Blackhawk Formation (1)	N/A	N/A	N/A	N/A
	Middle Blackhawk Formation (2)	N/A	N/A	N/A	N/A
	Upper Blackhawk Formation (3)	0.27	0.40	N/A	N/A
	Lower Castlegate Sandstone (4)	0.18	0.25	13.00	30.00
	Middle Castlegate Sandstone (5)	0.17	0.21	N/A	N/A
	Upper Castlegate Sandstone (6)	0.26	0.39	N/A	N/A
	Price River Formation (7)	0.32	0.72	6.00	11.00
Salina Canyon	Lower Blackhawk Formation (1)	0.13	0.17	N/A	N/A
	Middle Blackhawk Formation (2)	0.49	0.67	N/A	N/A
	Upper Blackhawk Formation (3)	0.39	0.58	3.94	7.00

	Lower Castlegate Sandstone (4)	0.48	1.03	6.00	10.00
	Middle Castlegate Sandstone (5)	0.28	0.71	6.00	14.00
	Upper Castlegate Sandstone (6)	0.32	0.41	N/A	N/A
	Price River Formation (7)	0.31	0.38	N/A	N/A
Sixmile Canyon	Lower Blackhawk Formation (1)	0.29	0.68	22.00	40.00
	Middle Blackhawk Formation (2)	0.29	0.68	22.00	40.00
	Upper Blackhawk Formation (3)	0.29	0.68	22.00	40.00
	Lower Castlegate Sandstone (4)	0.81	15.00	18.00	35.00
	Middle Castlegate Sandstone (5)	0.81	15.00	18.00	35.00
	Upper Castlegate Sandstone (6)	0.81	15.00	18.00	35.00
	Price River Formation (7)	0.43	5.00	8.00	15.00
Straight Canyon	Lower Blackhawk Formation (1)	0.37	0.48	N/A	N/A
	Middle Blackhawk Formation (2)	0.24	0.32	N/A	N/A
	Upper Blackhawk Formation (3)	0.23	0.32	N/A	N/A
	Lower Castlegate Sandstone (4)	0.64	0.97	N/A	N/A
	Middle Castlegate Sandstone (5)	0.46	11.00	10.00	23.00
	Upper Castlegate Sandstone (6)	0.34	0.52	6.00	10.00
	Price River Formation (7)	N/A	N/A	N/A	N/A
Wattis Road	Lower Blackhawk Formation (1)	0.24	0.28	N/A	N/A
	Middle Blackhawk Formation (2)	0.26	0.30	N/A	N/A
	Upper Blackhawk Formation (3)	0.29	0.36	N/A	N/A
	Lower Castlegate Sandstone (4)	0.39	0.49	N/A	N/A
	Middle Castlegate Sandstone (5)	0.26	0.35	N/A	N/A
	Upper Castlegate Sandstone (6)	0.24	0.30	N/A	N/A
	Price River Formation (7)	N/A	N/A	N/A	N/A

Table S3: *Cross-set data collected and used in this study. Mean cross-set heights are estimated from mean maximum cross-set heights (see Methods). Where 'N/A' is reported, this is the absence of data (due to lack of access) or, rarely, absence of cross-sets. Cross-set data are reported for each field location, through stratigraphic intervals 1–7: 1 = lower Blackhawk Formation; 2 = middle Blackhawk Formation; 3 = upper Blackhawk Formation; 4 = lower Castlegate Sandstone; 5 = middle Castlegate Sandstone; 6 = upper Castlegate Sandstone (Bluecastle Tongue); 7 = (lowermost) Price River Formation.*

Location and stratigraphic interval		**Mean maximum cross-set height (m)**	**Predicted mean cross-set height (m)**	**Standard error on predicted mean cross-set height (m)**	**Number of cross-sets measured**
Bear Canyon	Lower Blackhawk Formation (1)	N/A	N/A	N/A	N/A
	Middle Blackhawk Formation (2)	0.19	0.13	0.0039	123
	Upper Blackhawk Formation (3)	0.11	0.08	0.0012	117

	Lower Castlegate Sandstone (4)	0.13	0.09	0.0026	47
	Middle Castlegate Sandstone (5)	0.19	0.13	0.0091	28
	Upper Castlegate Sandstone (6)	0.23	0.16	0.0046	244
	Price River Formation (7)	0.18	0.13	0.0041	105
Dry Hollow	Lower Blackhawk Formation (1)	N/A	N/A	N/A	N/A
	Middle Blackhawk Formation (2)	N/A	N/A	N/A	N/A
	Upper Blackhawk Formation (3)	N/A	N/A	N/A	N/A
	Lower Castlegate Sandstone (4)	N/A	N/A	N/A	N/A
	Middle Castlegate Sandstone (5)	N/A	N/A	N/A	N/A
	Upper Castlegate Sandstone (6)	N/A	N/A	N/A	N/A
	Price River Formation (7)	N/A	N/A	N/A	N/A
Lake Fork	Lower Blackhawk Formation (1)	N/A	N/A	N/A	N/A
	Middle Blackhawk Formation (2)	N/A	N/A	N/A	N/A
	Upper Blackhawk Formation (3)	N/A	N/A	N/A	N/A
	Lower Castlegate Sandstone (4)	0.18	0.13	0.0250	2
	Middle Castlegate Sandstone (5)	0.12	0.08	0.0090	13
	Upper Castlegate Sandstone (6)	0.12	0.08	0.0090	13
	Price River Formation (7)	0.10	0.07	0.0089	8
Link Canyon	Lower Blackhawk Formation (1)	0.19	0.13	0.0046	94
	Middle Blackhawk Formation (2)	0.21	0.15	0.0112	54
	Upper Blackhawk Formation (3)	0.24	0.17	0.0064	83
	Lower Castlegate Sandstone (4)	0.24	0.17	0.0115	50
	Middle Castlegate Sandstone (5)	0.19	0.13	0.0061	56
	Upper Castlegate Sandstone (6)	0.22	0.15	0.0046	67
	Price River Formation (7)	0.22	0.15	0.0060	26
Mellor Canyon	Lower Blackhawk Formation (1)	0.17	0.12	0.0041	206
	Middle Blackhawk Formation (2)	0.17	0.12	0.0041	206
	Upper Blackhawk Formation (3)	0.17	0.12	0.0041	206
	Lower Castlegate Sandstone (4)	0.11	0.08	0.0028	62
	Middle Castlegate Sandstone (5)	0.11	0.08	0.0028	62
	Upper Castlegate Sandstone (6)	0.11	0.08	0.0028	62
	Price River Formation (7)	0.11	0.08	0.0028	62
Price Canyon	Lower Blackhawk Formation (1)	N/A	N/A	N/A	N/A
	Middle Blackhawk Formation (2)	N/A	N/A	N/A	N/A
	Upper Blackhawk Formation (3)	0.18	0.13	0.0053	104
	Lower Castlegate Sandstone (4)	0.16	0.12	0.0032	77
	Middle Castlegate Sandstone (5)	0.16	0.12	0.0032	58
	Upper Castlegate Sandstone (6)	0.18	0.13	0.0046	62
	Price River Formation (7)	0.29	0.20	0.0056	146
Salina Canyon	Lower Blackhawk Formation (1)	0.20	0.14	0.0046	34
	Middle Blackhawk Formation (2)	0.21	0.15	0.0046	21
	Upper Blackhawk Formation (3)	0.23	0.16	0.0054	77
	Lower Castlegate Sandstone (4)	0.22	0.15	0.0056	57

	Middle Castlegate Sandstone (5)	0.18	0.12	0.0033	140
	Upper Castlegate Sandstone (6)	0.16	0.11	0.0030	106
	Price River Formation (7)	0.24	0.17	0.0072	41
Sixmile Canyon	Lower Blackhawk Formation (1)	0.35	0.25	0.0201	40
	Middle Blackhawk Formation (2)	0.35	0.25	0.0201	40
	Upper Blackhawk Formation (3)	0.35	0.25	0.0201	40
	Lower Castlegate Sandstone (4)	0.33	0.23	0.0185	76
	Middle Castlegate Sandstone (5)	0.33	0.23	0.0185	76
	Upper Castlegate Sandstone (6)	0.33	0.23	0.0185	76
	Price River Formation (7)	0.18	0.13	0.0047	37
Straight Canyon	Lower Blackhawk Formation (1)	0.25	0.18	0.0036	116
	Middle Blackhawk Formation (2)	0.20	0.14	0.0037	69
	Upper Blackhawk Formation (3)	0.19	0.13	0.0021	84
	Lower Castlegate Sandstone (4)	0.18	0.13	0.0031	52
	Middle Castlegate Sandstone (5)	0.16	0.11	0.0028	49
	Upper Castlegate Sandstone (6)	0.23	0.16	0.0037	107
	Price River Formation (7)	N/A	N/A	N/A	N/A
Wattis Road	Lower Blackhawk Formation (1)	0.17	0.12	0.0028	40
	Middle Blackhawk Formation (2)	0.18	0.12	0.0030	49
	Upper Blackhawk Formation (3)	0.18	0.12	0.0024	61
	Lower Castlegate Sandstone (4)	0.18	0.12	0.0034	33
	Middle Castlegate Sandstone (5)	0.16	0.11	0.0025	60
	Upper Castlegate Sandstone (6)	0.18	0.12	0.0037	29
	Price River Formation (7)	N/A	N/A	N/A	N/A

S5. Grain-size sample sufficiency

Ancillary data collection was conducted to test whether grain-size sample size was sufficient. These tests determined that counts of 100 and 50 clasts for coarse-fractions and sand-fractions, respectively, successfully recovered stable D_{50} estimates.

To check whether sample size in grain-size counts is sufficient, the iterative D_{50} was calculated to determine the number of counts required to produce stable estimates of D_{50} for each grain-size fraction (Figs S3, S4). D_{50} estimates were considered to be stable when the iterative D_{50} fluctuates within ~10 mm for boulder- and cobble-grade sediments, within ~2–3 mm for pebble-grade sediments and within ~0.1 mm for sand-grade sediments. Iterative estimates of D_{50} suggest that, for coarse-fractions, <80–90 clast counts are sufficient to converge towards the median (Figs S3, S4), whereas for sand-fractions, <30–40 counts are required (Fig. S3). Therefore, counts of 100 and 50 for coarse-fractions and sand-fractions, respectively, should successfully recover stable D_{50} estimates. However, where sand-fractions were poorly sorted 100 clasts were counted for certainty.

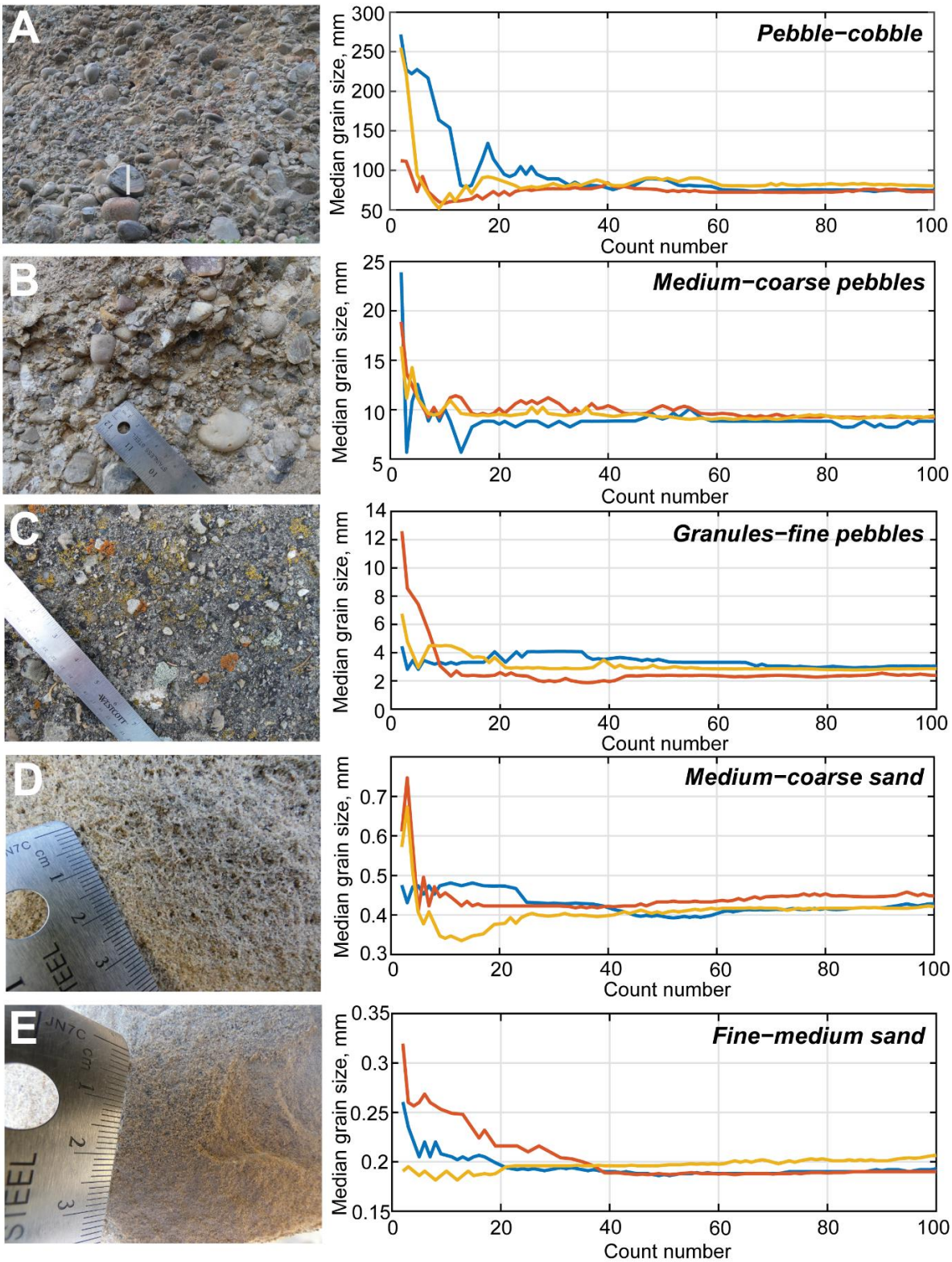

Figure S3: *The iterative convergence of median grain-size for (A) pebbles–cobbles, (B) medium–coarse pebbles, (C) granules–fine pebbles, (D) medium–coarse sand, and (E) fine–medium sand, as calculated from scaled photographs in ImageJ software. Three repeat counts were taken for each scaled photograph (red, blue and yellow solid lines). White bar in part A is 400 mm long.*

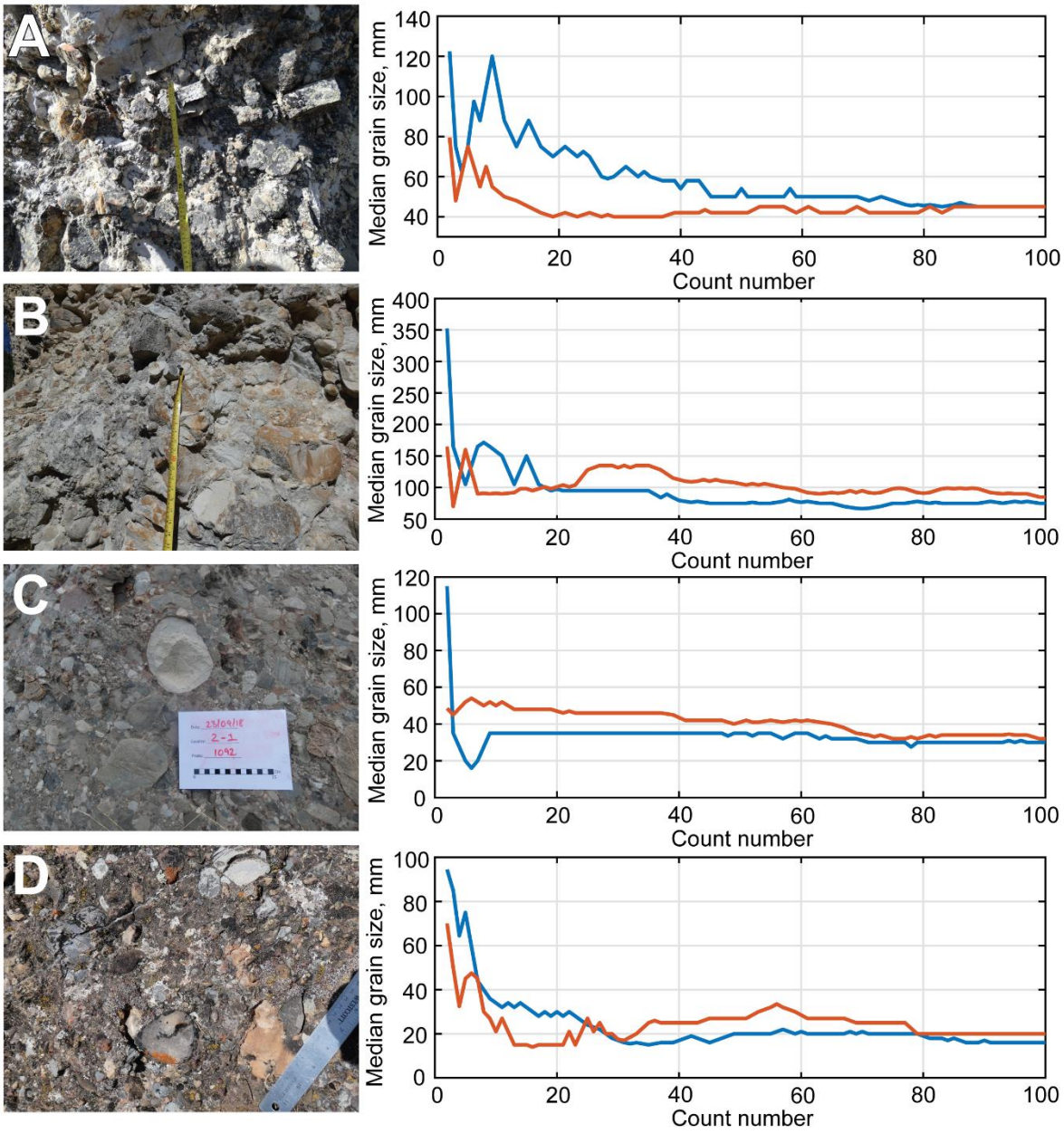

Figure S4: *The iterative convergence of median grain-size for different outcrops of gravel-grade sediments (A–D), as calculated from field Wolman counts. Repeat counts were taken (red and blue solid lines.*

S6. Secondary field data

As discussed in the main text, extensive work in this region has already focused on measuring geometries of architectural scale elements, which has increasingly exploited access to high-resolution imagery and three-dimensional outcrop models (Hajek & Heller, 2012; Rittersbacher et al., 2014; Flood & Hampson, 2015; Chamberlin & Hajek, 2019). These tools lend themselves to precise constraints on architectural geometries. As such, to the decision was made to primarily focus on grain-size and cross-set measurements in our field data collection, and secondary data providing constraints on architectural geometries were subsequently compiled. Specifically, data were compiled for independent indicators/proxies of palaeoflow depths (Table S4) and palaeoflow width (Table S5). The latter is particularly difficult to constrain from outcrop and, as such, indicators of palaeoflow width

tend to offer apparent widths, maximum widths, or a first-order sense as to the magnitude of width. These secondary data are supplemented by some of our own field observations at each field locality, where possible (Tables S4, S5), which were measured with a Haglof Laser Geo laser range finder to a precision of ±5 cm.

Given that we implement our field data in an entirely quantitative framework, independent observations and measurements of palaeoflow depths and palaeoflow widths are useful to corroborate estimates from this study (see Results). In addition, these constraints on the approximate, or order-of-magnitude, widths of these palaeorivers are further useful in probing the planform morphologies of these systems in both space and time (see Results).

Table S4: *A compilation of field measurements (secondary data from published literature) for architectural scale elements, e.g. bar heights, that are commonly used as palaeoflow depth proxies. For each secondary data set we include the stratigraphic interval it would be assigned in this study (1–7) and the field location from which the data set was collected. 1 = lower Blackhawk Formation; 2 = middle Blackhawk Formation; 3 = upper Blackhawk Formation; 4 = lower Castlegate Sandstone; 5 = middle Castlegate Sandstone; 6 = upper Castlegate Sandstone (Bluecastle Tongue); 7 = Price River Formation.*

Stratigraphic interval	Location	Value (m)	Proxy	Reference
Lower Blackhawk Formation (1)	South of Straight Canyon	7	Mean apparent height of channelized fluvial sandstone bodies	Flood and Hampson (2015)
Middle Blackhawk Formation (2)	South of Straight Canyon	8	Mean apparent height of channelized fluvial sandstone bodies	Flood and Hampson (2015)
Upper Blackhawk Formation (3)	South of Straight Canyon	7, 6	Mean apparent height of channelized fluvial sandstone bodies	Flood and Hampson (2015)
Blackhawk Formation (1–3)	Link Canyon	2 to >14	Channel story height	Hampson et al. (2013)
Blackhawk Formation (1–3)	Salina Canyon	0.5–2	Fining upward bed sets	Adams and Bhattacharya (2005)
Blackhawk Formation (1–3)	Salina Canyon	1–2	Bar heights	Adams and Bhattacharya (2005)
Blackhawk Formation (1–3)	Salina Canyon	5–8	Channel-belt sandstone body heights	Adams and Bhattacharya (2005)
Lower Castlegate Sandstone (4)	Price Canyon	4.1	Mean bar height	Hajek and Heller (2012)

Lower Castlegate Sandstone (4)	Price Canyon	1.1–7.6	Bar height	McLaurin and Steel (2007)
Lower Castlegate Sandstone (4)	Price Canyon	4.1 (1.5 to >8)	Mean bar height (and range)	Lynds and Hajek (2006)
Castlegate Sandstone (4–6)	Price Canyon	2.6	Mean bar height	Chamberlin and Hajek (2019)
Castlegate Sandstone (4–6)	Straight Canyon	3.6	Mean bar height	Chamberlin and Hajek (2019)
Castlegate Sandstone (4–6)	Salina Canyon	3.9	Mean bar height	Chamberlin and Hajek (2019)
Castlegate Sandstone (4–6)	Salina Canyon	1.5–2	Bar heights	Adams and Bhattacharya (2005)
Castlegate Sandstone (4–6)	Salina Canyon	3–5	Channel story heights	Adams and Bhattacharya (2005)
Blackhawk Formation (1–3)	Bear Canyon	2.1, 2.5, 3.9, 2.3, 1.8, 3.1, 3.5, 3.6, 2.5, 1.6, 2.5, 2.3, 1.5, 2.6	Lateral accretion set heights/channelized fluvial sandstone body heights	**This study**
Blackhawk Formation (1–3)	Salina Canyon	3.5, 4.6, 2, 2.1, 2.7, 5.8, 7.5, 3.7, 5.8, 6.6, 6.7	Lateral accretion set heights/channelized fluvial sandstone body heights	**This study**
Blackhawk Formation (1–3)	Link Canyon	3, 5.1, 5.4, 4.8, 4.7, 3.5, 2.1, 3, 4.5, 3.1, 3.2, 2.2, 1.5, 2.5, 3.3, 3.8, 4.4, 4.5, 3.2	Lateral accretion set heights/channelized fluvial sandstone body heights	**This study**
Blackhawk Formation (1–3)	Price Canyon	2.4, 2.3, 1.9, 1.9, 1.7, 1.6, 1.5	Lateral accretion set heights/channelized fluvial sandstone body heights	**This study**
Blackhawk Formation (1–3)	Straight Canyon	3.5, 5, 2, 3.5, 6.7, 3, 6, 3.7	Lateral accretion set heights/channelized fluvial sandstone body heights	**This study**

Blackhawk Formation (1–3)	Wattis Road	2.2, 3.5, 2.3, 2, 2.4, 1.7	Lateral accretion set heights/channelized fluvial sandstone body heights	**This study**
Castlegate Sandstone (4–6)	Bear Canyon	4, 6.4, 2.8, 2.9, 4.7, 3.4, 2.9, 4.1, 3.2, 2.1, 2.1	Lateral accretion set heights/channelized fluvial sandstone body heights	**This study**
Castlegate Sandstone (4–6)	Price Canyon	3.4, 3, 3.5, 2, 2.2, 2.8, 3	Lateral accretion set heights/channelized fluvial sandstone body heights	**This study**
Castlegate Sandstone (4–6)	Wattis Road	3.9, 4	Lateral accretion set heights/channelized fluvial sandstone body heights	**This study**
Castlegate Sandstone (4–6)	Salina Canyon	1.6, 2.8, 2.2, 2, 3.8, 3.2, 2.3, 2.8, 1.9, 3.7, 2.4, 2.3, 2.6, 4.1	Lateral accretion set heights/channelized fluvial sandstone body heights	**This study**
Castlegate Sandstone (4–6)	Link Canyon	1.6, 3.6, 2.3, 4.3, 3.1, 3.6, 2, 3.8, 0.75, 1.1, 1.1, 1.3, 2.4, 2.5	Lateral accretion set heights/channelized fluvial sandstone body heights	**This study**
Price River Formation (1–3)	Price Canyon	7	Lateral accretion set heights/channelized fluvial sandstone body heights	**This study**
Price River Formation (7)	Bear Canyon	3.7, 2.1, 2.4, 2.15, 4.1, 5.2, 0.9, 2.2, 1.4	Lateral accretion set heights/channelized fluvial sandstone body heights	**This study**

Table S5: *A compilation of field measurements (secondary data from published literature) for architectural scale elements, e.g. sand*stone *bodies, that are commonly used as a proxy to infer the magnitude of channel width. For each secondary data set we include the stratigraphic interval it would be assigned in this study (1–7) and the field location from which the data set was collected. 1 = lower Blackhawk Formation; 2 = middle Blackhawk Formation; 3 = upper Blackhawk Formation; 4 = lower*

Castlegate Sandstone; 5 = middle Castlegate Sandstone; 6 = upper Castlegate Sandstone (Bluecastle Tongue); 7 = (lowermost) Price River Formation.

Stratigraphic interval	Location	Value (m)	Proxy	Reference
Lower Blackhawk Formation (1)	South of Straight Canyon	350	Mean apparent width of channelized fluvial sandstone bodies	Flood and Hampson (2015)
Middle Blackhawk Formation (2)	South of Straight Canyon	370	Mean apparent width of channelized fluvial sandstone bodies	Flood and Hampson (2015)
Upper Blackhawk Formation (3)	South of Straight Canyon	420, 390	Mean apparent width of channelized fluvial sandstone bodies	Flood and Hampson (2015)
Blackhawk Formation (1–3)	Link Canyon	30 to >310	Channel story widths	Hampson et al. (2013)
Blackhawk Formation (1–3)	Link Canyon	>120 to >740	Channel belt widths	Hampson et al. (2013)
Blackhawk Formation (1–3)	Salina Canyon	8–~50	Bar widths	Adams and Bhattacharya (2005)
Lower Castlegate Sandstone (4)	Price Canyon	30, 35 (max >100)	Thalweg and bar widths	McLaurin and Steel (2007)
Castlegate Sandstone (4–6)	Price Canyon	58	Mean bar package width	Chamberlin and Hajek (2019)
Castlegate Sandstone (4–6)	Straight Canyon	180	Mean bar package width	Chamberlin and Hajek (2019)
Castlegate Sandstone (4–6)	Salina Canyon	87	Mean bar package width	Chamberlin and Hajek (2019)

S7. Goodness of fits on palaeoslope profiles inc. resolved steepness indexes

As described in the Methods, palaeorelief was reconstructed in the alluvial domain of Late Cretaceous central Utah palaeorivers. Initially, palaeoslope was reconstructed using 2 independent methods, a Shields stress inversion (Equation 3) and the approach of Trampush et al. (2014) (Equation 4). Palaeoslope estimates from each method were then used to estimate palaeorelief (see Methods and Results). In doing so, we a non-linear least squares regression was used to derive best-fit palaeoslope

profiles for the defined northern and southern transects using Equation 7. In doing so, three different values for the concavity index, θ, were assumed given that concavity in these ancient rivers is not known. Plausible values of 0.4, 0.5 and 0.6 were used for θ. Using the two sets of palaeoslope estimates (Equations 3 and 4) and the three different concavity values, a variety of steepness indexes, k_s (Equation 7), were recovered for the defined northern and southern depositional-dip transects, for each stratigraphic interval (where possible). These results are presented here; Table S6 details all k_s values recovered when reconstructing best-fit palaeoslope profiles, and also reports goodness of fit (R^2).

Table S6: *Steepness indexes, k_s, recovered for the defined northern and southern depositional-dip transects, through each stratigraphic interval (1–7), where possible. 1 =l Blackhawk Formation; 2 = middle Blackhawk Formation; 3 = upper Blackhawk Formation; 4 = lower Castlegate Sandstone; 5 = middle Castlegate Sandstone; 6 = upper Castlegate Sandstone (Bluecastle Tongue); 7 = (lowermost) Price River Formation. k_s values are calculated using palaeoslope estimates derived from both Equations 3 and 4, and using a concavity index, θ, of either 0.4, 0.5, or 0.6. R^2 values are given for each k_s value.*

Transect	**Stratigraphic interval**	**Concavity index, θ**											
		0.4				0.5				0.6			
		Shields stress inversion (Equation 3)		Trampush et al. 2014 (Equation 4)		Shields stress inversion (Equation 3)		Trampush et al. 2014 (Equation 4)		Shields stress inversion (Equation 3)		Trampush et al. 2014 (Equation 4)	
		k_s ($m^{0.8}$)	R^2	k_s ($m^{0.8}$)	R^2	k_s (m^{1})	R^2	k_s (m^{1})	R^2	k_s ($m^{1.2}$)	R^2	k_s ($m^{1.2}$)	R^2
Northern transect	Price River Fm (7)	18.3	0.67	12.3	0.81	34.9	0.77	23.1	0.89	64.7	0.84	42.4	0.94
	Upper Castlegate Sst (6)	16.4	0.34	10.2	0.91	22.5	0.25	14.6	0.88	30.2	0.16	20.3	0.82
	Middle Castlegate Sst (5)	16.4	0.34	10.3	0.91	22.5	0.25	14.6	0.88	30.2	0.17	20.3	0.82
	Lower Castlegate Sst (4)	14.1	0.58	9.6	0.99	19.6	0.5	13.8	0.98	26.7	0.41	19.3	0.95
	Upper Blackhawk Fm (3)	6.1	0.98	8.3	0.99	8.6	0.99	11.6	0.98	12.0	0.99	16.0	0.96
	Middle Blackhawk Fm (2)	6.1	0.96	8.1	0.98	8.6	0.99	11.4	0.99	11.9	0.99	15.8	0.99
	Lower Blackhawk Fm (1)	N/A	N/A	N/A	N/A	N/A	N/A	N/A	N/A	N/A	N/A	N/A	N/A
Southern transect	Price River Fm (7)	15.8	0.90	5.9	0.98	22.6	0.95	8.4	0.99	31.8	0.98	11.7	0.99
	Upper Castlegate Sst (6)	15.3	0.88	5.8	0.94	22.2	0.94	8.3	0.97	31.5	0.97	11.6	0.98
	Middle Castlegate Sst (5)	15.4	0.88	5.9	0.92	22.4	0.94	8.4	0.94	31.6	0.97	11.7	0.94
	Lower Castlegate Sst (4)	15.4	0.88	5.9	0.93	22.3	0.94	8.4	0.95	31.6	0.97	11.7	0.94
	Upper Blackhawk Fm (3)	3.5	0.91	3.1	0.89	5.1	0.96	4.4	0.89	7.2	0.98	6.1	0.86
	Middle Blackhawk Fm (2)	3.5	0.91	3.1	0.90	5.1	0.96	4.3	0.90	7.2	0.98	6.0	0.88
	Lower Blackhawk Fm (1)	3.5	0.90	3.0	0.91	5.1	0.95	4.3	0.92	7.2	0.98	6.0	0.91

S8. Additional results

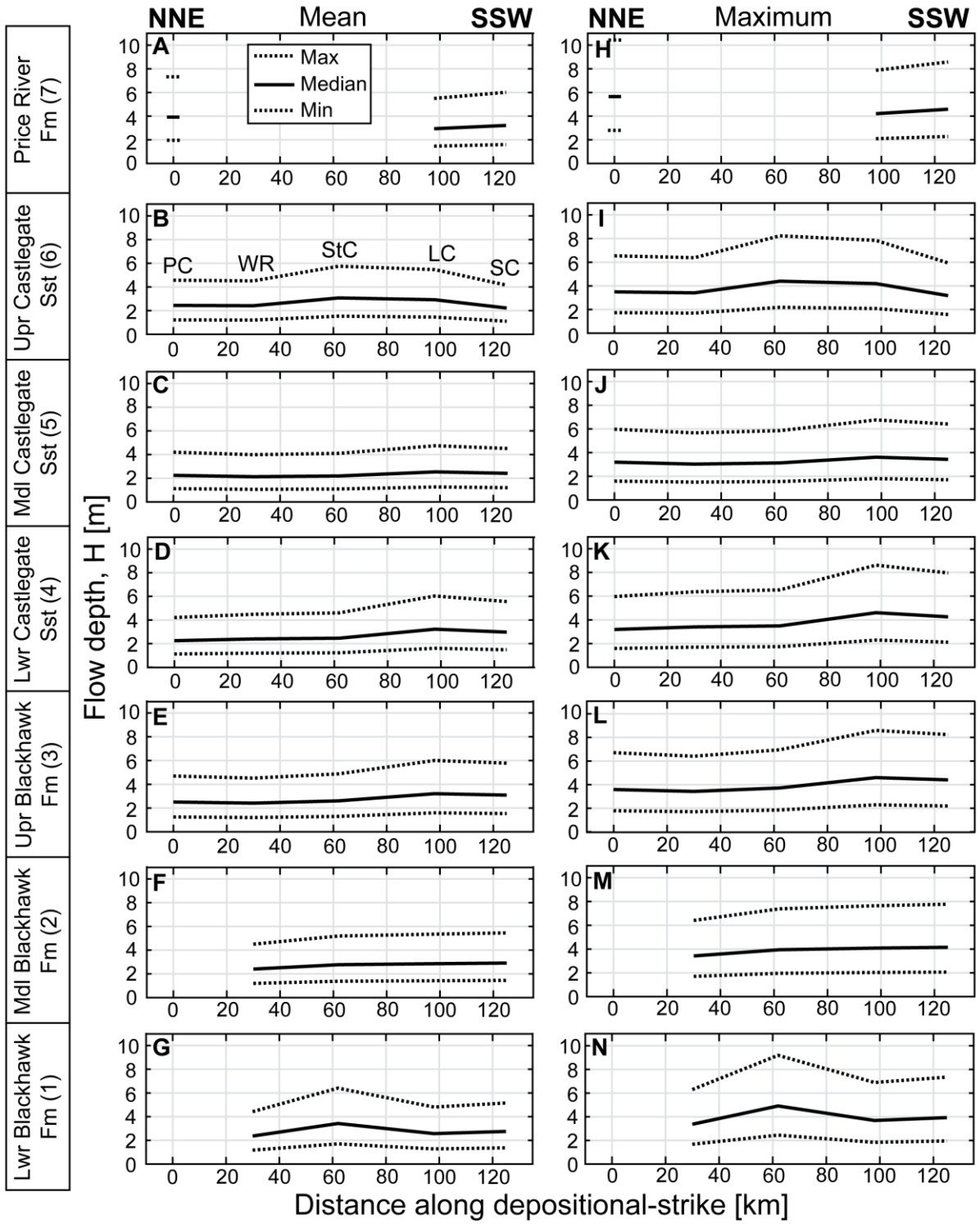

Figure S5: *Reconstructed palaeoflow depths for the 5 parallel fluvial systems, for each stratigraphic interval where possible. Parts A–G depict reconstructed palaeoflow depths from estimated mean cross-set heights, whereas parts H–N depict reconstructed palaeoflow depths from measured maximum cross-set heights. Results are presented as along-depositional strike transects from NNE (left; 0 km) to SSW (right; 125 km). Field sites span Price Canyon (PC), Wattis Road (WR), Straight Canyon (StC), Link Canyon (LC) and Salina Canyon (SC). Solid lines indicate median palaeoflow depths and dashed lines*

indicate plausible minimum and maximum values for median palaeoflow depths, derived from the uncertainty margins in Equation 2.

Adams, M. M., & Bhattacharya, J. P. (2005). No change in fluvial style across a sequence boundary, Cretaceous Blackhawk and Castlegate formations of central Utah, U.S.A. *Journal of Sedimentary Research, 75*(6), 1038-1051. doi:10.2110/jsr.2005.080

Allen, J. R. L. (1982a). *Sedimentary Structures; Their Character and Physical Basis. Volume I* (Vol. 30). Amsterdam: Elsevier.

Allen, J. R. L. (1982b). *Sedimentary Structures; Their Character and Physical Basis. Volume II* (Vol. 30). Amsterdam: Elsevier.

Allen, P. A. (2008a). From landscapes into geological history. *Nature, 451*, 274-276. doi:10.1038/nature06586

Allen, P. A. (2008b). Time scales of tectonic landscapes and their sediment routing systems. *Geological Society, London, Special Publications, 296*(1), 7-28. doi:10.1144/sp296.2

Allen, P. A., Armitage, J. J., Carter, A., Duller, R. A., Michael, N. A., Sinclair, H. D., . . . Whittaker, A. C. (2013). The *Qs* problem: Sediment volumetric balance of proximal foreland basin systems. *Sedimentology, 60*(1), 102-130. doi:10.1111/sed.12015

Allmendinger, R. W. (1992). Fold and thrust tectonics of the western United States exclusive of the accreted terranes. In B. C. Burchfiel, P. W. Lipman, & M. L. Zoback (Eds.), *The Cordilleran Orogen*: Geological Society of America.

Andrews, E. D. (1984). Bed-material entrainment and hydraulic geometry of gravel-bed rivers in Colorado. *GSA Bulletin, 95*(3), 371-378. doi:10.1130/0016-7606(1984)95<371:BEAHGO>2.0.CO;2

Armitage, J. J., Duller, R. A., Whittaker, A. C., & Allen, P. A. (2011). Transformation of tectonic and climatic signals from source to sedimentary archive. *Nature Geoscience, 4*(4), 231-235. doi:10.1038/ngeo1087

Armstrong, R. L. (1968). Sevier Orogenic Belt in Nevada and Utah. *GSA Bulletin, 79*(4), 429-458. doi:10.1130/0016-7606(1968)79[429:SOBINA]2.0.CO;2

Aschoff, J., & Steel, R. (2011a). Anatomy and development of a low-accommodation clastic wedge, upper Cretaceous, Cordilleran Foreland Basin, USA. *Sedimentary Geology, 236*(1), 1-24. doi:10.1016/j.sedgeo.2010.10.006

Aschoff, J., & Steel, R. (2011b). Anomalous clastic wedge development during the Sevier-Laramide transition, North American Cordilleran foreland basin, USA. *GSA Bulletin, 123*(9-10), 1822-1835. doi:10.1130/B30248.1

Bartschi, N. C., Saylor, J. E., Lapen, T. J., Blum, M. D., Pettit, B. S., & Andrea, R. A. (2018). Tectonic controls on Late Cretaceous sediment provenance and stratigraphic architecture in the Book Cliffs, Utah. *GSA Bulletin, 130*(11-12), 1763-1781. doi:10.1130/B31927.1

Bhattacharya, J., & Tye, B. (2004). Searching for modern Ferron analogs and application to subsurface interpretation. In T. C. Chidsey Jr., R. D. Adams, & T. H. Morris (Eds.), *Regional to Wellbore Analog for Fluvial-Deltaic Reservoir Modeling: The Ferron Sandstone of Utah* (Vol. 50, pp. 39-57): AAPG Studies in Geology.

Bhattacharya, J. P., Copeland, P., Lawton, T. F., & Holbrook, J. (2016). Estimation of source area, river paleo-discharge, paleoslope, and sediment budgets of linked deep-time depositional systems and implications for hydrocarbon potential. *Earth-Science Reviews, 153*, 77-110. doi:10.1016/j.earscirev.2015.10.013

Bhattacharyya, P., Bhattacharya, J. P., & Khan, S. D. (2015). Paleo-channel reconstruction and grain size variability in fluvial deposits, Ferron Sandstone, Notom Delta, Hanksville, Utah. *Sedimentary Geology, 325*, 17-25. doi:10.1016/j.sedgeo.2015.05.001

Boulton, S. J., & Whittaker, A. C. (2009). Quantifying the slip rates, spatial distribution and evolution of active normal faults from geomorphic analysis: Field examples from an oblique-extensional graben, southern Turkey. *Geomorphology, 104*(3), 299-316. doi:10.1016/j.geomorph.2008.09.007

Bradley, R. W., & Venditti, J. G. (2017). Reevaluating dune scaling relations. *Earth-Science Reviews, 165*, 356-376. doi:10.1016/j.earscirev.2016.11.004

Brewer, C. J., Hampson, G. J., Whittaker, A. C., Roberts, G. G., & Watkins, S. E. (2020). Comparison of methods to estimate sediment flux in ancient sediment routing systems. *Earth-Science Reviews, 207*, 103217. doi:10.1016/j.earscirev.2020.103217

Bridge, J. S., & Mackey, S. D. (1993). A revised alluvial stratigraphy model. In M. Marzo & C. Puigdefábregas (Eds.), *Alluvial Sedimentation* (pp. 317-336): Wiley-Blackwell.

Bridge, J. S., & Tye, B. (2000). Interpreting the dimensions of ancient fluvial channel bars, channels, and channel belts from wireline-logs and cores. *AAPG Bulletin, 84*(8), 1205-1228. doi:10.1306/A9673C84-1738-11D7-8645000102C1865D

Brooke, S. A. S., Whittaker, A., Armitage, J. J., D'Arcy, M., & Watkins, S. E. (2018). Quantifying sediment transport dynamics on alluvial fans from spatial and temporal changes in grain size, Death Valley, California. *Journal of Geophysical Research: Earth Surface, 123*, 2039-2067.

Bruhn, R. L., Picard, M. D., & Isby, J. S. (1986). Tectonics and Sedimentology of Uinta Arch, Western Uinta Mountains, and Uinta Basin. In J. A. Peterson (Ed.), *Paleotectonics and sedimentation in the Rocky Mountain Region, United States* (Vol. 41): American Association of Petroleum Geologists.

Bryant, B., & Nichols, D. J. (1988). Late Mesozoic and early Tertiary reactivation of an ancient crustal boundary along the Uinta trend and its interaction with the Sevier orogenic belt. In C. J. Schmidt & W. J. Perry, Jr. (Eds.), *Interaction of the Rocky Mountain Foreland and the Cordilleran Thrust Belt* (Vol. 171): Geological Society of America.

Buhler, P. B., Fassett, C. I., Head, J. W., & Lamb, M. P. (2014). Timescales of fluvial activity and intermittency in Milna Crater, Mars. *Icarus, 241*, 130-147. doi:10.1016/j.icarus.2014.06.028

Carling, P. A. (1999). Subaqueous gravel dunes. *Journal of Sedimentary Research, 69*(3), 534-545. doi:10.2110/jsr.69.534

Carlston, C. W. (1969). Longitudinal slope characteristics of rivers of the midcontinent and the Atlantic east gulf slopes. *International Association of Scientific Hydrology - Bulletin, 14*(4), 21-31. doi:10.1080/02626666909493751

Castelltort, S., Goren, L., Willett, S. D., Champagnac, J.-D., Herman, F., & Braun, J. (2012). River drainage patterns in the New Zealand Alps primarily controlled by plate tectonic strain. *Nature Geoscience, 5*(10), 744-748. doi:10.1038/ngeo1582

Castelltort, S., Simpson, G., & Darrioulat, A. (2009). Slope-control on the aspect ratio of river basins. *Terra Nova, 21*(4), 265-270. doi:10.1111/j.1365-3121.2009.00880.x

Castelltort, S., & Van Den Driessche, J. (2003). How plausible are high-frequency sediment supply-driven cycles in the stratigraphic record? *Sedimentary Geology, 157*(1), 3-13. doi:10.1016/S0037-0738(03)00066-6

Chamberlin, E. P., & Hajek, E. A. (2019). Using bar preservation to constrain reworking in channel-dominated fluvial stratigraphy. *Geology, 47*(6), 531-534. doi:10.1130/G46046.1

Champagnac, J.-D., Molnar, P., Sue, C., & Herman, F. (2012). Tectonics, climate, and mountain topography. *Journal of Geophysical Research: Solid Earth, 117*(B2). doi:10.1029/2011JB008348

Chase, C. G., Gregory-Wodzicki, K. M., Parrish, J. T., & DeCelles, P. G. (1998). Topographic history of the Western Cordillera of North America and controls on climate. In T. J. Crowley & K. Burke (Eds.), *Tectonic Boundary Conditions for Climate Reconstructions* (Vol. 39, pp. 73-99): Oxford Monographs on Geology and Geophysics.

Chen, C., Guerit, L., Foreman, B. Z., Hassenruck-Gudipati, H. J., Adatte, T., Honegger, L., . . . Castelltort, S. (2018). Estimating regional flood discharge during Palaeocene-Eocene global warming. *Scientific Reports, 8*(1), 13391. doi:10.1038/s41598-018-31076-3

Chitale, S. V. (1970). River Channel Patterns. *Journal of Hydraulic Division American Society Civil Engineering, 96*, 201-221.

Church, M., & Rood, K. (1983). *Catalogue of Alluvial River Channel Regime Data* (Vol. 99). Vancouver: University of British Columbia.

Cobban, W. A., McKinney, K. C., Obradovich, J. D., & Walasczyk, I. (2006). A USGS zonal table for the Upper Cretaceous Middle Cenomanian–Maastrichtian of the Western Interior of the United States based on Ammonites, Inoceramids, and radiometric ages: U.S. Geological Survey, Open-File Report 2006-1250. 1-46.

Colombera, L., Arévalo, O. J., & Mountney, N. P. (2017). Fluvial-system response to climate change: The Paleocene-Eocene Tremp Group, Pyrenees, Spain. *Global and Planetary Change, 157*, 1-17. doi:10.1016/j.gloplacha.2017.08.011

Constenius, K., Esser, R., & Layer, P. (2003). Extensional collapse of the Charleston-Nebo salient and its relationship to space-time variations in Cordilleran orogenic belt tectonism and continental stratigraphy. *Cenozoic systems of the Rocky Mountain region, Raynolds, R.G. and Flores, R. M., eds.,Rocky Mountain Section, Society of Economic Paleontologists and Mineralogists*, 303-353.

D'Arcy, M., & Whittaker, A. C. (2014). Geomorphic constraints on landscape sensitivity to climate in tectonically active areas. *Geomorphology, 204*, 366-381. doi:10.1016/j.geomorph.2013.08.019

D'Arcy, M., Whittaker, A. C., & Roda-Boluda, D. C. (2017). Measuring alluvial fan sensitivity to past climate changes using a self-similarity approach to grain-size fining, Death Valley, California. *Sedimentology, 64*(2), 388-424. doi:10.1111/sed.12308

Dade, W. B., & Friend, P. F. (1998). Grain size, sediment transport regime, and channel slope in alluvial rivers. *The Journal of Geology, 106*(6), 661-676. doi:10.1086/516052

DeCelles, P. G. (1994). Late Cretaceous–Paleocene synorogenic sedimentation and kinematic history of the Sevier thrust belt, northeast Utah and southwest Wyoming. *GSA Bulletin, 106*, 32-56. doi:10.1130/0016-7606(1994)106<0032:LCPSSA>2.3.CO;2

DeCelles, P. G. (2004). Late Jurassic to Eocene evolution of the Cordilleran thrust belt and foreland basin system, western U.S.A. *American Journal of Science, 304*. doi:10.2475/ajs.304.2.105

DeCelles, P. G., & Coogan, J. C. (2006). Regional structure and kinematic history of the Sevier fold-and-thrust belt, central Utah. *GSA Bulletin, 118*(7/8), 841-864. doi:10.1130/B25759.1

DiBiase, R. A., & Whipple, K. X. (2011). The influence of erosion thresholds and runoff variability on the relationships among topography, climate, and erosion rate. *Journal of Geophysical Research: Earth Surface, 116*(F4). doi:10.1029/2011JF002095

DiBiase, R. A., Whipple, K. X., Heimsath, A. M., & Ouimet, W. B. (2010). Landscape form and millennial erosion rates in the San Gabriel Mountains, CA. *Earth and Planetary Science Letters, 289*(1), 134-144. doi:10.1016/j.epsl.2009.10.036

Duller, R. A., Armitage, J. J., Manners, H. R., Grimes, S., & Jones, T. D. (2019). Delayed sedimentary response to abrupt climate change at the Paleocene-Eocene boundary, northern Spain. *Geology, 47*(2), 159-162. doi:10.1130/G45631.1

Duller, R. A., Whittaker, A. C., Fedele, J. J., Whitchurch, A. L., Springett, J., Smithells, R., . . . Allen, P. A. (2010). From grain size to tectonics. *Journal of Geophysical Research: Earth Surface, 115*(F3), F03022. doi:10.1029/2009JF001495

Eide, C. H., Müller, R., & Helland-Hansen, W. (2018). Using climate to relate water discharge and area in modern and ancient catchments. *Sedimentology, 65*(4), 1378-1389. doi:10.1111/sed.12426

Ferguson, R. I., & Church, M. (2004). A simple universal equation for grain settling velocity. *Journal of Sedimentary Research, 74*(6), 933-937. doi:10.1306/051204740933

Fernandes, V. M., Roberts, G. G., White, N., & Whittaker, A. C. (2019). Continental-Scale Landscape Evolution: A History of North American Topography. *Journal of Geophysical Research: Earth Surface, 124*(11), 2689-2722. doi:10.1029/2018JF004979

Flint, J. J. (1974). Stream gradient as a function of order, magnitude, and discharge. *Water Resources Research, 10*(5), 969-973. doi:10.1029/WR010i005p00969

Flood, Y. S., & Hampson, G. J. (2014). Facies and architectural analysis to interpret avulsion style and variability: Upper Cretaceous Blackhawk Formation, Wasatch Plateau, central Utah, U.S.A. *Journal of Sedimentary Research, 84*(9), 743-762. doi:10.2110/jsr.2014.59

Flood, Y. S., & Hampson, G. J. (2015). Quantitative analysis of the dimensions and distribution of channelized fluvial sandbodies within a large outcrop dataset: Upper Cretaceous Blackhawk Formation, Wasatch Plateau, central Utah, U.S.A. *Journal of Sedimentary Research, 85*(4), 315-336. doi:10.2110/jsr.2015.25

Foreman, B. Z. (2014). Climate-driven generation of a fluvial sheet sand body at the Paleocene–Eocene boundary in northwest Wyoming (USA). *Basin Research, 26*, 225-241. doi:10.1111/bre.12027

Foreman, B. Z., Heller, P. L., & Clementz, M. T. (2012). Fluvial response to abrupt global warming at the Palaeocene/Eocene boundary. *Nature, 491*, 92-95. doi:10.1038/nature11513

Foreman, B. Z., Roberts, E. M., Tapanila, L., Ratigan, D., & Sullivan, P. (2015). Stable isotopic insights into paleoclimatic conditions and alluvial depositional processes in the Kaiparowits Formation (Campanian, south-central Utah, U.S.A.). *Cretaceous Research, 56*, 180-192. doi:10.1016/j.cretres.2015.05.001

Fouch, T. D., Lawton, T. F., Nichols, D. J., Cashion, W. B., & Cobban, W. A. (1983). Patterns and timing of synorogenic sedimentation in Upper Cretaceous rocks of central and northeast Utah. In M. W. Reynolds & E. D. Dolly (Eds.), *Mesozoic Paleogeography of West-Central United States* (pp. 305-336): SEPM Rocky Mountain Section.

Fricke, H. C., Foreman, B. Z., & Sewall, J. O. (2010). Integrated climate model-oxygen isotope evidence for a North American monsoon during the Late Cretaceous. *Earth and Planetary Science Letters, 289*(1-2), 11-21. doi:10.1016/j.epsl.2009.10.018

Ganti, V., Hajek, E. A., Leary, K., Straub, K. M., & Paola, C. (2020). Morphodynamic hierarchy and the fabric of the sedimentary record. *Geophysical Research Letters, 47*(14), e2020GL087921. doi:10.1029/2020GL087921

Ganti, V., Lamb, M. P., & Chadwick, A. J. (2019a). Autogenic erosional surfaces in fluvio-deltaic stratigraphy from floods, avulsions, and backwater hydrodynamics. *Journal of Sedimentary Research, 89*(8), 815-832. doi:10.2110/jsr.2019.40

Ganti, V., Lamb, M. P., & McElroy, B. (2014). Quantitative bounds on morphodynamics and implications for reading the sedimentary record. *Nature Communications, 5*(1), 3298. doi:10.1038/ncomms4298

Ganti, V., Paola, C., & Foufoula-Georgiou, E. (2013). Kinematic controls on the geometry of the preserved cross sets. *Journal of Geophysical Research: Earth Surface, 118*(3), 1296-1307. doi:10.1002/jgrf.20094

Ganti, V., Whittaker, A., Lamb, M. P., & Fischer, W. W. (2019b). Low-gradient, single-threaded rivers prior to greening of the continents. *Proceedings of the National Academy of Sciences, 116*(4), 11652-11657. doi:10.1073/pnas.1901642116

Gill, J. R., & Hail Jr, W. J. (1975). Stratigraphic sections across Upper Cretaceous Mancos Shale-Mesaverde Group boundary, eastern Utah and western Colorado. *U.S. Geological Survey Publication, 68*. doi:10.3133/oc68

Gill, M. A. (1971). Height of sand dunes in open channel flows. *Journal of the Hydraulics Division, 97*(12), 2067-2074.

Hack, J. T. (1957). Studies of longitudinal stream profiles in Virigina and Maryland. *U.S. Geological Survey Professional Paper, 294-B*, 45-97.

1673 Hack, J. T. (1973). Stream profile analysis and stream gradient index. *US Geological Survey Journal of*
1674 *Research, 1*, 421–429.
1675 Hajek, E. A., & Heller, P. L. (2012). Flow-depth scaling in alluvial architecture and nonmarine
1676 sequence stratigraphy: Example from the Castlegate Sandstone, central Utah, U.S.A. *Journal*
1677 *of Sedimentary Research, 82*(2), 121-130. doi:10.2110/jsr.2012.8
1678 Hajek, E. A., Heller, P. L., & Sheets, B. A. (2010). Significance of channel-belt clustering in alluvial
1679 basins. *Geology, 38*(6), 535-538. doi:10.1130/G30783.1
1680 Hajek, E. A., & Wolinsky, M. A. (2012). Simplified process modeling of river avulsion and alluvial
1681 architecture: Connecting models and field data. *Sedimentary Geology, 257-260*, 1-30.
1682 doi:10.1016/j.sedgeo.2011.09.005
1683 Hampson, G. J. (2010). Sediment dispersal and quantitative stratigraphic architecture across an
1684 ancient shelf. *Sedimentology, 57*(1), 96-141. doi:10.1111/j.1365-3091.2009.01093.x
1685 Hampson, G. J., Duller, R. A., Petter, A. L., Robinson, R. A. J., & Allen, P. A. (2014). Mass-balance
1686 constraints on stratigraphic interpretation of linked alluvial–coastal–shelfal deposits from
1687 source to sink: example from Cretaceous Western Interior Basin, Utah and Colorado, U.S.A.
1688 *Journal of Sedimentary Research, 84*(11), 935-960. doi:10.2110/jsr.2014.78
1689 Hampson, G. J., Jewell, T. O., Irfan, N., Gani, M. R., & Bracken, B. (2013). Modest change in fluvial
1690 style with varying accommodation in regressive alluvial-to-coastal-plain wedge: Upper
1691 Cretaceous Blackhawk Formation, Wasatch Plateau, central Utah, U.S.A. *Journal of*
1692 *Sedimentary Research, 83*(2), 145-169. doi:10.2110/jsr.2013.8
1693 Hampson, G. J., Royhan Gani, M., Sahoo, H., Rittersbacher, A., Irfan, N., Ranson, A., . . . Bracken, B.
1694 (2012). Controls on large-scale patterns of fluvial sandbody distribution in alluvial to coastal
1695 plain strata: Upper Cretaceous Blackhawk Formation, Wasatch Plateau, Central Utah, USA.
1696 *Sedimentology, 59*(7), 2226-2258. doi:10.1111/j.1365-3091.2012.01342.x
1697 Hay, W., L. Eicher, D., & Diner, R. (1993). Physical oceanography and water masses of the Cretaceous
1698 Western Interior Seaway. In W. E. G. Caldwell & E. G. Kauffman (Eds.), *Evolution of the*
1699 *Western Interior Basin* (pp. 297-318): Geological Association of Canada.
1700 Hayden, A. T., Lamb, M. P., Fischer, W. W., Ewing, R. C., McElroy, B. J., & Williams, R. M. E. (2019).
1701 Formation of sinuous ridges by inversion of river-channel belts in Utah, USA, with
1702 implications for Mars. *Icarus, 332*, 92-110. doi:10.1016/j.icarus.2019.04.019
1703 Hettinger, R. D., & Kirschbaum, M. A. (2002). Stratigraphy of the Upper Cretaceous Mancos Shale
1704 (upper part) and Mesaverde Group in the southern part of the Uinta and Piceance basins,
1705 Utah and Colorado. *USGS Geologic Investigation Series: IMAP, 2764*, 21. doi:10.3133/i2764
1706 Holbrook, J., & Wanas, H. (2014). A fulcrum approach to assessing source-to-sink mass balance using
1707 channel paleohydrologic paramaters derivable from common fluvial data sets with an
1708 example from the Cretaceous of Egypt. *Journal of Sedimentary Research, 84*(5), 349-372.
1709 doi:10.2110/jsr.2014.29
1710 Horton, B. K., Constenius, K. N., & DeCelles, P. G. (2004). Tectonic control on coarse-grained
1711 foreland-basin sequences: An example from the Cordilleran foreland basin, Utah. *Geology,*
1712 *32*(7), 637-640. doi:10.1130/G20407.1
1713 Hovius, N. (1996). Regular spacing of drainage outlets from linear mountain belts. *Basin Research,*
1714 *8*(1), 29-44. doi:10.1111/j.1365-2117.1996.tb00113.x
1715 Jerolmack, D. J., & Mohrig, D. (2005). Frozen dynamics of migrating bedforms. *Geology, 33*(1), 57-60.
1716 doi:10.1130/G20897.1
1717 Jerolmack, D. J., & Paola, C. (2010). Shredding of environmental signals by sediment transport.
1718 *Geophysical Research Letters, 37*(19), 1-5. doi:10.1029/2010gl044638
1719 Jerolmack, D. J., & Sadler, P. (2007). Transience and persistence in the depositional record of
1720 continental margins. *Journal of Geophysical Research: Earth Surface, 112*(F3).
1721 doi:10.1029/2006JF000555
1722 Jinnah, Z. A., Roberts, E. M., Deino, A. L., Larsen, J. S., Link, P. K., & Fanning, C. M. (2009). New ^{40}Ar-
1723 ^{39}Ar and detrital zircon U-Pb ages for the Upper Cretaceous Wahweap and Kaiparowits

formations on the Kaiparowits Plateau, Utah: Implications for regional correlation, provenance, and biostratigraphy. *Cretaceous Research, 30*(2), 287-299. doi:10.1016/j.cretres.2008.07.012

Kauffman, E. G. (1977). Geological and biological overview: Western Interior Basin In E. G. Kauffman (Ed.), *Cretaceous facies, faunas, and paleoenvironments across the Western Interior Basin* (pp. 75-99): Rocky Mountain Association of Geologists.

Kauffman, E. G., & Caldwell, W. (1993). The Western Interior Basin in space and time. In E. G. Kauffman & W. Caldwell (Eds.), *Evolution of the Western Interior Basin: Geological Association of Canada, Special Paper 39* (pp. 1-30).

Kirby, E., & Whipple, K. (2001). Quantifying differential rock-uplift rates via stream profile analysis. *Geology, 29*(5), 415-418. doi:10.1130/0091-7613(2001)029<0415:QDRURV>2.0.CO;2

Kirby, E., & Whipple, K. X. (2012). Expression of active tectonics in erosional landscapes. *Journal of Structural Geology, 44*, 54-75. doi:10.1016/j.jsg.2012.07.009

Kirby, E., Whipple, K. X., Tang, W., & Chen, Z. (2003). Distribution of active rock uplift along the eastern margin of the Tibetan Plateau: Inferences from bedrock channel longitudinal profiles. *Journal of Geophysical Research: Solid Earth, 108*(B4). doi:10.1029/2001JB000861

Lamb, M. P., Grotzinger, J. P., Southard, J. B., & Tosca, N. J. (2012). Were aqueous ripples on Mars formed by flowing brines? In J. P. Grotzinger & R. E. Milliken (Eds.), *Sedimentary Geology of Mars* (Vol. 102): SEPM Society for Sedimentary Geology.

Lapôtre, M. G. A., Ielpi, A., Lamb, M. P., Williams, R. M. E., & Knoll, A. H. (2019). Model for the formation of single-thread rivers in barren landscapes and implications for pre-Silurian and Martian fluvial deposits. *Journal of Geophysical Research: Earth Surface, 124*(12), 2757-2777. doi:10.1029/2019JF005156

Lawton, T. F. (1982). Lithofacies correlations within the Upper Cretaceous Indianola Group, central Utah. *Utah Geological Association Publication, 10*, 199-213.

Lawton, T. F. (1983). Late Cretaceous fluvial systems and the age of foreland uplifts in central Utah. In J. D. Lowell (Ed.), *Rocky Mountain Foreland Basins and Uplifts* (pp. 181-199). Denver: Rocky Mountain Association of Geologists.

Lawton, T. F. (1986a). Compositional trends within a clastic wedge adjacent to a fold-thrust belt: Indianola Group, central Utah, USA. In P. A. Allen & P. Homewood (Eds.), *Foreland Basins* (pp. 411-423). London: Blackwell.

Lawton, T. F. (1986b). Fluvial Systems of the Upper Cretaceous Mesaverde Group and Paleocene North Horn Formation, Central Utah: A Record of Transition from Thin-Skinned to Thick-Skinned Deformation in the Foreland Region. In J. A. Peterson (Ed.), Paleotectonics and sedimentation in the Rocky Mountain Region, United States (Vol. 41): American Association of Petroleum Geologists. doi:10.1306/M41456C20

Lawton, T. F., Pollock, S. L., & Robinson, R. A. J. (2003). Integrating sandstone petrology and nonmarine sequence stratigraphy: application to the Late Cretaceous fluvial systems of southwestern Utah, USA. *Journal of Sedimentary Research, 73*, 398-406.

Leary, K. C. P., & Ganti, V. (2020). Preserved fluvial cross strata record bedform disequilibrium dynamics. *Geophysical Research Letters, 47*(2), e2019GL085910. doi:10.1029/2019GL085910

Leclair, S. F. (2002). Preservation of cross-strata due to the migration of subaqueous dunes: an experimental investigation. *Sedimentology, 49*(6), 1157-1180. doi:10.1046/j.1365-3091.2002.00482.x

Leclair, S. F., & Bridge, J. S. (2001). Quantitative interpretation of sedimentary structures formed by river dunes. *Journal of Sedimentary Research, 71*(5), 713-716. doi:1527-1404/01/071-713/$03.00

Leopold, L. B., & Maddock Jr, T. (1953). The hydraulic geometry of stream channels and some physiographic implications. *USGS Professional Paper, 252*, 64. doi:10.3133/pp252

Leopold, L. B., & Wolman, M. G. (1957). River channel patterns: Braided, meandering, and straight. *USGS Professional Paper, 282B*, 50. doi:10.3133/pp282B

Li, Y., Bhattacharya, J. P., Ahmed, S., & Garza, D. (2018). Re-evaluating the paleogeography of the river-dominated and wave-influenced Ferron Notom Delta, Southern Central Utah: an integration of detailed facies-architecture and paleocurrent analysis. *Journal of Sedimentary Research, 88*(2), 214-240. doi:10.2110/jsr.2018.9

Lin, W., & Bhattacharya, J. P. (2017). Estimation of source-to-sink mass balance by a fulcrum approach using channel paleohydrologic parameters of the Cretaceous Dunvegan Formation, Canada. *Journal of Sedimentary Research, 87*(1), 97-116. doi:10.2110/jsr.2017.1

Litty, C., & Schlunegger, F. (2017). Controls on pebbles' size and shape in streams of the Swiss Alps. *The Journal of Geology, 125*(1), 101-112. doi:10.1086/689183

Litty, C., Schlunegger, F., & Viveen, W. (2017). Possible threshold controls on sediment grain properties of Peruvian coastal river basins. *Earth Surf. Dynam., 5*(3), 571-583. doi:10.5194/esurf-5-571-2017

Lynds, R., & Hajek, E. (2006). Conceptual model for predicting mudstone dimensions in sandy braided-river reservoirs. *AAPG Bulletin, 90*(8), 1273-1288. doi:10.1306/03080605051

Lyster, S. J., Whittaker, A. C., Allison, P. A., Lunt, D. J., & Farnsworth, A. (2020). Predicting sediment discharges and erosion rates in deep time—examples from the late Cretaceous North American continent. *Basin Research*, 1-27. doi:10.1111/bre.12442

Mahon, R. C., & McElroy, B. (2018). Indirect estimation of bedload flux from modern sand-bed rivers and ancient fluvial strata. *Geology, 46*(7), 579-582. doi:10.1130/G40161.1

McLaurin, B. T., & Steel, R. J. (2007). Architecture and origin of an amalgamated fluvial sheet sand, lower Castlegate Formation, Book Cliffs, Utah. *Sedimentary Geology, 197*(3), 291-311. doi:10.1016/j.sedgeo.2006.10.005

Miall, A. D. (1993). The architecture of fluvial-deltaic sequences in the Upper Mesaverde Group (Upper Cretaceous), Book Cliffs, Utah. *Geological Society, London, Special Publications, 75*(1), 305. doi:10.1144/GSL.SP.1993.075.01.19

Miall, A. D. (1994). Reconstructing fluvial macroform architecture from two-dimensional outcrops; examples from the Castlegate Sandstone, Book Cliffs, Utah. *Journal of Sedimentary Research, 64*(2b), 146-158. doi:10.1306/D4267F78-2B26-11D7-8648000102C1865D

Miall, A. D., & Arush, M. (2001). The Castlegate Sandstone of the Book Cliffs, Utah: Sequence stratigraphy, paleogeography, and tectonic controls. *Journal of Sedimentary Research, 71*(4), 537-548. doi:10.1306/103000710537

Miller, I. M., Johnson, K., Kline, D. E., Nichols, D. J., & Barclay, R. (2013). A Late Campanian Flora from the Kaiparowits Formation, southern Utah, and a brief overview of the widely sampled but little-known Campanian vegetation of the Western Interior of North America. *At the Top of the Grand Staircase: The Late Cretaceous of southern Utah*, 107-131.

Milliman, J. D., & Farnsworth, K. L. (2013). *River Discharge to the Coastal Ocean: A Global Synthesis*: Cambridge University Press.

Paola, C., & Borgman, L. (1991). Reconstructing random topography from preserved stratification. *Sedimentology, 38*(4), 553-565. doi:10.1111/j.1365-3091.1991.tb01008.x

Parker, G. (1976). On the cause and characteristic scales of meandering and braiding in rivers. *Journal of Fluid Mechanics, 76*(3), 457-480. doi:10.1017/S0022112076000748

Parker, G. (2004). *1D Sediment Transport Morphodynamics with Applications to Rivers and Turbidity Currents*.

Parker, L. R. (1976). The paleoecology of the fluvial coal-forming swamps and associated floodplain environments in the Blackhawk Formation (Upper Cretaceous) of central Utah. *Brigham Young University, Geological Studies, 22*, 99-116.

Paul, J. D., Roberts, G. G., & White, N. (2014). The African landscape through space and time. *Tectonics, 33*(6), 898-935. doi:10.1002/2013TC003479

Pederson, J. L., & Tressler, C. (2012). Colorado River long-profile metrics, knickzones and their meaning. *Earth and Planetary Science Letters, 345-348*, 171-179. doi:10.1016/j.epsl.2012.06.047

Perry, G. D., Duffy, P. B., & Miller, N. L. (1996). An extended data set of river discharges for validation of general circulation models. *Journal of Geophysical Research: Atmospheres, 101*(D16), 21339-21349. doi:10.1029/96JD00932

Pettit, B. S., Blum, M., Pecha, M., McLean, N., Bartschi, N. C., & Saylor, J. E. (2019). Detrital-zircon U-Pb paleodrainage reconstruction and geochronology of the Campanian Blackhawk–Castlegate succession, Wasatch Plateau and Book Cliffs, Utah, U.S.A. *Journal of Sedimentary Research, 89*(4), 273-292. doi:10.2110/jsr.2019.18

Reesink, A. J. H., & Bridge, J. S. (2007). Influence of superimposed bedforms and flow unsteadiness on formation of cross strata in dunes and unit bars. *Sedimentary Geology, 202*(1), 281-296. doi:10.1016/j.sedgeo.2007.02.005

Reesink, A. J. H., & Bridge, J. S. (2009). Influence of bedform superimposition and flow unsteadiness on the formation of cross strata in dunes and unit bars — Part 2, further experiments. *Sedimentary Geology, 222*(3), 274-300. doi:10.1016/j.sedgeo.2009.09.014

Reesink, A. J. H., Van den Berg, J. H., Parsons, D. R., Amsler, M. L., Best, J. L., Hardy, R. J., . . . Szupiany, R. N. (2015). Extremes in dune preservation: Controls on the completeness of fluvial deposits. *Earth-Science Reviews, 150*, 652-665. doi:10.1016/j.earscirev.2015.09.008

Rittersbacher, A., Howell, J. A., & Buckley, S. J. (2014). Analysis of fluvial architecture in the Blackhawk Formation, Wasatch Plateau, Utah, U.S.A., using large 3D photorealistic models. *Journal of Sedimentary Research, 84*(2), 72-87. doi:10.2110/jsr.2014.12

Roberts, E. M. (2007). Facies architecture and depositional environments of the Upper Cretaceous Kaiparowits Formation, southern Utah. *Sedimentary Geology, 197*(3), 207-233. doi:10.1016/j.sedgeo.2006.10.001

Roberts, E. M., Tapanila, L., & Mijal, B. (2008). Taphonomy and sedimentology of storm-generated continental shell beds: A case example from the Cretaceous Western Interior Basin. *The Journal of Geology, 116*(5), 462-479. doi:10.1086/590134

Roberts, G. G., White, N., & Lodhia, B. H. (2019). The generation and scaling of longitudinal river profiles. *Journal of Geophysical Research: Earth Surface, 124*(1), 137-153. doi:10.1029/2018JF004796

Roberts, G. G., White, N. J., Martin-Brandis, G. L., & Crosby, A. G. (2012). An uplift history of the Colorado Plateau and its surroundings from inverse modeling of longitudinal river profiles. *Tectonics, 31*(4). doi:10.1029/2012TC003107

Roberts, L. N. R., & Kirschbaum, M. A. (1995). Paleogeography and the Late Cretaceous of the Western Interior of middle North America: coal distribution and sediment accumulation. *U.S. Geological Survey Professional Paper, 1561*, 1-65. doi:10.3133/pp1561

Robinson, R. A. J., & Slingerland, R. L. (1998). Grain-size trends, basin subsidence and sediment supply in the Campanian Castlegate Sandstone and equivalent conglomerates of Central Utah. *Basin Research, 10*, 109-127.

Romans, B. W., Castelltort, S., Covault, J. A., Fildani, A., & Walsh, J. P. (2016). Environmental signal propagation in sedimentary systems across timescales. *Earth-Science Reviews, 153*, 7-29. doi:10.1016/j.earscirev.2015.07.012

Rudge, J. F., Roberts, G. G., White, N. J., & Richardson, C. N. (2015). Uplift histories of Africa and Australia from linear inverse modeling of drainage inventories. *Journal of Geophysical Research: Earth Surface, 120*(5), 894-914. doi:10.1002/2014JF003297

Sadler, P. M. (1981). Sediment accumulation rates and the completeness of stratigraphic sections. *The Journal of Geology, 89*, 569-584. doi:10.1086/628623

Schulze, K., Hunger, M., & Döll, P. (2005). Simulating river flow velocity on global scale. *Advances in Geosciences, 5*, 133-136.

Schumm, S. A. (1968). River adjustment to altered hydrologic regimen - Murrumbidgee River and paleochannels, Australia. *U.S. Geological Survey Professional Paper, 598*, 65. doi:10.3133/pp598

Sewall, J. O., & Fricke, H. C. (2013). Andean-scale highlands in the Late Cretaceous Cordillera of the North American western margin. *Earth and Planetary Science Letters, 362*, 88-98. doi:10.1016/j.epsl.2012.12.002

Seymour, D. L., & Fielding, C. R. (2013). High resolution correlation of the Upper Cretaceous stratigraphy between the Book Cliffs and the western Henry Mountains syncline, Utah, U.S.A. *Journal of Sedimentary Research, 83*(6), 475-494. doi:10.2110/jsr.2013.37

Sharma, S., Bhattacharya, J. P., & Richards, B. (2017). Source-to-sink sediment budget analysis of the Cretaceous Ferron Sandstone, Utah, U.S.A., using the fulcrum approach. *Journal of Sedimentary Research, 87*(6), 594-608. doi:10.2110/jsr.2017.23

Soria-Jáuregui, Á., Jiménez-Cantizano, F., & Antón, L. (2019). Geomorphic and tectonic implications of the endorheic to exorheic transition of the Ebro River system in northeast Iberia. *Quaternary Research, 91*(2), 472-492. doi:10.1017/qua.2018.87

Spieker, E. M. (1946). Late Mesozoic and early Cenozoic history of central Utah. *U.S. Geological Survey Professional Paper, 205D*. doi:10.3133/pp205D

Straub, K. M., Duller, R. A., Foreman, B. Z., & Hajek, E. A. (2020). Buffered, incomplete, and shredded: The challenges of reading an imperfect stratigraphic record. *Journal of Geophysical Research: Earth Surface, 125*(3), e2019JF005079. doi:10.1029/2019JF005079

Stucky de Quay, G., Kite, E. S., & Mayer, D. P. (2019). Prolonged fluvial activity from channel-fan systems on Mars. *Journal of Geophysical Research: Planets, 124*(11), 3119-3139. doi:10.1029/2019JE006167

Szwarc, T. S., Johnson, C. L., Stright, L. E., & McFarlane, C. M. (2015). Interactions between axial and transverse drainage systems in the Late Cretaceous Cordilleran foreland basin: Evidence from detrital zircons in the Straight Cliffs Formation, southern Utah, USA. *GSA Bulletin, 127*(3-4), 372-392. doi:10.1130/B31039.1

Trampush, S. M., Huzurbazar, S., & McElroy, B. (2014). Empirical assessment of theory for bankfull characteristics of alluvial channels. *Water Resources Research, 50*(12), 9211-9220. doi:10.1002/2014WR015597

Trower, E. J., Ganti, V., Fischer, W. W., & Lamb, M. P. (2018). Erosional surfaces in the Upper Cretaceous Castlegate Sandstone (Utah, USA): Sequence boundaries or autogenic scour from backwater hydrodynamics? *Geology, 46*(8), 707-710. doi:10.1130/G40273.1

Tucker, G. E., & Whipple, K. X. (2002). Topographic outcomes predicted by stream erosion models: Sensitivity analysis and intermodel comparison. *Journal of Geophysical Research: Solid Earth, 107*(B9), ETG 1-1-ETG 1-16. doi:10.1029/2001JB000162

Valora, P. M. (2010). *Late Cretaceous to Paleocene Tectono-Stratigraphic Evolution of the Southern Part of the Provo Salient, Sevier Fold-Thrust Belt, Central Utah: New Insights from Geologic Mapping, Growth-Strata Analysis and Structural Modeling in the Thistle, UT 7.5' Quadrangle.* (M.S. thesis), Colorado School of Mines, Golden, Colorado.

van Rijn, L. C. (1984a). Sediment transport III: bedforms and alluvial roughness. *Journal of Hydraulic Engineering, 110*(12), 1733-1754. doi:10.1061/(ASCE)0733-9429(1984)110:12(1733)

van Rijn, L. C. (1984b). Sediment transport, part II: Suspended load transport. *Journal of Hydraulic Engineering, 110*(11), 1613-1641. doi:10.1061/(ASCE)0733-9429(1984)110:11(1613)

van Wagoner, J. C. (1995). Sequence Stratigraphy and Marine to Nonmarine Facies Architecture of Foreland Basin Strata, Book Cliffs, Utah, U.S.A. In J. C. van Wagoner & G. T. Bertram (Eds.), *Sequence Stratigraphy of Foreland Basin Deposits: Outcrop and Subsurface Examples from the Cretaceous of North America* (Vol. 64): American Association of Petroleum Geologists.

Watkins, S. E., Whittaker, A. C., Bell, R. E., Brooke, S. A. S., Ganti, V., Gawthorpe, R. L., . . . Nixon, C. W. (2020). Straight from the source's mouth: Controls on field-constrained sediment export across the entire active Corinth Rift, central Greece. *Basin Research, n/a*(n/a). doi:10.1111/bre.12444

Watkins, S. E., Whittaker, A. C., Bell, R. E., McNeill, L. C., Gawthorpe, R. L., Brooke, S. A. S., & Nixon, C. W. (2018). Are landscapes buffered to high-frequency climate change? A comparison of

sediment fluxes and depositional volumes in the Corinth Rift, central Greece, over the past 130 k.y. *GSA Bulletin, 131*, 372-388. doi:10.1130/B31953.1

Whipple, K. X. (2004). Bedrock rivers and the geomorphology record of active orogens. *Annual Review of Earth and Planetary Sciences, 32*(1), 151-185. doi:10.1146/annurev.earth.32.101802.120356

Whitchurch, A., Carter, A., Sinclair, H., Duller, R., Whittaker, A., & Allen, P. (2011). Sediment routing system evolution within a diachronously uplifting orogen: Insights from detrital zircon thermochronological analyses from the South-Central Pyrenees. *American Journal of Science, 311*, 442-482. doi:10.2475/05.2011.03]

Whittaker, A. C. (2012). How do landscapes record tectonics and climate? *Lithosphere, 4*(2), 160-164. doi:10.1130/rf.l003.1

Whittaker, A. C., Duller, R. A., Springett, J., Smithells, R. A., Whitchurch, A. L., & Allen, P. A. (2011). Decoding downstream trends in stratigraphic grain size as a function of tectonic subsidence and sediment supply. *GSA Bulletin, 123*(7-8), 1363-1382. doi:10.1130/B30351.1

Wobus, C., Whipple, K. X., Kirby, E., Snyder, N., Johnson, J., Spyropolou, K., . . . Sheehan, D. (2006). Tectonics from topography: Procedures, promise, and pitfalls. In S. D. Willett, N. Hovius, M. T. Brandon, & D. M. Fisher (Eds.), *Tectonics, Climate, and Landscape Evolution*: Geological Society of America.

Wobus, C. W., Tucker, G. E., & Anderson, R. S. (2010). Does climate change create distinctive patterns of landscape incision? *Journal of Geophysical Research: Earth Surface, 115*(F4). doi:10.1029/2009JF001562

Wolfe, J. A., & Upchurch Jr., G. R. (1987). North American nonmarine climates and vegetation during the Late Cretaceous. *Palaeogeography, Palaeoclimatology, Palaeoecology, 61*(Supplement C), 33-77. doi:10.1016/0031-0182(87)90040-X

Wolman, M. G. (1954). A method of sampling coarse river-bed material. *Eos Transactions American Geophysical Union, 35*(6), 951-956. doi:10.1029/TR035i006p00951

Wright, S., & Parker, G. (2004). Flow resistance and suspended load in sand-bed rivers: Simplified stratification model. *Journal of Hydraulic Engineering, 130*(8), 796-805. doi:10.1061/(ASCE)0733-9429(2004)130:8(796)

Yalin, M. S. (1964). Geometrical properties of sand waves. *Journal of the Hydraulics Division, 90*(5), 105-119.

Yoshida, S., Willis, A., & Miall, A. D. (1996). Tectonic control of nested sequence architecture in the Castlegate Sandstone (Upper Cretaceous), Book Cliffs, Utah. *Journal of Sedimentary Research, 66*(4), 737-748.

Zhang, J., Covault, J., Pyrcz, M., Sharman, G., Carvajal, C., & Milliken, K. (2018). Quantifying sediment supply to continental margins: Application to the Paleogene Wilcox Group, Gulf of Mexico. *AAPG Bulletin, 102*(9), 1685-1702. doi:10.1306/01081817308

Zhisheng, A., Kutzbach, J. E., Prell, W. L., & Porter, S. C. (2001). Evolution of Asian monsoons and phased uplift of the Himalaya–Tibetan plateau since Late Miocene times. *Nature, 411*(6833), 62-66. doi:10.1038/35075035